NTNU
Det skapende universitet

Performance Calculations for a Model Turbine

John Amund Karlsen

Master i energi og miljø
Oppgaven levert: Juni 2009
Hovedveileder: Per-Åge Krogstad, EPT

Norges teknisk-naturvitenskapelige universitet
Institutt for energi og prosessteknikk

Oppgavetekst

At the Department of Energy and Process Engineering we have for a number of years studied the flow around wind turbines. Among the tools available is a model turbine with a rotor diameter of 0.9m which is used for tests in our large wind tunnel. At the end of 2008 a new set of turbine blades were designed for this model based on a family of profiles developed at National Renewable Energy Laboratory (NREL) in USA. It is considered necessary to perform tests of the turbine with the new blades and compare the results with numerical predictions.

We would like to have the model tested and the results compared with respect to the calculations used in the rotor design. This is to be done with simple laboratory tests. The design calculations were based on the Blade Element Method and it is well known that this method have simplifications which may affect the performance. The main purpose of this work is therefore to perform calculations with a method that solves the complete set of equations of motion to get as accurate results as possible. It is of particular interest to map any behavior of the flow in operating conditions where there are significant differences between the original predictions and the model tests. We expect these differences to begin at operating conditions where the first indication of stall occurs.

- The student is to study the work done previously at the department.
- The numerical computations should be done with the program code Fluent. The student should first perform simple two-dimensional calculations in order to learn how to use the program.
- The student should then generate a mesh in a rotating coordinate system and compute the performance for a set of operating conditions.
- The development of the flow is to be studied and departures between the calculations and the measurements are to be reported.

Oppgaven gitt: 19. januar 2009
Hovedveileder: Per-Åge Krogstad, EPT

Preface

This master thesis is the conclusion of five years at NTNU. It is the final part of a master's degree in 'Energy and Environment'. The thesis has ended up being quite a multilateral work, touching several of the fields of fluid dynamics. During the last year I have been introduced to the mysticism of Computational Fluid Dynamics, and the work has been both inspiring, frustrating and rewarding. I have been working in the laboratory, with equations and with numerical simulations.

Looking back at five years at NTNU, there is a lot to be said. However, summing up these years is not easily done. Even the last semester cannot be captured by mere words on a simple page. Still there are some people that deserve special thanks.

First of all my supervisor Per–Åge Krogstad for his inspiring comments and helpful guidelines that managed to get me through the frustrating parts of this project. Are Johan Simonsen for a very helpful crash course in TGRID, and assistance with the the simulations. Muyiwa 'Sam' Adaramola for help with the experimental setup and kind provision of experimental data for comparison. The opera singer in the hallway. The band downstairs. The sound of the wind tunnel.

My classmates. The crew on Ida. All my friends pulling me out of school and into the mountains where we really belong. Jostein and the north face of Store Trolla. Janne for the lunch boxes and the motivation.

John Amund Karlsen

Abstract

A model wind turbine with a diameter of 0.9 m has been studied both experimentally and numerically. This has been done in order to examine if it works according to the estimates made in the design process. Numerical estimates of the wind turbine power and thrust coefficients under different operational conditions was obtained using a Blade Element Momentum (BEM) and a full CFD simulation of the wind turbine. Experiments was later conducted in the wind tunnel at NTNU for comparison.

The wind turbine uses the NREL s826 profile throughout the blade. An introductory two–dimensional study of the airfoil performance was conducted. This resulted in both lift– and drag–curves used in the BEM calculations, and recommendations for grid refinement when constructing the 3D model of the wind turbine.

A hybrid mesh was used in the final 3D CFD simulations, consisting of $3.54 \cdot 10^6$ cells. The flow field was assumed to be rotationally periodic, and the k–ω SST turbulence model was used in the simulations.

Good correspondence was observed between the experimental and numerical results. The CFD method tended to be superior, predicting the wind turbine power coefficient at low tip speed ratios within 5% of the experimental values.

It was revealed that rotational augmentation was present in the flow field for low tip speed ratios. This is related to three dimensional effects occurring when the root of the blade is stalled. The BEM method is unable to predict or describe these effects. However the method tended to predict the occurrence of stall fairly well.

The rotationally augmented flow field was studied, indicating a dependency of the root geometry.

Severe dynamic effects was observed in the experiment. These effects could be related to regular stall, but there are indications that laminar effects were present. These effects were not captured in the CFD simulations, as a fully turbulent formulation was used. This calls for further studies on the effect of rotation on transition. Moreover, the actual physics behind rotational augmentation are still incompletely understood, requesting further investigation.

Sammendrag

En modell av en vindturbin er studert numerisk og eksperimentelt. Dette er gjort for å verifisere at modellen fungerer i henhold til de beregninger som ble lagt til grunn i designprosessen. Vindturbinen har en diameter på 0.9 m. Numeriske beregniner av vindturbinens effekt– og dragkoeffisient har blitt kalkulert under forskjellige driftsbetingelser. Både en Bladelementmetode (BEM) og en fullstendig løsning av bevegelseslikningene (CFD) har blitt benyttet. Eksperimentelle målinger ble deretter utført i vindtunnelen for å ha et sammelikningsgrunnlag.

Modellturbinen benytter et NREL s826 profil langsmed hele bladet. Grundige todimensjonale undersøkelser av dette profilet ble gjennomført, et studie som resulterte i løft og dragkurver for BEM–beregningene, samt anbefalinger for gridoppløsning i det tredimensjonale gridet som skulle bli konstruert.

Et hybridgrid bestående av $3.54 \cdot 10^6$ celler ble benyttet i CFD–simuleringen. Strømingen ble antatt å være rotasjonsmessig periodisk, og k–ω SST modellen ble benyttet for å modellere de turbulente størrelsene.

Det ble observert god overensstemmelse mellom eksperimentelle og numeriske resultater. CFD–resultatene viste seg å stemme best overens med den målte effektkoeffisienten, med avvik under 5%.

Det ble oppdaget at strømingen rundt vindturbinen ble svært tredimensjonal ved lave tupphastighetsrater. Denne tredimensjonaliteten synes å oppstå når roten av bladet steiler, og forplanter seg langsmed dette i det tupphastighetsraten senkes ytterligere. BEM–metoden er ikke i stand til å beskrive denne prosessen, men viste seg å predikere forholdsvis nøyaktig når bladet steiler.

Det viste seg at vindturbinen opplever en rotasjonsmessig forsterking av løftekraften på vingeseksjoner nær roten på grunn av disse tredimensjonale effektene. De tredimensjonale effektene antas å være avhengige av vingerotens geometriske utforming.

I eksperimentet ble det observert kraftige dynamiske effekter ved begynnende steiling. Disse kan være knyttet til regulær steiling av bladet, men det er indikasjoner på at laminære effekter kan være involvert. Disse effektene ble ikke observert i CFD–simuleringene da en fullturbulent beskrivelse ble benyttet. Effekten rotasjon har på transisjon i grensesjiktet bør studeres videre, da dette kan ha betydning for dynamiske krefter på vindturbiner. Videre er fysikken bak rotasjonsmessig løftforsterkning utilstrekkelig beskrevet, noe som inviterer til videre studier.

Contents

List of Figures

List of Tables

Nomenclature

Latin symbols

Symbol	Definition
A	Area
A_j	Cell face area of cell j
$(A_i)_j$	Cell face area of cell j multiplied with cell face normal vector in x_i direction
B	Number of wind turbine blades
BLh	Boundary layer grid height
C	Local total chord length on wind turbine blade
C_P	Power coefficient
C_T	Thrust coefficient
C_p	Pressure coefficient
C_f	Skin friction coefficient
C_l	Lift coefficient
C_d	Drag coefficient
C_t	Tangential force coefficient
C_n	Normal force coefficient
dF_x	Force per unit span in the normal direction (thrust)
dF_z	Force per unit span in the tangential direction (moment)
$C_{1\epsilon}$, $C_{2\epsilon}$, C_μ	k–ϵ turbulence model constants
C_{b1}, $C_{\nu 2}$	Spalart–Allmaras turbulenve model constants
D_ω	SST turbulence model cross diffusion term
F	Prandtls tip loss factor
F_1, F_2	SST turbulence model blending functions
G_k, $\tilde{G}_k$	Production of mean turbulent kinetic energy
G_ω	'Production' of spesific dissipation rate
G_ν	Production of modified turbulent viscosity
M	Total shaft torque or moment
P	Total wind turbine power
T	Total wind turbine thrust force
T	Temperature
TI	Turbulence intesity, $\frac{\sigma_u}{U} = \frac{\sqrt{u'^2}}{U}$
Re	Reynolds number
R	Radial extention of wind turbine blade
R	Ideal gas constant
R_ϵ	RNG turbulence model correction term
S_{ij}	Mean strain rate tensor
U	Mean axial velocity
W	Mean angular velocity

U_i	Mean velocity in tensor notation
U_{rel}	Flow velocity relative to blade section
V	Voltage measurements
Y_k, Y_ω	SST turbulence model diffusion terms
Y_{nu}	Destruction of modified turbulent viscosity
a	Axial induction factor
a'	Angular induction facor
a_c	Limiting value of the axial induction factor
c	Chordwise position (measured from leading edge)
d	Drag per unit span
l	Lift per unit span
d	Wind turbine diameter
k	Mean turbulent kinetic energy
k_p	Value of k in fist cell point normal to the wall
p	Static pressure
p_∞	Free stream static pressure
q_∞	Free stream dynamic pressure
r	Radial position on wind turbine blade
$\overline{u_i u_j}$	Reynolds stress tensor
u^+	Dimensionless velocity, $\frac{U}{u_*}$
u_*	Wall friction velocity, $\sqrt{\tau_w/\rho}$
x, y, z	Regular Cartesian coordinates
x', y'	Body attached coordinate system
x_i	Position vector in tensor notation
y^+	Dimensionless, sublayer–scaled distance from nearest wall, $u_* y/\nu$
y_p	Normal distance from the wall to the nearest cell point

Greek symbols

Symbol	**Definition**
α	Angle of attack
α_k, α_1, α^*, β	Turbulence model constants
δ	Boundary layer height
δ^*	Displacement height
δ_{ij}	Kronecker delta
ϵ	Dissipation rate
ω	Rotational speed of wind turbine
ω	Spesific dissipation rate
η	RNG turbulence model correction parameter
ρ	Density
σ	Blade solidity
σ	Standard deviation
σ_k, σ_ϵ	k–ϵ turbulence model constants
$\sigma_{k,1}$, $\sigma_{k,2}$, $\sigma_{\omega,1}$, $\sigma_{\omega,2}$	SST turbulence model constants

τ	Viscous shear
τ_w	Viscous wall shear
τ_i	Viscous wall shear in the x_i direction
τ_{turb}	Turbulent time scale
τ_{strain}	Strain rate time scale
λ	Tip speed ratio, $\frac{\omega R}{U_\infty}$
μ	Viscosity
μ_t	Turbulent viscosity
μ_{eff}	Effective viscosity
ν	Kinematic viscosity, $\frac{\rho}{\mu}$
ν_t	Turbulent kinematic viscosity, $\frac{\rho}{\mu_t}$
$\hat{\nu}$	Turbulent viscosity ratio, $\frac{\mu_t}{\mu}$
$\tilde{\nu}$	Modified viscosity (Spalart–Allmaras turbulence model)
φ	Local flow angle
θ	Local twist angle
$\Delta\theta$	Pitch angle
Γ	Circulation per unit span
κ	von Karmáns constant

Chapter 1

Introduction

1.1 The big picture

The knowledge we have about climate change calls for major investments in renewable energy production, in order to satisfy the global demand for energy in a sustainable way. It is now widely recognized that there is *"an urgent need for a veritable energy revolution, involving a wholesale global shift to low–carbon technologies""* [23]. In 2006, renewable energy production met only 7 % of the global primary energy needs.

Increased renewable energy production is known to be one of the main strategies to cut down greenhouse gas emissions and reduce the impacts of global warming. Several countries have introduced support regimes, e.g. feed–in tariffs, in order to increase the profitability of renewable energy production. This has given results in countries like Germany and Spain, where wind power in 2006 accounted for 4.9% and 7.7% of the total electricity generation respectively [23]. During the last decade the global installed wind power capasity has been increasing from 7.6 GW in 1997 to 94.1 GW in 2007 at an annual increase of almost 30% [7]. Most of the growth has taken place in Europe and the US, but countries like China and India are growing markeds for wind power as well.

In a global perspective, wind power have several environmental benefits compared to conventional electricity production. However, there are still negative externalities connected to wind energy production. The main challenges are connected to noise and visual pollution, and interference with living organism populations [7]. Compared to traditional land based wind power, the negative externalities are believed to be smaller for offshore wind power production. Combined with a much higher possible energy yield, it is expected that offshore wind power production will be a considerable part of the future energy mix.

As modern wind turbine efficiency is close to the theoretical maximum dictated by the Betz limit, wind energy competitiveness is best achieved by bringing down the costs of wind turbines. It is known that aerodynamical loading of wind turbine blades is a *"principal determinant of the overall cost of [wind] energy"* [19]. Prediction of the aerodynamical loads on a wind turbine requires a thorough understanding of the rather complex flow fields around wind turbine blades. The presence of three–dimensional effects makes modeling and prediction of these flow fields complicated.

Several methods exists to assess the performance of wind turbines. The Blade Element Momentum Method (BEM) has gained popularity for use in initial studies and for coarse design due to its simplicity and low demand of computational power. The method is a one dimensional approach and

divides the blade into non–interacting annular elements, thus neglecting all three-dimensional effects. This simplifies the calculations considerably but introduces significant errors. In order to account for some of the major three–dimensional effects, certain correction factors can be applied. However, these methods have only showed modest improvement of the results.

Methods that take three–dimensional effects into account are more computational demanding. But advances in the field of computational fluid dynamics (CFD) has made complete solutions of the equations of motion possible for flows around wind turbines. Among others, this has been done by Sørensen et. al [21], who did a Reynolds–averaged Navier–Stokes (RANS) simulation of the NREL Phase VI experiment. This method solves the entire flow field around the wind turbine, revealing detailed information of flow parameters that will be hard to collect experimentally. However, due to problems connected to modeling of turbulence and small scales of motion, these methods also suffers from lack of accuracy.

1.2 Earlier work

Studies of fluid flow around airfoils and wind turbines has been conducted at the institute of fluid mechanics at NTNU for several years. At the moment several experimental studies are being conducted on a small scale wind turbine in the wind tunnel at the institute. The turbine has a diameter of 0.9 m. Late 2008 a new set of turbine blades was designed using the BEM method [22].

The wind turbine blades were designed for a tip speed ratio of 5, and an angle of attack of 7°. The corresponding lift and drag ratio was set to 1.2756 and 0.0135 respectively, and performance calculations were performed using a BEM method. However, some changes was made to the original design, before the blades was produced. Because of this, new performance calculations have to be made. The final blade has a chord length and twist angle varying over the airfoil as shown in figure 1.1. The blades were machined from aluminum.

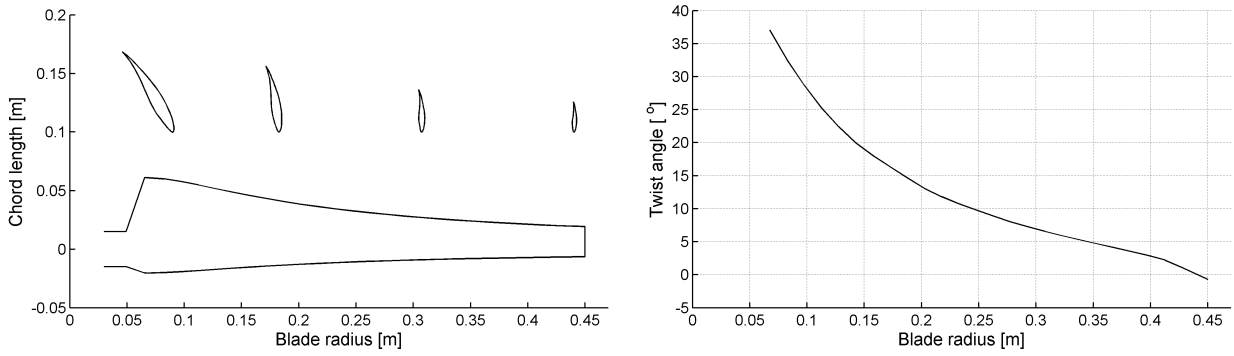

Figure 1.1: Twist angle and chord length

The wind turbine blades were designed using the airfoil profile NREL s826 throughout the blade. This profile was designed at the National Renewable Energy Laboratory (NREL) in the US for variable speed, pitch–controlled HAWTs with blade lengths of 20 to 40 meters. The design Reynolds number of the s826 airfoil was 2.0x10^6, quite higher than what is expected in the wind turbine. With $\lambda \approx 5$ and $U_\infty \approx 10$ m/s, a Reynolds number for the tip of the blade will be close to $1.0 \cdot 10^5$. The low Reynolds number expected here will result in lower l/d–ratios than what is expected for higher Reynolds numbers, due to effects caused by the presence of laminar separation and larger viscous forces.

The BEM performance calculations were conducted using l/d–ratios from the program XFOIL.

1.3 Rationale for the study

It is of interest to investigate if the BEM estimates manage to predict the wind turbine performance under different operating conditions. As a one–dimensional approach to a three–dimensional problem, it is expected that the method will only work well in conditions where the three–dimensional effects are small. This is expected to be the case close to the design tip speed ratio. Under these conditions the tip loss is the main cause of three–dimensionality. This effect is well described, and is normally implemented in the BEM methods.

However, as the tip speed ratio is reduced, the wind turbine blade will become stalled. Under these conditions substantial three–dimensional effects are expected, altering the flow field dramatically. These three–dimensional effects are still incompletely understood and characterized. Certain attempts have been made to model these effects in a way applicable for the BEM method, but no promising results have been documented [13] [19].

These three–dimensional effects can be investigated by solving the full equations of motion. This can be done using CFD software, and has proven to yield good results for wind turbine applications. This will be done in order to investigate the applicability of the BEM method under the influence of certain three–dimensional effects.

Chapter 2

Aim of the study

This study aims to investigate how two different methods predict wind turbine performance and forces acting on the blades of a wind turbine. Experimental data will be obtained through wind tunnel testing and measurements of the torque and thrust forces on a model wind turbine. Special focus will be put on examination of where and why discrepancies between the different methods occur.

In order to do this, a initial investigation of the NREL s826 profile performance will be made using the software XFOIL. This software is known to yield good results for two–dimensional flow over airfoils in the range of Reynolds numbers expected for the operation of the wind turbine. The airfoil performance data will be used in a BEM calculation of wind turbine performance.

By using the CFD–software FLUENT, a thorough two–dimensional study of the airfoil performance will be made. In order to reduce the failure–rate for the three–dimensional cases, there will be a focus on the demand for grid refinement. Different turbulence models will also be tested in order to find the most suitable one for the three–dimensional simulations.

On the basis of the results from the two–dimensional simulations, a three-dimensional grid will be constructed using GAMBIT and TGRID. This grid will be used in FLUENT to make a complete stationary incompressible RANS calculation of the flow field around the wind turbine.

Information from the flow field will be used to investigate the discrepancies between measurements, CFD– and BEM–predictions.

A special foucus will be put on the three–dimensional effects that are expected to occur close to the root of the blade at low tip speed ratios. The precence of these effects will violate the presumptions made in the BEM method, and might cause the method to fail.

Chapter 3

Theory

3.1 Theoretical aspects

The study of fluid motion is a highly challenging field. Only a handful, quite trivial, flow problems have analytical solutions, and scientists and engineers still have to rely on empirical relations and modelling to a large extent. However, this fact has not prevented wind turbine designers approaching the theoretical maximum efficiency when designing state of the art wind turbines. A lot of different advances in the field of fluid mechanics has made this possible.

3.1.1 General physics of a wind turbine

A wind turbine in a device that extracts kinetic energy in the wind. The most common design for modern wind turbines is the Horizontal Axis Wind Turbine (HAWT) design, consisting of blades mounted perpendicularly on a horizontal axis. When these blades are rotating and exposed to a wind velocity, the resulting torque on the horizontal axis is converted into electrical energy by a generator. The energy available in a given cross section, A, normal to the wind direction is given as $P = \frac{1}{2}\rho U_\infty^3 A$ where U_∞ is the wind speed and ρ the density of the air.

However, it is clear that a full exploitation of the kinetic energy in the wind will be impossible. This implies that the wind speed behind the wind turbine has to be zero, a physical impossibility. The air moving through the rotor plane need to retain some kinetic energy in order to be transported away from the wind turbine. Using momentum theory, it can be shown that the maximum aerodynamical efficiency of a wind turbine is 59.3 %, known as the Betz limit. The efficiency of a wind turbine is normally denoted the power coefficient, C_P:

$$C_P = \frac{P_{extracted}}{P_{available}} = \frac{\omega M}{\frac{1}{2}\rho U_\infty^3 A} \tag{3.1}$$

The forces acting on the wind turbine blades do not only create a torque. There are also forces acting in the streamwise direction. These forces are normally called thrust forces (T). The wind turbine foundation has to withstand this force, and knowledge of it is therefor of crucial importance. The thrust coefficient is normally denoted:

$$C_T = \frac{T}{\frac{1}{2}\rho U_\infty^2 A} \tag{3.2}$$

The power generation is determined by the rotational speed and the torque produced by the wind turbine blades. This makes the aerodynamical performance of the blades important. The flow around airfoils has been studied for more than 100 years, and is the basis of modern wind turbine technology. As long as the flow is regarded two–dimensional, there exist several quite accurate methods for calculating the forces acting on such an airfoil. The field of boundary layer theory is one of these approaches, dividing the flow field into two interdependent regions; a boundary layer with large velocity gradients where viscous effects are dominating, and an inviscid flow regime with very small velocity gradients, making viscous effects neglectible.

The inviscid flow regime can be calculated by the use of potential theory, but its dependency on the viscous boundary layer makes its solution more cumbersome, as an iterating process has to be used. This process is the basis of the program XFOIL used to generate lift and drag curves for the airfoil used in the design of the wind turbine blades.

3.1.2 The boundary layer

Due to the no–slip condition, fluid flow over a wall will be affected by its presence. At the wall the velocity has to be zero. This will cause a velocity gradient normal to the wall, implying the presence of a shear stress. This shear stress is given by the elementary law of fluid friction, and has been found to be proportional to the velocity gradient normal to the wall surface [18]:

$$\tau = \mu \frac{dU}{dy'} \tag{3.3}$$

The fluid viscosity μ is a physical property of fluids. At the wall, the friction caused by the shear stress can be calculated through the relation $\tau_w = \mu \frac{dU}{dy}|_w$, as long as the fluid viscosity and the velocity gradient at the wall is known. Integrated along the wall, this stress causes a viscous friction force on a wall exposed to fluid motion.

When regarding the flow around a body, it is clear that the shear stress will reduce the speed of the fluid close to the wall as the flow propagates along the surface. This will cause the boundary layer thickness will grow[1] as the retardation of fluid particles close to the wall will start to affect fluid particles at larger and larger distances from the wall.

Due to continuity, the growth of the boundary layer will cause a displacement of the 'inviscid' flow around the body, causing the streamlines to curve around the body. If the displacement thickness δ^* is added to the body thickness, the effective shape of the body can be found [4].

$$\delta^* = \int_0^\delta \left(1 - \frac{U}{U_\infty}\right) dy' \tag{3.4}$$

The streamline curvature gives rise to a pressure distribution at the edge of the boundary layer. For most airfoils, the boundary layers are very thin compared to the surface curvature. This makes

[1] The boundary layer thickness is not a physical quantity, but is normally defined as distance from the wall where the velocity has reached 99 % of the freestream velocity $U(\delta) = 0.99U_\infty$

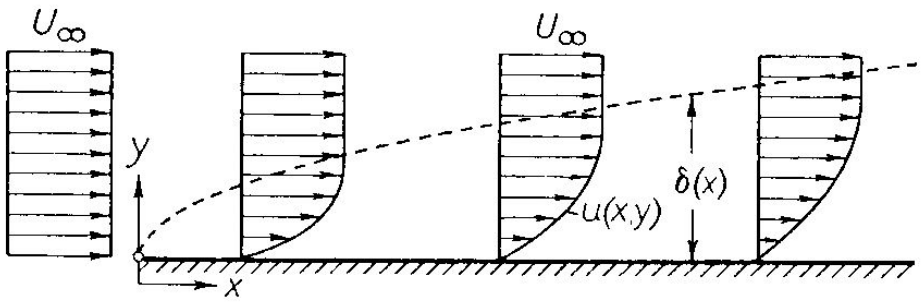

Figure 3.1: The growth of the boundary layer thickness δ over a flat plate. From Schlichting [18].

transverse pressure gradients in the boundary layer disappear, making the pressure distribution at the edge of the boundary layer similar to that on the airfoil surface [18]. This way the pressure forces acting on the surface can be determined using potential theory, as long as the effective shape of the body is known.

3.1.3 Separation

As stated earlier, the pressure distribution normal to the wall is constant through the boundary layer. This makes the pressure vary only with the position on the airfoil. The pressure coefficient is often used when examining pressure distributions around airfoils. It has the definition:

$$C_p = \frac{p - p_\infty}{\frac{1}{2}\rho U_\infty^2} \tag{3.5}$$

At the stagnation point the Bernoulli equation can be used to calculate the pressure. Because the velocity at that point is zero, the pressure is equal to the total pressure. From this one gets $C_p = 1$. From the stagnation point, the fluid accelerates over the leading edge of the airfoil, moving toward lower pressure. This decreasing pressure gradient along the surface $\frac{dp}{dx'} < 0$ is called a favorable pressure gradient.

Some distance from the stagnation point, the minimum pressure is reached, exposing the flow to a adverse pressure gradient, $\frac{dp}{dx'} > 0$. This causes the fluid to decelerate. In an inviscid flow regime, the gain of kinetic energy from the favorable pressure gradient will be enough to make the fluid overcome the adverse pressure gradient, making smooth streamlines enveloping the airfoil. However, the viscous forces drain energy from the flow, making it harder for the fluid to overcome the adverse gradient. If the curvature of the airfoil is large enough for the fluid to decelerate to zero velocity near the surface, the flow separates.

As the velocity gradient at the surface is zero at the separation point, it is clear that the viscous friction force has to be zero as well. From this one knows that the skin friction coefficient (C_f) is zero at the separation point. The skin friction coefficient is equal to:

$$C_f = \frac{\tau_w}{\frac{1}{2}\rho U_\infty^2} \tag{3.6}$$

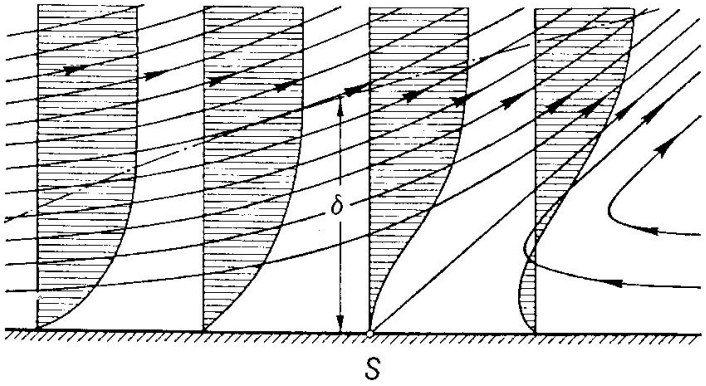

Figure 3.2: Boundary layer flow close to the separation point (schematic). The separation point can be observed where the velocity gradient at the wall is equal to zero ($\frac{dU}{dy'}|_w(x = S) = 0$). From Schlichting [18].

As the fluid is unable to overcome the adverse pressure gradient, separated areas are areas of low pressure. As separation occurs mostly on the downwind side of bodies immersed in fluid flow, separation causes high form drag for blunt bodies and stalled airfoils. For an airfoil at low angles of attack, its streamlined shape reduces the amount of form drag. Separated areas are also recognized as areas of low pressure gradients. Thus, separation can be observed on a C_p–plot as areas of horizontal C_p–lines.

In the separation zone, the velocities will be low or even negative. This makes the boundary layer grow, leading to an increase in the displacement thickness. This will alter the effective geometry of the airfoil, most often reducing its aerodynamic performance. The larger the angle of attack of an airfoil, the closer to the leading edge separation will occur. Eventually the airfoil drag force increases and the lift force decreases. This reduction in airfoil performance indicates that the airfoil is stalled. Stall can occur either abruptly or more smoothly, depending on the airfoil geometry and flow characteristics. As separation rarely is a stationary occurrence, the separation point tends to move back and forwards, causing large dynamic forces on stalled airfoils. Because of this, wind turbine airfoils are often characterized with very docile stall characteristics, as this will reduce dynamic forces related to stall.

3.1.4 Reynolds number

The Reynolds number is defined as the ratio between inertial and viscous forces. It is normally defined as the ratio of the velocity and some characteristic length to the kinematic viscosity of the fluid. For an airfoil the characteristic length is normally the chord length, C:

$$Re = \frac{UC}{\nu} \tag{3.7}$$

High Reynolds number flows are generally characterized by thin boundary layers indicating higher viscous forces. However, as the inertial forces scales with the square of the velocity, the lift to drag ratio will generally increase with the Reynolds number. As the Reynolds number tend to infinity, the asymptotic behavior for the flow around an airfoil is given by the inviscid (potential flow) solution.

3.1.5 Flow regimes and transition

The boundary layer flow can be either laminar or turbulent. Laminar flow is also called layered flow, as the flow seems to move in separate layers without much interference. Laminar flow regimes are characterized by steady fluid properties, a fact that causes transverse exchange of e.g. momentum rely merely on molecular motion [4]. These flows can only exist under certain restrictions. As soon as a parameter like the Reynolds number exceeds a limit (Re_{crit}), the flow in the boundary layer gets unstable. These instabilities propagates throughout the boundary layer. Depending on the degree of amplification of some unavoidable infinitesimal disturbances, the flow will transist into a turbulent flow some distance downstream the point of instability. Apart from a small layer close to the wall where the viscous effects are still dominating[2], the boundary layer will now be turbulent.

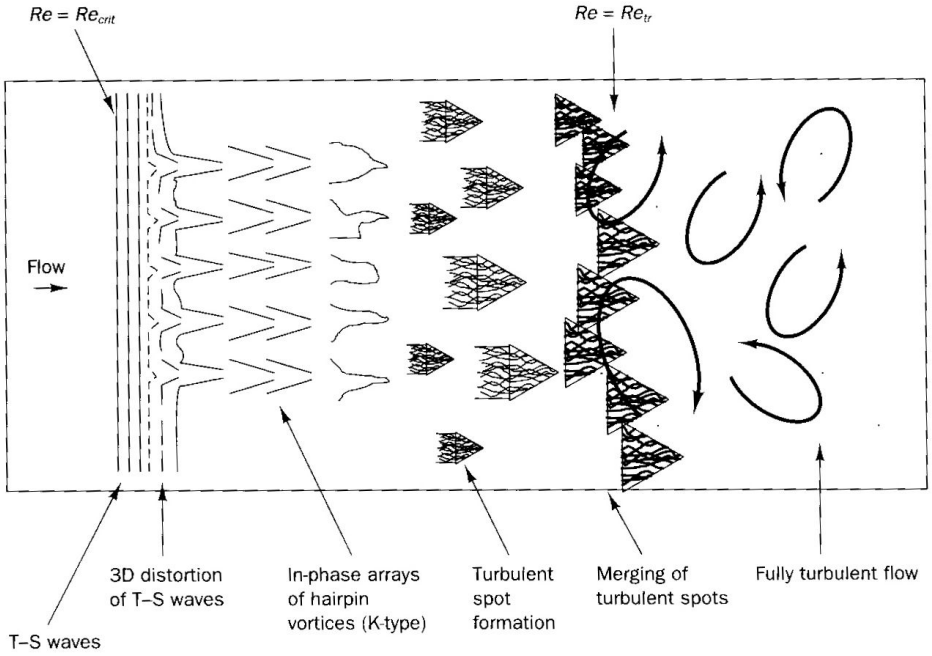

Figure 3.3: Schematic of the transition on a flat plate. Re_{crit} is found at the position of laminar instability, while Re_{tr} is found at the point of transition. From Versteeg [26].

Turbulent flows are characterized by irregular fluctuating motion that is strongly rotational and three dimensional [24]. The time and length scales of the turbulent motion spans a wide spectrum, but even the smallest length scales are far larger than that of molecular motion. The fact that the turbulent length scales of motion are far larger than the molecular (laminar) makes turbulent flows more diffusive than laminar flows. The increase in transverse transport of momentum has an effect both on the shape and size of the turbulent boundary layer; increasing the velocity gradient near the wall and the boundary layer height. This can be seen from figure 3.4.

An airfoil moving through still air will experience a laminar flow regime approaching it. As the fluid particles in the boundary layer flows over the airfoil they are constantly subjected to several disturbances caused by e.g. roughness elements on the surface, free stream turbulent motion, local heating or other micro scale effects. Eventually the laminar flow becomes unstable. This will happen either if the local Reynolds number exceeds a certain limit, or if the boundary layer is subject to

[2]This layer is normally called the viscous sublayer

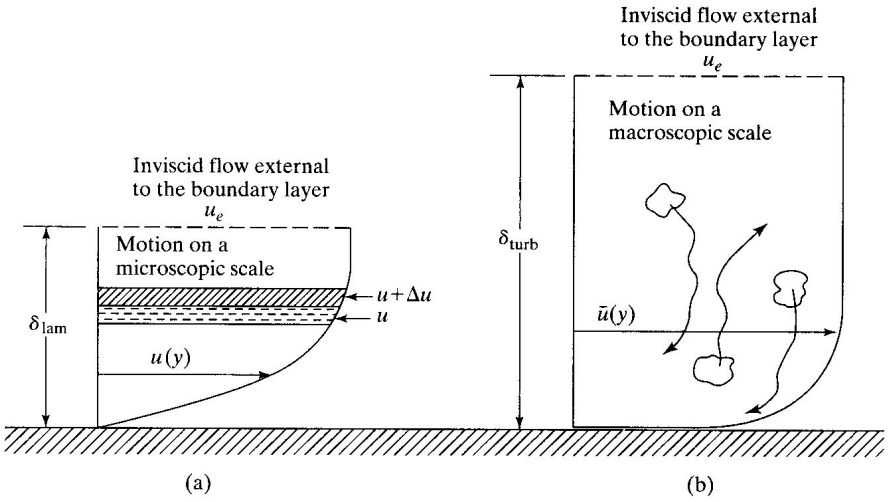

Figure 3.4: Schematic og laminar and turbulent boundary layers. The differences in momentum transport is illustrated for both the (a) laminar boundary layer and (b) the turbulent boundary layer. From Bertin [4].

an adverse pressure gradient. The initial disturbances will grow, eventually turning the laminar flow into a turbulent flow regime. The stronger the disturbances, the faster this process will go.

For a turbulent boundary layer, the high velocity gradient at the wall increases the shear stress, resulting in higher skin friction for surfaces exposed to turbulent flow. Laminar flow is therefore favorable over certain parts of an airfoil, due to the reduced viscous drag. However, the low velocity gradient and momentum transport close to the wall makes the flow more sensitive to separation, an undesirable effect for most airfoil flows.

3.1.6 Laminar separation bubbles

As the laminar boundary layer has less momentum transport close to the surface, it has less available kinetic energy to overcome adverse pressure gradients. If the transition to turbulent flow does not happen before the pressure gradient becomes adverse, separation can occur near the leading edge even for low angles of attack.

The separation will increase the amount of disturbances in the flow, leading to a rapid transition. After this transition occurs, the increased mixing will transport momentum towards the surface at a higher rate than before, thus forcing the flow towards reattachment. If the airfoil Reynolds number is more that approximately $7.0 \cdot 10^4$, the boundary layer can reattach, as long as the airfoil curvature or adverse pressure gradient is sufficiently small. In this case a laminar separation bubble is formed [15]. However, a high curvature or adverse pressure gradient might cause the flow to remain separated far downstream, causing the airfoil to stall. At the Reynolds numbers expected in the wind tunnel, this effect is expected.

This kind of stall can be very dramatic. If a laminar separation bubble close to the leading edge burst, the airfoil will experience a very abrupt changes in lift and drag.

Modelling transisting flows is a complicated exercise with a high demand of computational power and advanced models. As this is a mere masters project, this effects will not be modeled in detail,

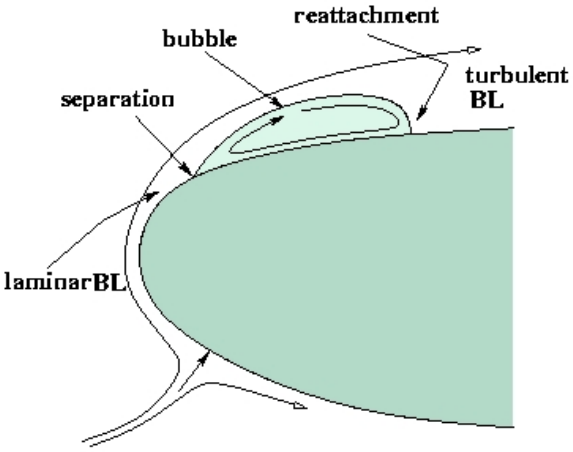

Figure 3.5: Schematic of a laminar separation bubble. From Hu and Yang [11].

but only commented upon.

3.1.7 Lift and drag

With the pressure distribution known, the pressure forces acting on the effective body can be determined. Combined with viscous friction, the net forces acting in the streamwise and transverse direction can be calculated by integrating the pressure forces and the skin friction over the surface. The resultant forces are normally called drag in the streamwise direction, and lift in the transverse direction. The forces are often non–dimensionalised by dividing them by the dynamic pressure times the area in consideration. In a two dimensional case, the sectional lift and drag coefficients are given as:

$$C_l = \frac{l}{\frac{1}{2}\rho U_\infty^2 C} \tag{3.8}$$

$$C_d = \frac{d}{\frac{1}{2}\rho U_\infty^2 C} \tag{3.9}$$

l and d being the lift and drag per unit span of the airfoil respectively. These are the forces creating the torque and thrust forces acting on a wind turbine.

It can be shown that a lifting force introduces circulation to the flow field. The relation between the induced circulation and the lifting force is described by the Kutta–Jukowski theorem:

$$l = \rho_\infty U_\infty \Gamma \tag{3.10}$$

Γ is the total circulation induced per unit span.

3.1.8 Tip loss

For an airfoil of infinite span, the flow will be completely two–dimensional (if one ignore the turbulent scales of motion). This makes the lift per unit span (and thus the circulation) independent on the spanwise position. For a wing of finite length, like a wind turbine blade, this is no longer the case. The high–pressure air on the pressure side of the blade will spill out around the tip towards the low–pressure air on the suction side. This will decrease the pressure difference between the suction and pressure side, reducing the lift towards the tip.

This tip effect will also induced spanwise velocity components over the blade, creating a vortex sheet behind the wing, that tend to roll up in large wing–tip vortices with high velocities and low pressures. The trailing vortices induce an additional component of drag, as the effective angle of attack is reduced due to downwash. This is known as vortex drag or induced drag and is known to be proportional to the square of the lift coefficient divided by the aspect ratio, given an unswept, untapered wing [4].

It has been shown that the amount of circulation induced by the blade tends to zero as one approaches the tip. The Prandtl tip loss factor describes this lift reduction, and is used in the BEM method to account for the tip effects.

As the wind turbine blade examined in this report has a sharp edge near the root as well, it is possible that a hub vortex will be present here. This will lead to the same effects as described above. But as the relative velocity is far lower at this point, the effect of this vortex can be assumed to be lower than near the tip.

3.1.9 Rotational augmentation

Rotational augmentation or stall delay is still incompletely understood and characterized. But there are strong indications that rotational effects can enhance blade section lift and delay stall on wind turbine blades and propellers compared to a non–rotating reference. Several studies have been performed in order to examine the effects of rotation on a wind turbine, but the mechanisms behind the effect of stall delay have not yet been determined.

A study of Schreck and Robinson did show that stall delay is associated with spanwise pressure gradients and chordwise 'pressure signatures'. One interpretation is that it is connected to centripetal and Coriolis forces [19].

The presence of centripetal and Coriolis forces will influence the flow field around the blade to a certain extent. Because of the blade rotation, the fluid particles in a blade–fixed reference system will experience an acceleration away from the blade. This acceleration imposes a small positive radial velocity component on the fluid in the boundary layer. Due to the Coriolis effect, this radial velocity component will induce a chordwise force that will act on the fluid in the boundary layer. A force acting in the chordwise direction can be interpreted as a favorable pressure gradient, delaying separation [19].

It is however unclear what are the main driving factors behind this effect. The only thing clear is that three dimensional effects are present, altering the flow field from the idealised case examined in the BEM method.

3.2 The BEM–method

As seen in the previous chapter, the flow around the blades of a wind turbine is far more complicated than the two–dimensional flow assumed to be the case when making a BEM calculation. The two main reasons for this are the three–dimensional effects caused by the rotation and the fact that the blades are of finite length.

As the blade sections are regarded non–interacting, these effects are neglected when using the BEM method. This simplifies the calculations dramatically, but introduces several errors. To account for this, some of the effects are addressed through modelling. The BEM method normally employs two such models: Prandtls tip loss factor and Glauerts correction for high values of axial induction. These will be discussed in the following chapters.

The objective of a BEM–calculation is to determine the thrust and moment force caused by the fluid on each of the blade elements. The flow is normally divided into non–interacting annular streamtubes of width dr. The aerodymaical forces acting on the corresponding blade element is found, thus determining the axial and angular momentum changes of the air in the annular strip. In order to determine the lift and drag forces acting on each element, knowledge of the local angle of attack (α) and flow velocity relative to the blade (U_{rel}) needs to be obtained, as well as the blade twist angle and chord length. As the design of the blades in this study is known, only the two first quantities needs to be determined.

3.2.1 Axial induction factor

When the wind turbine extracts energy form the wind, the kinetic energy of the wind has to be reduced as it flows through the rotor plane of the turbine. The axial induction factor a describes the axial speed reduction caused by the presence of the blades. This way, the axial speed at the rotor plane U_t is given by the relation $U_t = U_\infty(1 - a)$. This is deducted from the definition of the axial induction factor a:

$$a = \frac{U_\infty - U_t}{U_\infty} \tag{3.11}$$

The axial induction factor is thereby a measure of the kinetic energy extraction from the wind. A small a indicates that little kinetic energy is extracted from the airflow, thereby indicating a low efficiency. However, a high a implies that U_t is small, thus indicating a too high kinetic energy extraction. As this reduces the velocity at the rotor plane, the efficiency will be reduced as well. The optimum value of a can be found by using momentum theory on the flow around the turbine, yielding the following equation for the power coefficient, C_P:

$$C_P = 4a\,(1 - a)^2 \tag{3.12}$$

The optimum found by differentiation, is known as the Betz limit, giving $C_{Pmax} = 0.593$ for $a = 1/3$.

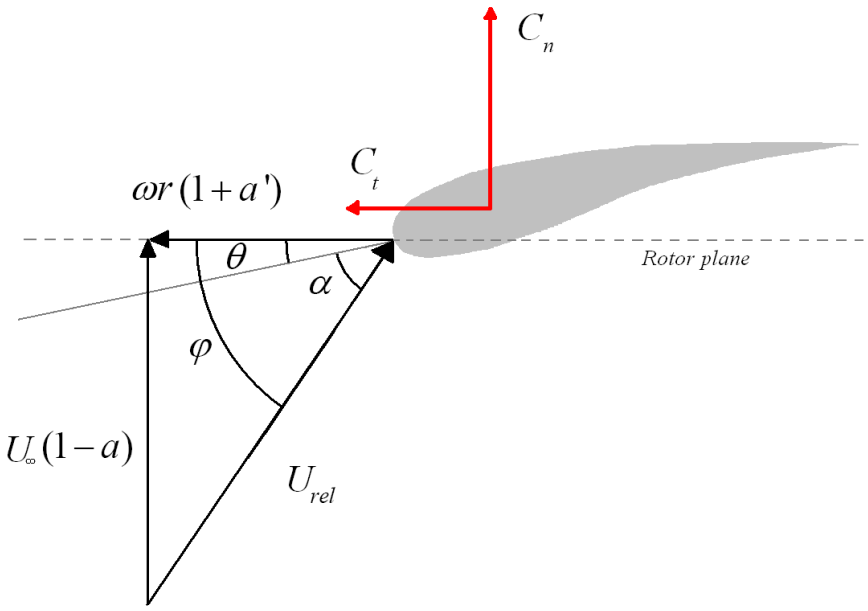

Figure 3.6: The relations between α, φ, θ, the velocities and forces acting on a wind turbine blade element.

3.2.2 Angular induction factor

The circulation created by the lift force around the rotating blade, and the trailing vortices caused by the finite length of the blade, induces rotation in the flow downstream of the wind turbine. Upstream of the turbine, no rotation will be present. In a case where energy is extracted from the wind, the wake will be rotating in the opposite direction of the wind turbine rotor. The wake rotation can be regarded a net loss of energy. Because it is directly related to the torque generated by the fluid flow, a high tip speed ratio and low torque will lead to low losses due to wake rotation.

The angular component of the wind speed at the rotor plane is normally given as a fraction of the local rotational speed of the blade ($\omega r a'$), where a' is the angular induction factor. Thus, the angular velocity component of the relative wind speed at the rotor plane, will be given by the rotational speed of the blade, and the induced rotational speed. This way the tangential velocity component at the rotor plane will be given as $W_t = \omega r(1 + a')$.

$$a' = \frac{W_t}{\omega r} \tag{3.13}$$

The relative inflow velocity (U_{rel}) and the inflow angle (φ) can be calculated as long as the axial and angular induction factors are known. Using the definitions of the axial and angular induction factors, the effective inflow velocity and the inflow angle will be given by:

$$U_{rel} = \sqrt{[U_\infty(1-a)]^2 + [\omega r(1+a')]^2} \tag{3.14}$$

$$\tan\varphi = \frac{U_\infty(1-a)}{\omega r(1+a')} \tag{3.15}$$

The angle of attack, α, is found by subtracting the twist angle, θ, from the inflow angle, φ. As α and U_{rel} are known, sectional lift and drag forces acting on each element can be found. These forces are transformed into normal and tangential forces through trigonometrical relations. The normal force coefficient (C_n) is defined as acting in the flow direction, thus acting as a thrust force. The tangential force coefficient (C_t) is defined as acting in the tangential direction, thus acting as a moment on the wind turbine axis. They are determined using the following equations:

$$C_n = C_l \cos\varphi + C_d \sin\varphi \tag{3.16}$$

$$C_t = C_l \sin\varphi - C_d \cos\varphi \tag{3.17}$$

When the normal (thrust) forces and tangential (moment) forces for each blade element are found, the total thrust or torque can be found by integration along the blade.

3.2.3 Prantls tip loss

As a leakage of circulation is present at the tip, this needs to be corrected for in the BEM code. It is clear that the forces acting on a blade element close to the tip should be lower than for a similar element at the middle of the blade.

Prandtl showed that the circulation created by a rotating blade of a finite length tends exponentially to zero close to the tip. This is the basis of the Prandtl correction factor that can be added to the BEM equations; here given by the approximate formula introduced by Glauert [20]:

$$F = \frac{2}{\pi}\cos^{-1}\left[e^{-\frac{B(R-r)}{2r\sin\varphi}}\right] \tag{3.18}$$

This factor stays close to one for most radii, but goes quickly to zero close to the tip. This makes the correction apply only for the elements close to the tip of the blade.

In the further equations, the solidity of the blades is defined as

$$\sigma(r) = \frac{C(r)B}{2\pi r} \tag{3.19}$$

where B is the number of blades and r is the local radius. The corrected equations for the performance calculations are given as [10]:

$$a = \frac{1}{\frac{F4\sin^2\varphi}{\sigma C_n} + 1} \tag{3.20}$$

$$a' = \frac{1}{\frac{F4\sin\varphi\cos\varphi}{\sigma C_t} - 1} \tag{3.21}$$

$$dF_x = 4\pi r \rho U_\infty^2 a(1-a)F \tag{3.22}$$

$$dF_z = 4\pi r^2 \rho U_\infty \omega (1-a) a' F \tag{3.23}$$

Here dF_x is the force acting per unit span of the blade in the streamwise (x) direction, while dF_z is the force acting per unit span of the blade in the tangential (z) direction. If dF_x is integrated along the blade, the total thrust force (T) is found. When dF_z is multiplied with the local radius and integrated along the blade to the tip, the total moment (M) is found.

$$T = \int_0^R dF_x dr \tag{3.24}$$

$$M = \int_0^R dF_z r dr \tag{3.25}$$

Close to the tip the Prandtl tip loss factor will go to zero. This will increase the axial induction factor toward one. This will reduce the angle of attack towards zero, reducing the forces acting on the tip of the blade. However, if the angular induction factor is decreased towards minus one at a rate faster than the axial induction factor, this will cause the angle of attack to increase toward the tip.

3.2.4 Glauerts correction for high values of a

As can be seen from equation 3.22, the thrust force will tend to zero as a tends to one. This is clearly unphysical, as it is expected that the thrust will increase. The thrust coefficient will actually increase beyond one. Glauert suggested a correction equation that should be used in the iterating process as soon as a increased beyond the value $a_c = 0.2$.

$$a = \frac{1}{2}\left[2 + K(1-2a_c) - \sqrt{(K(1-2a_c)+2)^2 + 4(Ka_c^2 - 1)}\right] \tag{3.26}$$

$$K = \frac{F 4 \sin^2 \varphi}{\sigma C_n} \tag{3.27}$$

This correction factor has proven to give good results for wind turbine, and is normally used in blade element momentum calculations [10].

3.2.5 Hub loss

The fact that the blades has to be connected to a hub introduces three dimensional effects at the root of the blade. The presence of a hub will affect the flow, inducing a speed up close to the root of the blade. This could make a simple omission of the hub area erroneous. In addition the presence of a hub vortex will influence the lift and drag coefficients close to the root of the blade. This could be addressed by introducing a hub loss factor. However, because the wind speeds are small compared to the tip speeds for most operational conditions, the errors introduced here are assumed to be small.

3.2.6 Performance calculation

A flow chart for the calculation of a wind turbine performance with the Prandtl tip loss and Glauerts correction factor is shown in figure 3.7. The calculation procedure is further described in Sætas project thesis. The program PERFORMANCE and FORCE has been used in the following calculations.

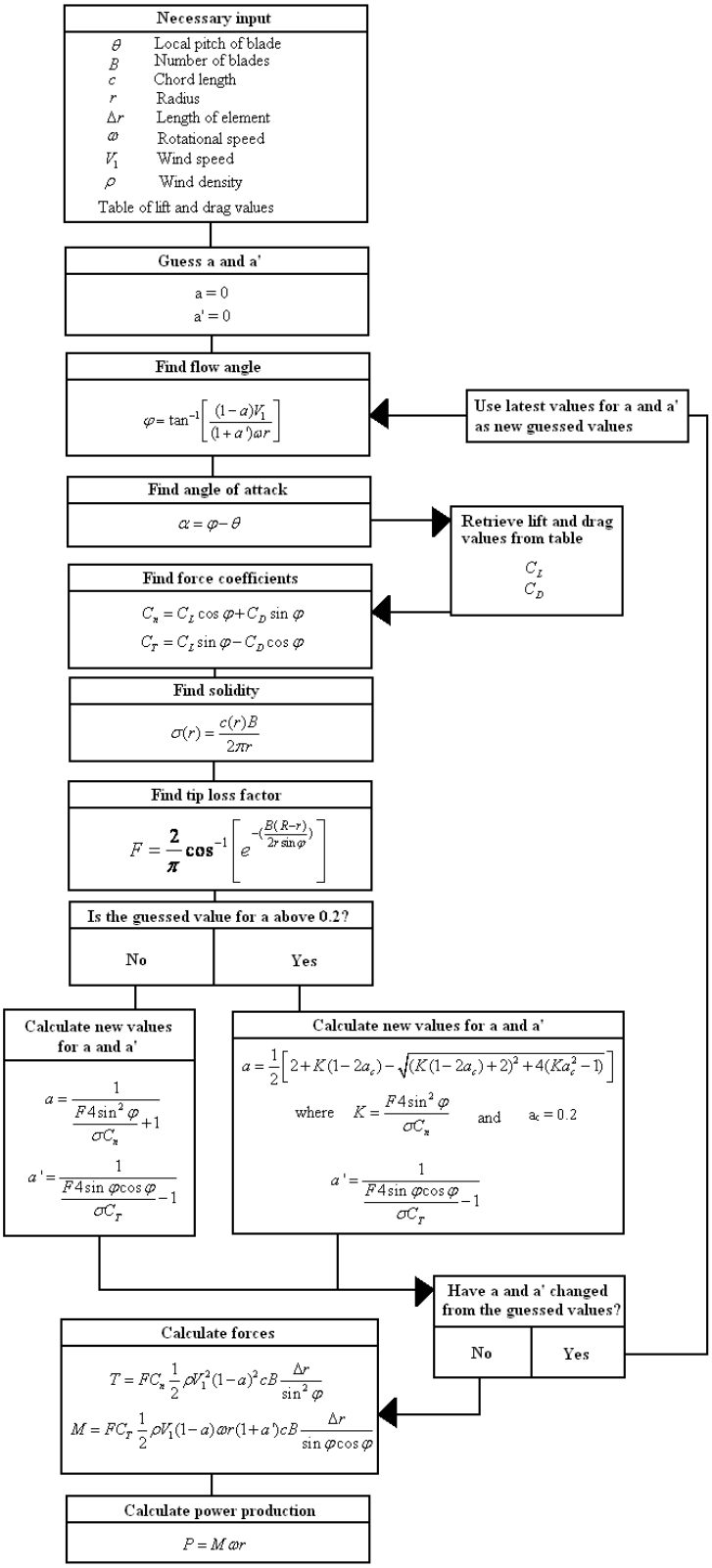

Figure 3.7: Calculation flow chart for performance calculations. From Sæta [22]

3.3 Numerical methods

The mathematical description of fluid motion is given by three laws of conservation: Conservation of mass, momentum and energy. Under assumptions that the flow is incompressible, and that there exist a linear relation between shear and the velocity gradient, the fluid motion can be described by the continuity equation and the well known Navier–Stokes equations.

The solution of these equations however, is not straightforward. Only a few, relatively trivial problems have known analytical solutions. As soon as certain parameters (e.g the Reynolds number) exceeds certain limits, the flow regime becomes turbulent. The spatial scales of the turbulent motion in the flow are significantly larger than that of molecular motions, so that the fluid can still be regarded a continuum. But these scales are yet so small that a complete calculation of these motions is impossible for most engineering problems.

3.3.1 The RANS equations

The most common way of addressing the issue with time–dependent, irregular motion is normally to split all time-varying components of the flow into a mean and a fluctuating value, e.g U_i and u_i for the velocity in the x_i direction. In this way a mean flow regime can be solved, with the fluctuating values being superimposed on the stationary solution. When this is introduced into the governing equations, they can be averaged, resulting in the well known RANS equation and an averaged continuity equation:

$$U_j \frac{\partial U_i}{\partial x_j} = -\frac{1}{\rho}\frac{\partial p}{\partial x_i} + \frac{\partial}{\partial x_j}\left(\nu\left(\frac{\partial U_i}{\partial x_j} + \frac{\partial U_j}{\partial x_i}\right) - \overline{u_i u_j}\right) \tag{3.28}$$

$$\frac{\partial U_j}{\partial x_j} = 0 \tag{3.29}$$

The turbulent motions are now reduced to one term in equation 3.28, called the Reynolds stress tensor $-\overline{u_i u_j}$. The lack of an analytical solution to this term forces one to model these stresses, most often done by introducing the concept of a turbulent viscosity ν_t. This approach was suggested by Boussinesq in 1877, giving the following definition of the turbulent viscosity [5]:

$$-\overline{u_i u_j} = \nu_t\left(\frac{\partial U_i}{\partial x_j} + \frac{\partial U_j}{\partial x_i}\right) - \frac{2}{3}k\delta_{ij} \tag{3.30}$$

where $k = \frac{1}{2}\overline{u_i u_i}$ is known as the mean turbulent kinematic energy, and δ_{ij} as the Kronecker delta. By introducing this concept, it can be seen that the magnitude of the different Reynolds stresses must be equal, resulting in an assumption of isotropic turbulence. Isotropic turbulence is known to be an exception rather than the rule, yet models using this concept still yield quite good results in many cases. Several attempts have been made to model the different stresses separately, using so–called Reynolds Stress Models (RSM). However, these tend to be quite computationally demanding. Moreover, the increased complexity of these models have not yet proven to yield correspondingly more accurate results [26]. The turbulent viscosity is normally modelled by introducing the *dissipation rate* of k, ϵ. This approach was standardized by Jones and Launder when they introduced the k–ϵ–model in 1972. Another approach was introduced by Kolmogorov, and refined by Wilcox. They chose to

model the turbulent viscosity by introducing the concept of the *spesific dissipation rate*, ω that has dimensions of $(time)^{-1}$.

$$\nu_t = \frac{\mu_t}{\rho} = C_\mu \frac{k^2}{\epsilon} = \frac{k}{\omega} \tag{3.31}$$

The two different approaches shown above are the basis of two of the most used two–equation turbulence models, namely the k–ϵ– and k–ω–model. In order to calculate ν_t, transport equations have to be made for the two unknown variables. The basis of two–equation turbulence modelling lies in the modelling or derivation of the transport equations for these two unknowns.

Several models for the transport equation for k are available, being the basis of most one–equation turbulence models. The challenge in two–equation turbulence modelling lies in the transport equation for the second unknown.

3.3.2 Turbulence models

The k–ϵ–model

The first k–ϵ–model was proposed in 1972 by Jones and Launder, when they modelled a transport equation for ϵ [14]. The effort has been criticised for being too much of a 'drastic surgery' to the original equations [28], however it is still one of the most used turbulence models available.

$$\frac{D\rho k}{Dt} = \frac{\partial}{\partial x_j}\left[\left(\mu + \frac{\mu_t}{\sigma_k}\right)\frac{\partial k}{\partial x_j}\right] + G_k - \rho\epsilon \tag{3.32}$$

$$\frac{D\rho \epsilon}{Dt} = \frac{\partial}{\partial x_j}\left[\left(\mu + \frac{\mu_t}{\sigma_\epsilon}\right)\frac{\partial \epsilon}{\partial x_j}\right] + C_{1\epsilon}\frac{\epsilon}{k}G_k - C_{2\epsilon}\rho\frac{\epsilon^2}{k} \tag{3.33}$$

$$G_k = -\rho\overline{u_i u_j}\frac{\partial U_j}{\partial x_i} \tag{3.34}$$

G_k is the production of k, and is through the Boussinesq approximation given as $G_k = 2\mu_t(S_{ij}S_{ij})$. The strain–rate tensor is given as: $S_{ij} = 1/2\left(\frac{\partial U_i}{\partial x_j} + \frac{\partial U_j}{\partial x_i}\right)$. The coefficients in the model are presented in table 3.1. The model is derived under the assumption that the flow is fully turbulent, and that the effect of molecular viscosity is neglectible. The model is therefore only valid for fully turbulent flows, and cannot predict transition.

Even if the model is widely used, it has major deficiencies, especially in recirculation areas and areas of rapid strain. The simplification introduced through the Boussinesq–approximation makes the turbulent stresses proportional to the strain–rate. μ_t is not a scalar in reality, therefore in cases of high anisotropy better results can be obtained by modelling the Reynolds stresses separately, using a Reynolds Stress Model (RSM). As this is quite computationally demanding, and the solutions tend to be more unstable than general two–equation solutions this approach is not used in this study.

The k–ϵ RNG–model

In 1986 Yakhot and Orszag used renormalisation group (RNG) theory to address some of the deficiencies in the k–ϵ–model [30]. Two major changes were made to the original model. First, the introduction of a differential model for the effective viscosity, making the model valid for transitional flows. Second, an introduction of a parameter $\eta = \sqrt{2S_{ij}S_{ij}}k/\varepsilon$ that addresses some of the problems with overprediction of turbulent stresses in areas of rapid strain. The parameter is given as the ratio of the turbulent timescale $\tau_{turb} = k/\varepsilon$ to a timescale of the strain–rate $\tau_{strain} = 1/\sqrt{2S_{ij}S_{ij}}$ [31]. It is large in areas of rapid strain, and leads through a term in the transport equation of ϵ to an increase of dissipation, and to a reduction of the production of k.

The model is presented in Fluent as:

$$\frac{D\rho k}{Dt} = \frac{\partial}{\partial x_j}\left(\alpha_k \mu_{eff}\frac{\partial k}{\partial x_j}\right) + G_k - \rho\epsilon \tag{3.35}$$

$$\frac{D\rho \epsilon}{Dt} = \frac{\partial}{\partial x_j}\left(\alpha_\epsilon \mu_{eff}\frac{\partial \epsilon}{\partial x_j}\right) + C_{1\epsilon}\frac{\epsilon}{k}G_k - C_{2\epsilon}\rho\frac{\epsilon^2}{k} - R_\epsilon \tag{3.36}$$

With $C_\nu \approx 100$ and $\hat{\nu} = \mu_{eff}/\mu$, the model for the effective viscosity is given as[3]:

$$d\left(\frac{\rho^2 k}{\sqrt{\epsilon\mu}}\right) = 1.72\frac{\hat{\nu}}{\sqrt{\hat{\nu}^3 - 1 + C_\nu}}d\hat{\nu} \tag{3.37}$$

In the high Reynolds number form, the effective viscosity is given by equation 3.31. The introduction of the η–parameter is done through the term R_ϵ in the transport equation for ϵ. Due to this term, the RNG–model tends to be more responsive to effects of rapid strain and streamline curvature, and tends to be superior to the standard formulation for several classes of flows.

$$R_\epsilon = \frac{C_\mu \rho \eta^3 \left(1 - \eta/4.38\right)}{1 + 0.012\eta^3}\frac{\epsilon^2}{k} \tag{3.38}$$

The coefficients in the models described are as follows [8]:

Model	C_μ	$C_{1\varepsilon}$	$C_{2\varepsilon}$	σ_k	σ_ε
Standard $k-\varepsilon$	0.09	1.44	1.92	1.0	1.3
RNG $k-\varepsilon$	0.0845	1.42	1.68	-	-

Table 3.1: Coefficients in the k–ε- and RNG–model

The k–ω SST–model

The original formulation of the transport equation for ω was made by Kolmogorov, but it was later improved by Wilcox [28]. It is an empirical model, based on transport equations for the turbulent kinetic energy k, and the spesific dissipation rate ω. Kolmogorovs derivation of the original transport

[3]The parameter $\hat{\nu}$ is very close to the turbulent viscosity ratio, and there are therefore given the same symbol.

equations was probably (according to Wilcox) made by dimensional analysis and physical reasoning. A quite different path than Jones and Launder chose.

The k–ω–model is known to be the model of choice in the viscous sublayer, and it allows simple Dirichlet boundary conditions to be specified walls [16]. This makes it possible to apply the model throughout the boundary layer. However, in the wake region of the boundary layer, the model is quite sensitive to freestream values of ω. The fact that this deficiency is not shared by the k–ϵ–model, gave rise to Menters idea of coupling them.

Through the introduction of blending functions (F_1 and F_2), Menter combined the two models in his Shear Stress Transport model; the k–ω–model was applied in the near wall region, while the k–ϵ–model was applied in the outer wake region and the free shear layers [16]. He also made some modification of the definition of the eddy viscosity in order to account for the transport of the principal turbulent stress.

The model used in Fluent is given as [8]:

$$\frac{D\rho k}{Dt} = \frac{\partial}{\partial x_j}\left[\left(\mu + \frac{\mu_t}{\sigma_k}\right)\frac{\partial k}{\partial x_j}\right] + \tilde{G}_k - Y_k \tag{3.39}$$

$$\frac{D\rho\omega}{Dt} = \frac{\partial}{\partial x_j}\left[\left(\mu + \frac{\mu_t}{\sigma_\omega}\right)\frac{\partial \omega}{\partial x_j}\right] + G_\omega - Y_\omega + D_\omega \tag{3.40}$$

$$\mu_t = \frac{\rho k}{\omega}\frac{1}{\max\left(\frac{1}{\alpha^*}, \frac{SF_2}{\alpha_1\omega}\right)} \tag{3.41}$$

$$\sigma_k = \frac{1}{F_1/\sigma_{k,1} + (1-F_1)/\sigma_{k,2}} \tag{3.42}$$

$$\sigma_\omega = \frac{1}{F_1/\sigma_{\omega,1} + (1-F_1)/\sigma_{\omega,2}} \tag{3.43}$$

$$\tilde{G}_k = \min\left(-\rho\overline{u_i'u_j'}\frac{\partial u_j}{\partial x_i}, 10\rho\beta^* k\omega\right) \tag{3.44}$$

$$G_\omega = -\frac{\alpha}{\nu_t}\rho\overline{u_i'u_j'}\frac{\partial u_j}{\partial x_i} \tag{3.45}$$

Because the model is using a k–ϵ formulation in the outer region, a cross diffusion term appears as the k–ϵ–model is transformed into a k–ω formulation. This term is given as:

$$D_\omega = 2(1-F_1)\rho\sigma_{\omega,2}\frac{1}{\omega}\frac{\partial k}{\partial x_j}\frac{\partial \omega}{\partial x_j} \tag{3.46}$$

The diffusion terms (Y_k and Y_ω), as well as the model constants are excluded here. A complete description of the turbulence model is found in the Fluent user guide, or in the Menter article [16] [8].

The Spalart–Allmaras model

The Spalart–Allmaras turbulence model is a one–equation model that has been designed specifically for aerospace applications, and it is therefore a model of choice regarding wall–bounded flows. It has also proven to yield good results for boundary layers with adverse pressure gradients.

As a one equation model it has certain shortcomings regarding abrupt changes from wall–bounded to free shear flow and prediction of the decay of homogeneous isotropic turbulence. However, the model has given promising results for turbomachinery applications [8].

The model uses a modified turbulence viscosity as the transported variable, the transport equation given as:

$$\frac{D\rho\tilde{\nu}}{Dt} = G_\nu + \frac{1}{\sigma_{\tilde{\nu}}}\left[\frac{\partial}{\partial x_j}\left((\mu + \rho\tilde{\nu}\frac{\partial\tilde{\nu}}{\partial x_j}\right) + C_{b2}\rho\left(\frac{\partial\tilde{\nu}}{\partial x_j}\right)^2\right] - Y_\nu \tag{3.47}$$

$$\mu_t = \rho\tilde{\nu}\left(\frac{(\tilde{\nu}/\nu)^3}{(\tilde{\nu}/\nu)^3 + C_{v1}^3}\right) \tag{3.48}$$

In the model, G_ν is the production of $\tilde{\nu}$ and Y_ν is the destruction. Model constants and equations for the production and destruction of $\tilde{\nu}$ can be found in the Fluent user guide [8]. The modified turbulence viscosity is set to zero at walls.

3.3.3 Boundary conditions

Inlet and outlet boundary conditions

In order to close the equations in a CFD problem, boundary conditions have to be determined. At the inlet, flow velocity and turbulent properties are normally set. The flow velocity in this problem is known from the measurements. Apart from that, two turbulence properties needs to be set in order to close the two turbulent transport equations. Here this is done by specifying a turbulence intensity (TI) and a turbulent viscosity ratio ($\hat{\nu}$). The turbulent intensity is defined as the root mean square value of the velocity fluctuations, divided by the mean flow velocity [8]. With the Boussinesq assumption of isotropic turbulence, one gets:

$$k = \frac{2}{3}(U_\infty TI)^2 \tag{3.49}$$

The turbulent viscosity ratio is defined as the ratio between the turbulent and the molecular viscosity. It is normally given as $\hat{\nu} = \mu_t/\mu$, or in terms of the kinematic viscosity, as the flow is incompressible. The relationship between the spesific dissipation rate and the turbulent viscosity ratio is given as:

$$\omega = \rho\frac{k}{\mu}\left(\frac{\mu_t}{\mu}\right)^{-1} \tag{3.50}$$

Knowing the spesific dissipation rate, the dissipation rate (ϵ) can be found using equation 3.31.

At the outlet a static pressure was set. Compared to a determination of the outflow velocity or velocity angle, this method is known to give better convergence in case backflow occurs. In case backflow occurs, turbulent properties needs to be determined for this 'inflow'. This was done by determining a high turbulence intensity while keeping the viscosity ratio determined at the inlet.

Periodic boundary condition

When the wind turbine is modelled, the flow is assumed to be rotationally periodic. This is a valid assumption as long as the wind tunnel is modelled as a circular tube, and the influence from non–rotational geometries (like the wind turbine tower or hub irregularities) are excluded. This has been done in the three dimensional simulations in order to reduce the size of the numerical model to one third of the physical model.

The periodic boundaries are placed 120° apart, with one wind turbine blade placed in between. The boundaries are specified so that there is no pressure drop across them. When calculating flow variables at one cell at the periodic boundary, its neighbor cell on the other side of the boundary will be the cell adjacent to the opposite periodic boundary [8]. Explained in another manner, the flow into one periodic boundary will flow out of the opposite one.

Wall boundary condition

Wall boundaries are determined so that there are no velocity components normal to the wall. The velocity gradient close to the wall can be specified directly, or the no–slip condition can be applied.

All viscous flows are significantly affected by the presence of walls. For physical, non–moving walls, the no–slip condition has to be fulfilled. This gives rise to a shear, affecting both the velocity and the turbulent properties of the flow. While the k–ω–model can be applied throughout the boundary layer, the k–ϵ models are only valid for fully turbulent flow. This is problematic in the viscous sublayer, wheree the viscous stresses are dominant.

There are two main ways of achieving boundary conditions for wall–bounded flows.

- *The wall–function approach* uses the law of the wall, and semi–empirical relations to determine the velocity and turbulent properties in the logarithmic region. This reduces the refinement close to the surface, resulting in faster computations.
- *The near–wall model approach* uses grids that resolves the viscous sublayer, and uses formulas for near–wall turbulent quantities. The need for a fine mesh increases the computing time, but the approach is known to give better results, especially for low–Reynolds–number flows.

For most high Reynolds–number flows with finite wall shear, the law of the wall is valid for a thin region close to the surface. The viscous sublayer and the logarithmic layer both has well–defined velocity distributions under these conditions, that are used to determine the mean velocity close to the wall. In the viscous sublayer, ranging from $0 \leq y^+ < 5$ the velocity distribution is known to be given by $u^+ = y^+$. In the fully turbulent logarithmic layer $70 \leq y^+ < 300$, the velocity is known to be described by the logarithmic law $u^+ = \frac{1}{\kappa} \ln(y^+) + C^+$ [18].

The wall function approach is used by the k–ϵ–models, assuming that the dissipation rate and production of turbulent kinetic energy is in equilibrium in the logarithmic layer. This gives the

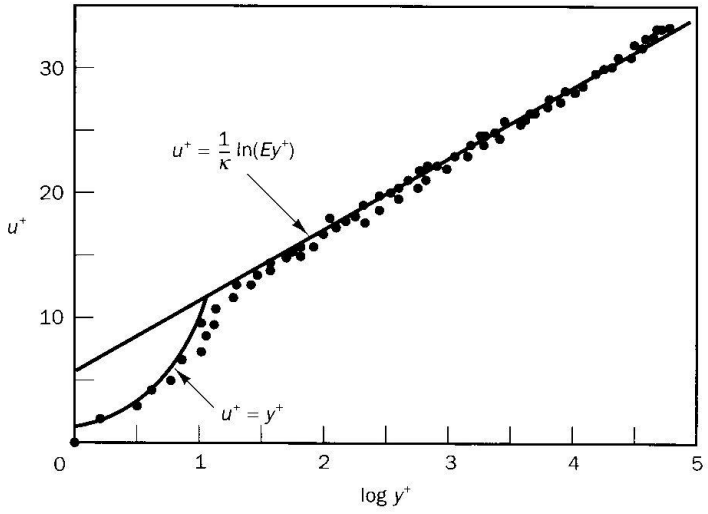

Figure 3.8: Schematic of the viscous sublayer. From Versteeg [26].

following relations for k and ϵ when using standard wall functions and boundary layer approximations [8]:

$$G_k \approx \tau_w \frac{\partial U}{\partial y} = \tau_w \frac{\tau_w}{\kappa \rho C_\mu^{0.25} k_p^{0.5} y_p} \tag{3.51}$$

$$\epsilon_w = \frac{C_\mu^{0.75} k_p^{1.5}}{\kappa y_p} \tag{3.52}$$

These so–called 'standard wall functions' can only be applied in the logarithmic layer, normally ranging from $30 \leq y^+ < 300$. If an attempt is made to solve the flow in the viscous sublayer, enhanced methods have to be used.

If the flow in the viscous sublayer is to be solved by the k–ϵ–model, a two–layer method is used. The flow is divided into a fully turbulent area where the original equations are used, and a viscosity–affected region where a one–equation model is used. The demarcation–line is defined as $Re_y \equiv \frac{y\sqrt{k}}{\nu} = 200$, where y is the distance from the wall. The one–equation model used in the viscous sublayer uses the the original formulation of the momentum– and k–equations. The turbulent viscosity is regarded proportional to the square root of k, and ϵ is regarded proportional to $k^{1.5}$. In between the two regions, blending functions are used to ensure smooth transition of quantities between the sublayer and the fully turbulent region [8].

The k–ω– and Spalart–Allmaras–models both use methods close to the wall that are insensitive to the position of the first cell. This is done by formulating the law of the wall as one single wall law for the entire near–wall region, including both the viscous sublayer and the logarithmic layer. This ensures a reasonable treatment if the first cell point falls in the buffer region. The turbulent kinetic energy at the wall is calculated using the same functions as for the standard wall treatment functions [8].

The enhanced wall treatment or enhanced wall functions are recommended in cases where the boundary layer needs to be resolved accurately. This is the case in this study, as viscous friction and correct

prediction of separation is an important factor when determining the forces acting on an airfoil.

3.3.4 Discretisation

In a numerical solution, the fluid and flow properties are normally calculated for all cell centers. But as we are using a Control Volume Method, the fluxes at the cell faces also need to be known. The fact that the solution is not continuous, forces us to use a differencing scheme. The most intuitive one is the 'central differencing scheme' that applies simple linear interpolation between values in the closest cell centers in order to find fluid properties at cell faces.

In a problem where convection is a dominant cause of transportation, this might not be appropriate. It is rather expected that the cell center value of a specific property will be more influenced by the corresponding value in the upwind cell than in the downwind. This fact has lead to the 'upwind differencing scheme' that takes the flow direction into account, and uses only upwind cell center values for interpolation at cell faces.

As the accuracy of the upwind differencing scheme is only first order in terms of truncation errors, it is vulnerable for numerical errors. However, first order schemes tend to be numerically stable, and suitable for initial simulations. In order to reduce the truncation errors, higher order differencing schemes must be used. FLUENT has the option for a 'second order upwind differencing scheme' and a QUICK scheme. Both these schemes have been used in the calculations.

The QUICK scheme uses quadratic interpolation, thus reducing the truncation errors. It is however more exposed to numerical divergence.

3.3.5 Numerical solution strategies

The equations governing a complicated fluid flow problem have no analytical solution. Numerical approaches must therefore be applied. As the equations 3.28 and 3.29 are coupled, they cannot be solved separately. One of the most common solutions strategies is called SIMPLE.

The procedure uses a guessed pressure field as the starting point (p^*). On the basis of this, the discretised momentum equations (3.28) are solved. The resultant velocity field does not necessarily satisfy the continuity equation, therefore the pressure and velocity fields must be corrected by a certain value to account for this ($p_{new} = p^* + p'$). In the end the rest of the transport equations are solved.

As the old value of a scalar (e.g. $p*$) is corrected by the term p', the equation is susceptible to divergence. The correction term might be too large, and the changes are normally damped by an under-relaxation factor. Due to this, the correction equation for the pressure is given as:

$$p_{new} = p^* + \alpha_p p' \tag{3.53}$$

where α_p is the under–relaxation factor. If this is kept at one, the solution is in danger of divergence. If it is kept close to zero, nothing will happen. The trick is to find the right value in order to speed up convergence without risking divergence.

The SIMPLE and SIMPLEC algorithm are both used in this project. The differences between them are marginal, and further information can be found in Versteeg [26].

Chapter 4

Experimental results

4.1 Experimental setup

The turbine examined in this project has been developed for testing in the NTNU wind tunnel. The wind tunnel has a cross section of 2.7 m x 1.9 m, and a test section approximately 11 m long.

The wind turbine blades are connected to a rotating nacelle. The blades can be pitched about the blade quarter chord, but this pitch angle ($\Delta\theta$) was set to zero in the experiment. This nacelle is connected by an axis to a transmission belt that is attached at the rear of the hub. This transmission belt transfers the moment to a generator mounted beneath the wind tunnel floor. The generator is connected to a full–frequency converter, making it possible to control the rotational speed of the rotor. A torque gauge is mounted in the hub in order to measure the moment on the transmission axis. This data was logged by a computer.

The nacelle and blades are mounted on a cylindrical hub. This hub has a diameter of 0.09 metres and is 0.56 m long. Thorough measurements of the geometry was performed, and the hub was later modelled in GAMBIT.

The hub is mounted on a tower that consists of several cylindrical elements with different diameters mounted on top of each other. The frontal area of the tower is approximately 0.053 m^2. The tower height was measured to be 0.82 m high, keeping the tip of the blade 0.37 m from the nearest wind tunnel wall. This distance is thought to be enough to prevent the blades from entering the wind tunnel boundary layer.

The wind turbine was mounted on a weight that can measure forces in three dimensions. However only the thrust force was measured. The thrust gauge readings was logged by a computer.

The free stream velocity was measured using a pitot tube. The measurements was taken upstream of the wind turbine, some distance to the side, in order to escape the influence of the wind turbine.

All measurements was logged at a frequency of 500 Hz, with a logging time of 15 s. This resulted in a total number of samples of 7500. Both mean values and standard deviations (σ) were collected.

The temperature was measured using a regular digital thermometer and the total (atmospheric) pressure using a weatherglass.

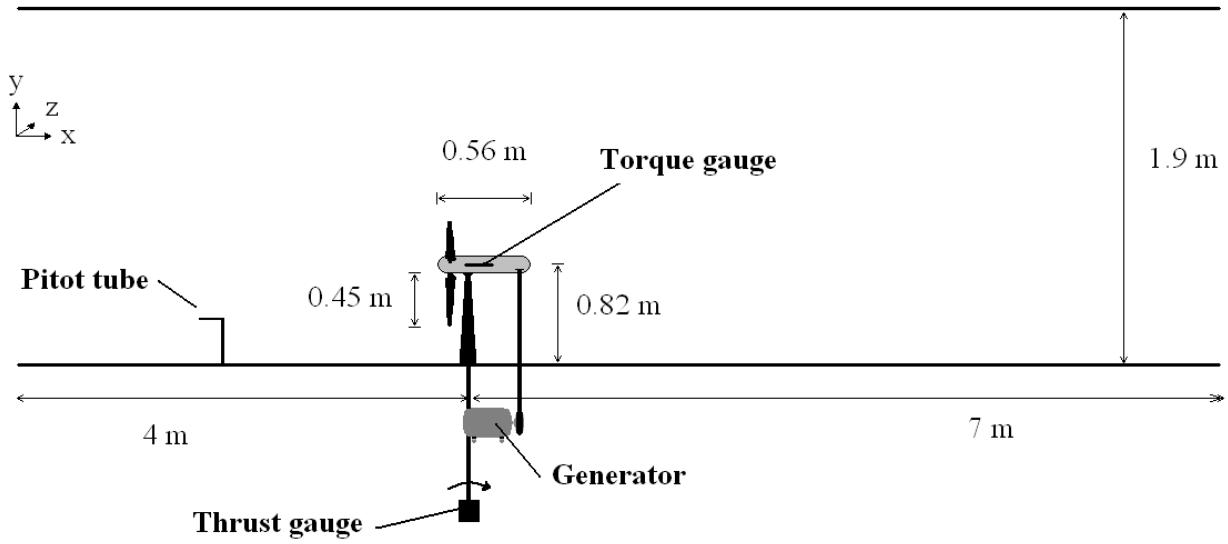

Figure 4.1: A schematic of the experimental setup in the wind tunnel

4.2 Calibration

The pitot tube calibration curve was already known, but the torque and thrust gauges had to be calibrated. This was done using weight elements with a known mass. The sensors are known to respond linearly to increased torque and thrust forces. Linear regression was used to obtain the correct relation between the sensor signals and the real forces acting on the turbine. The calibration curves and data can be found in appendix A.1.

10 and 14 measurements were conducted for the torque and thrust sensor respectively. The calibration results yielded a correlation of 0.9999 and 0.9995 respectively, thereby the systematic error can be expected to be rather small.

4.3 Results

Measurements of the total pressure and temperature were done. This made it possible to estimate the density of the air using the ideal gas law. Combined with the dynamical pressure measured by the pitot tube, the wind speed in the wind tunnel was found:

$$U_\infty = \sqrt{2\frac{q_\infty}{\rho}} \tag{4.1}$$

Knowing the rotational velocity, the tip speed ratio was determined.

The torque and thrust forces were measured directly, and the coefficients of performance was calculated using the known free stream velocity, density and the rotor area. The calculations was done using equation 3.1 and 3.2.

A free stream Reynolds number based on the rotor diameter was obtained. The mean kinematic

viscosity measured in the wind tunnel was determined using Sutherlands equation that can be used for air for temperatures below 3000 K [4]:

$$\mu = 1.458 \cdot 10^{-6} \frac{T^{1.5}}{T + 110.4} \tag{4.2}$$

	Mean	σ	**Max**	**Min**
Velocity	9.97 m/s	0.165 m/s	10.56 m/s	9.87 m/s
Total pressure	99.97 kPa	-	-	-
Density	1.173 kg/m^3	0.002 kg/m^3	1.176 kg/m^3	1.1704 kg/m^3
Temperature	23.848°C	0.404°C	24.4°C	23.0°C
Reynolds number	6.38x10^5	0.12x10^5	6.77x10^5	6.31x10^5

Table 4.1: Mean, maximum and minimum values, as well as the standard deviation of the results in the wind tunnel experiment.

The Reynolds number can then be found from equation 4.3 and the ideal gas law, based on the velocity upstream of the wind turbine, the wind turbine diameter (d), the pressure and the temperature:

$$Re = \frac{Ud}{\mu} \frac{p}{RT} \tag{4.3}$$

Measurements were done with varying rotational speed of the wind turbine, keeping all other parameters constant. A small temperature rise was observed during the experiment. This changes the density and viscosity of the air somewhat, but was observed to have only a small effect on the wind tunnel Reynolds number. The temperature rise is quite normal, as some of the work done by the wind turbine fan is transformed into heat, making the temperature in the wind tunnel rise.

The measured values of the torque and thrust forces was used to generate a C_P and C_T curve.

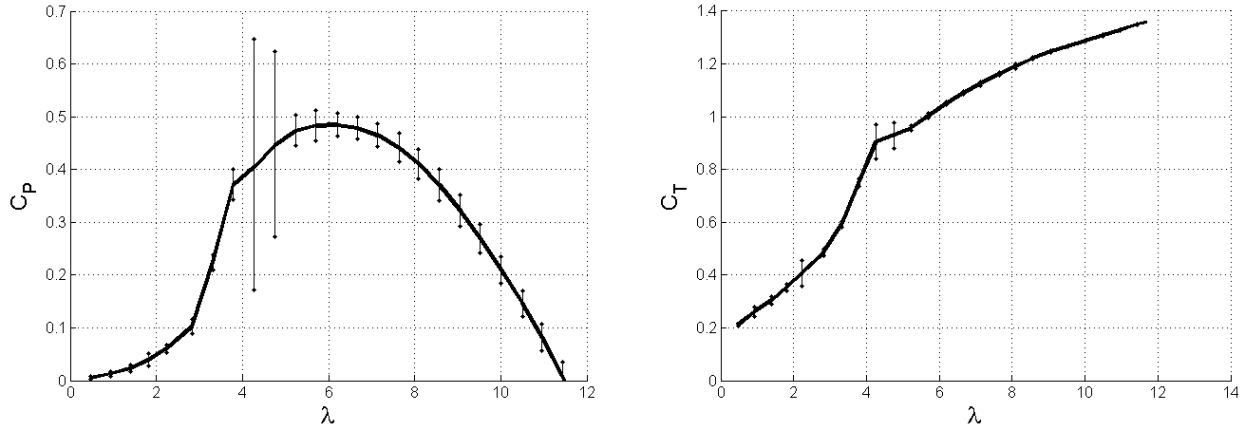

Figure 4.2: Measured C_P and C_T curves. The bars indicate the measured standard deviation.

The standard deviations are indicated in figure 4.2. It is clear that there are some considerable dynamic effects causing large fluctuations in both torque and thrust forces between $\lambda = 4$ and $\lambda = 5$. As the tip speed ratio was reduced below 5, we know that the local angle of attack is increasing over the blade. As the efficiency of the wind turbine is reduced here, this could indicate that the dynamic effects are related to separation.

It is important to notice that the method of changing the rotational speed of the wind turbine makes Reynolds number effects more dominant, compared to a case where the rotational speed was kept constant, with a varying free stream velocity. For most tip speed ratios above 2 (where the relative inflow angle at the tip is less than 30°), the Reynolds number at the tip will to a large extent be determined by the rotational speed. This makes the tip Reynolds number in this experiment vary with a factor of 10 (see figure 7.1).

A more thorough investigation of these results will be done using the BEM method and CFD simulations.

Chapter 5

2D airfoil charateristics

A numerical study of flow patterns around a wind turbine is a three dimensional exercise, with a high demand for computational power. This demand calls for thorough initial studies, in order to increase the success ratio of the numerical experiments. Failed three dimensional simulations are time–consuming; learning is faster and less frustrating in two dimensions.

5.1 Airfoil characteristics

The NREL s826 airfoil that has been used in the design and production of the wind turbine blades in question is designed for Reynolds numbers in the order of $2.0 \cdot 10^6$. The design is made so that the airfoil should be insensitive to leading edge roughness. This is done by putting a highly curved part on the suction side, close to the leading edge. This curvature will cause a suction peak to appear, promoting transition close to the leading edge, independent of surface roughness or free stream turbulence. This way the boundary layer will be turbulent over most of the suction side of the airfoil.

In the range of Reynolds number expected in the wind tunnel experiments, this suction peak will probably cause laminar instability, but due to the low Reynolds number, the flow might remain laminar over a larger portion of the airfoil. Because of the high airfoil curvature, this is expected to result in laminar separation for certain angles of attack.

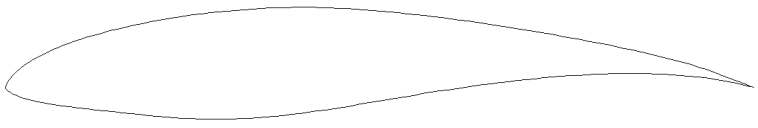

Figure 5.1: The NREL s826 airfoil. The high airfoil curvature near the leading edge can be seen at the airfoil nose.

The airfoil is also equipped with a separation ramp near the trailing edge; a feature often found on wind turbine profiles. It can be seen on the suction side very close to the trailing edge, where the downward slope of the airfoil is increased. The flow over this ramp will experience an increased adverse pressure gradient, making separation more likely to happen here. This might sound peculiar, but this is the core of the rationale behind this design. As the pressure increase over this ramp is high, the adverse pressure gradient over the rest of the airfoil suction side can be lower, reducing

the possibility of separation. If the flow separates, the separation will tend to be confined to the separation ramp area, reducing the dynamic stall effects. This has proven to be an effective way of reducing dynamic loads on stall regulated wind turbines.

This trap both makes separation occur quite early but also delays full stall. Because separation tends to alter the effective shape of the airfoil, this will tend to smooth lift and drag curves, causing stall to happen more smoothly. This is favorable, as a wind turbine exposed to turbulent inflow will experience large variations in local angle of attack.

The airfoil is cambered, and will therefore generate lift at zero angle of attack.

In lack of experimental data, results from XFOIL has been used as an input for BEM calculations and comparison with CFD results. XFOIL is known to give accurate results for airfoils within a large range of Reynolds numbers. Studies have shown that XFOIL is able to predict airfoil forces quite accurately, even though the actual position of the transition point or the spatial extent of separation bubbles might not be correctly predicted at low Reynolds numbers [29] [25].

5.2 XFOIL study

5.2.1 Analysis of transition criteria

In order to examine the airfoil performance in an efficient manner, XFOIL was used to generate lift and drag curves for different Reynolds numbers and transition criteria. Choosing a reasonable transition criteria is important because the actual position of the transition point has a large influence on airfoil performance.

The flow around a smooth airfoil of infinite length moving in still air is known to transist from laminar to turbulent flow as soon as the level of disturbances exceeds a certain limit. The transition point can be predicted with a reasonable accuracy by using the e^n–criteria, where n or $Ncrit$ is the amplification factor of the most–amplified frequency which triggers transition [18]. The recommended value for $Ncrit$ is normally 9. This method is only appropriate in situations where the growth of two–dimensional Tollmien–Sclichting waves are the dominant cause of the transition.

However, this is not expected to be the case for the flows examined in this study. There are three main effects that most probably will cause transistion to occur considerably closer to the leading edge than what is the case in the idealised two dimensional case mentioned above.

1. The flow around the wind turbine is swirling, where substantial three–dimensional effects are present. These effects will most probably disturb the two–dimensional Tollmien–Schlichting waves, dictating a different path to transition.
2. The turbulence level in the wind tunnel is expected to be in the order of 0.7% [9], introducing external disturbances that will hasten the transition.
3. The wind turbine blades are not completely smooth, and have some small edges and scratches near the leading edge. In case this roughness turns out to be a cause of transition, the linear instability theory will fail to predict the transition point [4].

Depending on the magnitude of these disturbances, transition might occur quite close to the leading edge, forcing a turbulent flow regime over most of the airfoil.

The effects of rotation on transition are very hard to determine. There are indications that rotation might hasten transition due to introduction of three dimensionality. However, this effect has been excluded in the following discussion. Only the two last effects will be discussed. In order to mimic the effect of roughness or free–stream turbulence the amplification factor can be given a lower value. This will cause transition to occur closer to the the point of laminar instability, thus imitating the other physical effects.

By varying the transition criteria, l/d curves were calculated for three different Reynolds numbers.

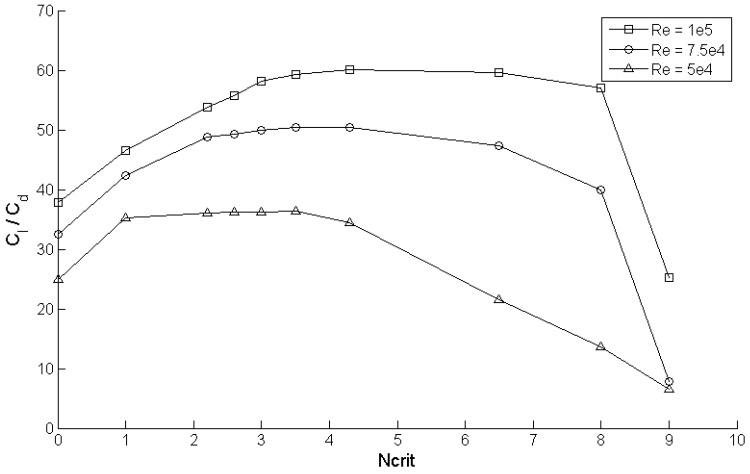

Figure 5.2: L/D–ratios for s826 at $\alpha = 7°$ with varying $Ncrit$ and varying Reynolds numbers.

Figure 5.2 shows how both conservative (high $Ncrit$) and progressive (low $Ncrit$) transition criteria gives reduced lift to drag ratios. When $Ncrit$ is given a high value, laminar separation will occur on both sides of the profile for most angles of attack. This will deform the effective shape of the airfoil and significantly reduce the airfoil performance.

When $Ncrit$ is given a low value, the flow is turbulent over most of the airfoil. The lift is not much altered, so the increased viscous drag accounts for most of the l/d reduction.

It is clear from figure 5.2 that we face an airfoil efficiency reduction as the Reynolds number is reduced, regardless the transition criteria. A reduction of the Reynolds number do by definition imply that viscous effects becomes more dominating, increasing viscous drag. In addition the thickness of the boundary layer will increase with decreasing Reynolds number, deforming the airfoil, leading to increased form drag or less lift.

The Reynolds number effect will be important when calculating the wind turbine performance.

5.2.2 Lift and drag curves

On the basis of figure 5.2, three different transition criteria were used in the further studies; $Ncrit = 0.01$ with more or less instant transition. $Ncrit = 3.0$ was chosen for a moderate case, somewhere in between. Ultimately, $Ncrit = 9$ was chosen as the other 'extreme'. These was used to produce L/D–ratios for different angles of attack with a Reynolds number of $1.0 \cdot 10^5$.

The presence of laminar separation bubbles in the case where $Ncrit$ is set to 9 is clear from figure 5.3. For moderate angles of attack the deformation of the airfoil tend to both increase the drag and

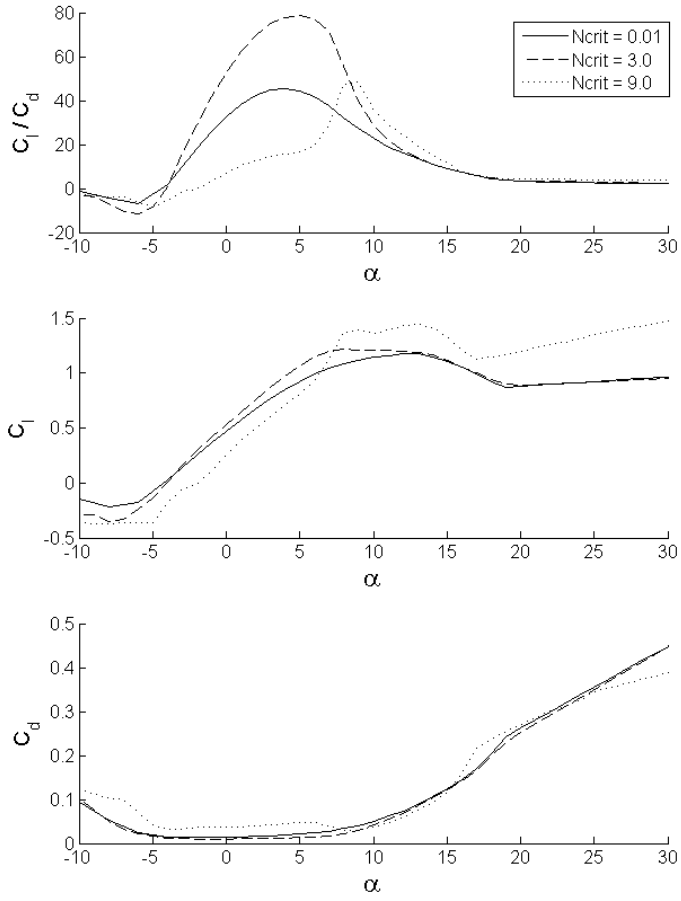

Figure 5.3: L/D–ratios, lift and drag coefficients for different α, using three different transition criteria. Re = $1.0 \cdot 10^5$

reduce the lift. A typical laminar separation bubble can be seen in figure A.1 in the appendix.

As seen in figure 5.3, the airfoil has a somewhat better performance with conservative transition criteria ($Ncrit = 9.0$) in the early stall area ($10° < \alpha < 15°$). This is caused by the presence of a laminar separation bubble near the leading edge. In this bubble, the pressure gradient is very small, maintaining a lower pressure over a larger portion of the airfoil. This way the effective curvature of the airfoil leading edge is reduced, reducing the adverse pressure gradient. This moves the actual separation point closer to the trailing edge, compared to a case where transition occurs before laminar separation. Thus, the lift is increased. However, as the angle of attack exceeds 15°, the laminar bubble burst, resulting in full stall from the leading edge. As the stall will be very abrupt, this kind of stall can result in severe dynamic effects. Detailed graphs and figures of this transition procedure is found in appendix A.4.

The $Ncrit = 3.0$ regime is also affected by laminar separation, seen as an increase in lift for moderate angles of attack. However, no dramatic stall is observed here.

In the wind turbine case, it seems clear that a $Ncrit$ of 9 is too conservative. The presence of rotation, free–stream turbulence and roughness will most probably force transition to occur before the

Tollmien–Schlichting linear instability occurs for moderate angles of attack. It is therefore expected that a lower $Ncrit$ will imitate the actual processes more actually.

Assuming the transition to occur near the leading edge for all angles of attack might be a to progressive choice. However, an analysis of all three cases might be interesting when comparing the BEM results to the experimental data.

5.3 CFD study

5.3.1 Methods

A 2D model of the NREL s826 airfoil was made using GAMBIT. The numerical domain was extended $12.5C$ upstream and $20C$ downstream of the airfoil. These are recommended values used in several studies in the literature, and the solutions sensitivity to the size of the numerical domain was therefore not tested. A structured grid was used close to the airfoil, while both structured and unstructured grids was used in the rest of the numerical domain.

The CFD–study was performed in FLUENT, with a focus on examination of how different turbulence models and grid resolutions affected the solution. This was done in order to reduce the computational effort in the three dimensional case. The sensitivity to the following parameters was tested:

- Choice of turbulence model
- Freestream turbulence level sensitivity
- Grid resolution sensitivity
- Reynolds number sensitivity

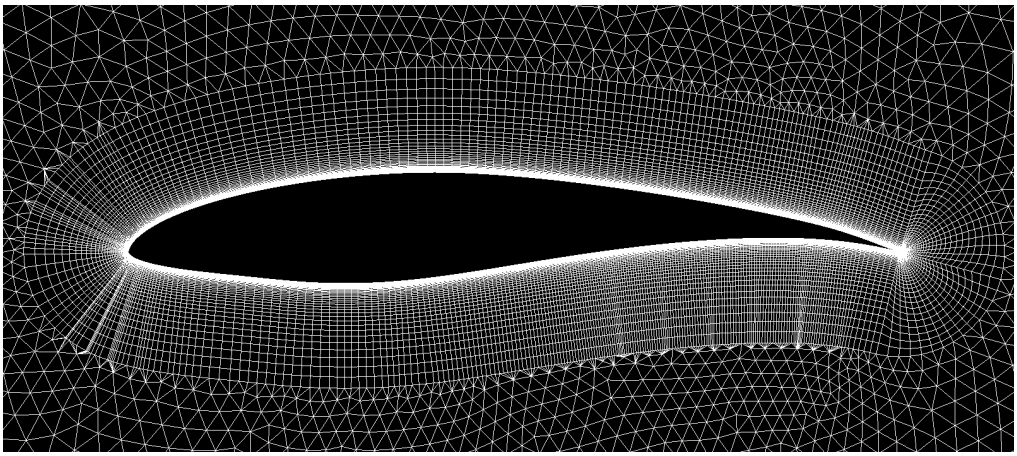

Figure 5.4: The 'O I' grid that has been used in the two dimensional studies of the NREL s826 airfoil.

A Reynolds number of $1.0 \cdot 10^5$ was used in the CFD–calculations if not stated otherwise. This was achieved by adjusting the fluid viscosity and density, keeping the inflow velocity at 10 m/s in all simulations.

A turbulence intensity between 1.0% and 0.5% is expected in the wind tunnel [9]. As a base case, the turbulence intensity close to the airfoil was put set to 1% in most of the calculations. It was later shown, as seen in figure 5.6, that the fully turbulent solutions showed little sensitivity to the free stream turbulence level. A turbulence viscosity ratio was also defined at the inlet. It was defined using the approximation $\epsilon = 2k$ in order to ensure that the turbulence level was decreasing as the flow approaced the airfoil.

The outlet was set as a constant pressure boundary, and the airfoil surface as a smooth wall. Both standard wall functions and enhanced wall treatment were used.

The SIMPLE algorithm was used to couple the pressure and velocity field, and 2. order upwind differencing schemes was applied on the flow variables. Only stationary solutions was obtained.

5.3.2 Grid resolution sensitivity

In order to solve the flow field around an airfoil, the grid needs to be fine enough to capture the flow gradients. As the flow gradients are generally larger close to solid surfaces, the cell size can generally be enlarged with distance from these surfaces.

A structured boundary layer grid was constructed close to the airfoil. This was done in order to ensure a good resolution of the boundary layer flow. A structured grid makes it easy to control of the transverse grid resolution close to the airfoil surface. It it possible to combine this with both a structured or an unstructured grid in the rest of the numerical domain. In the 3D-case, unstructured griding is preferable due to its simplicity. The downside of unstructured grids is the fact that the number of cells tends to increase. In addition unstructured grids tend to be more numerically unstable than structured grids. This calls for an thorough investigation of different griding possibilities, and further how this affects the solution.

An initial grid independence study was performed in order to be sure that the solutions obtained in the later sensitivity analyses were consistent. The grids used in the study are presented in table 5.1. The fully turbulent k–ω SST model was used in the calculations.

Using the six different grid presented in table 5.1, lift drag polars were created using the SST–model. The results are presented in figure 5.5. It is clear that there is an outstanding consistency between the CFD simulations and the XFOIL results. The solution seems to be independent of the grid resolution, apart from grid 'O IV'. Examining table 5.1, there is a strong indication that the chordwise grid resolution has not been good enough.

Chordwise grid resolution

As there are chordwise flow gradients over the airfoil surface, it is important that there are enough cells on the airfoil surface. First of all, the airfoil geometry needs to be captured. Second, the chordwise flow gradients needs to be captured. Because of this, several grid–points are needed in areas of high curvature and in areas with high rates of change in the chordwise direction. This applies to the leading and trailing edge, as well as close to separation– and reattachment–points. As

Grid	**C I**	**C II**	**O I**	**O II**	**O III**	**O IV**
# cells	41 000	100 000	27 188	19 570	18 920	17 473
# nodes on airfoil	210	300	366	248	248	141
# nodes normal to airfoil	100	200	-	-	-	-
y_p	$10^{-4}C$	$10^{-4}C$	$10^{-4}C$	$10^{-4}C$	$2 \cdot 10^{-4}C$	$2 \cdot 10^{-4}C$
Nodes in BL	-	-	45	35	30	30
BL growth rate	-	-	1.12	1.12	1.15	1.15
BL height	-	-	$0.136C$	$0.043C$	$0.087C$	$0.087C$

Table 5.1: Grid parameters for grids used in the fist part of the grid sensitivity study. There are two structured C-shaped grids (C I and C II), and four unstructured grids with a structured O-grid wrapped around the airfoil (O I - O IV).

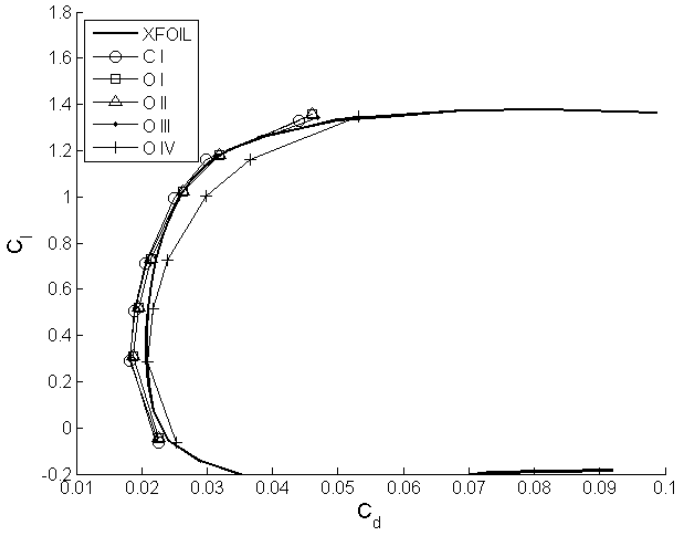

Figure 5.5: Initial grid independence study. The XFOIL results has been obtained using a *Ncrit* of 0.01 to indicate turbulent flow.

separations and reattachment–points move with the flow conditions, the grid was only refined toward the leading and trailing edge.

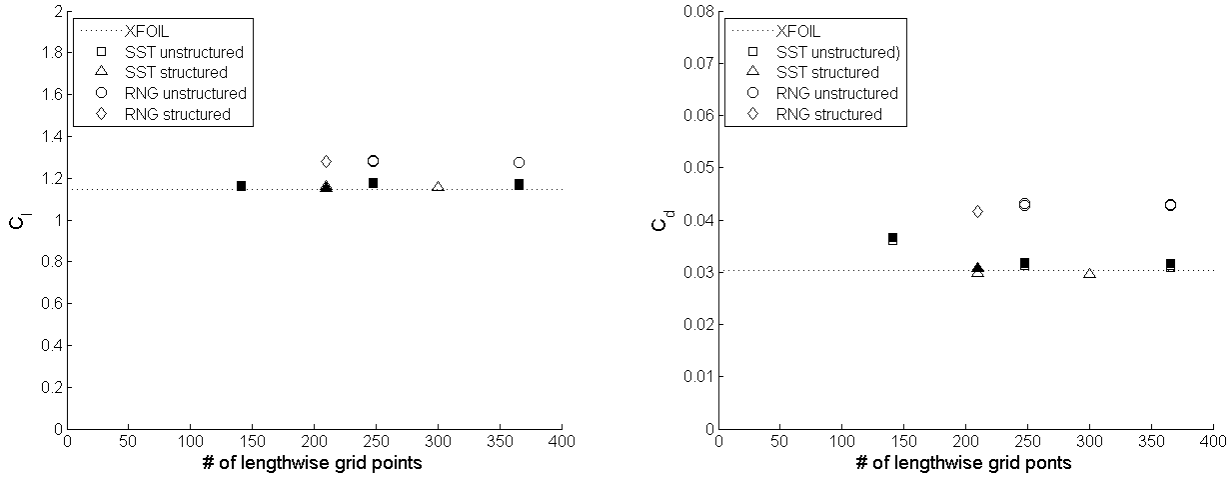

Figure 5.6: Lift and drag coefficients for grids with different number of grid points on the airfoil surface. The filled and open figures are indicating calculations with a TI at the airfoil of 1 % and 0.2 % respectivly.

Examining the results obtained from the initial study, one sees that the number of grid–points on the airfoil were varying from 366 to 141. The results are presented in figure 5.6. It is clear that grid 'O IV' is unable to predict the correct drag coefficient. As seen from table 5.1 The main only difference between grid 'O III' and 'O IV' is the number of cells representing the airfoil surface. This indicates that at least 200 cell points should be used to get a good representation of the airfoil geometry, and to capture all effects in the spanwise direction.

As expected, the lift calculations are not very sensitive to the resolution of the boundary layer flow. The pressure–distribution around the airfoil is given by the continuity equation, and is only indirectly

coupled with the boundary layer state. The skin friction coefficient is determined by the velocity gradient at the surface ($\frac{dU}{dy'}|_w$). As the solution of the flow details in the boundary layer is much more elaborate than the estimation of the displacement thickness, the errors will generally be larger when calculating the drag than the lift.

Even though the solutions are fully turbulent, some sensitivity to free stream turbulence intensity level is expected. Two sets of solutions were obtained using a free stream TI at the airfoil position of 0.2% and 1% respectivly. The solutions showed very little sensitivity to freestram turbulence level, as shown in figure 5.6.

Transverse resolution in the boundary layer

In order to get a good representation of the viscous drag it is recommended to use enhanced wall treatment to get a more accurate representation of the boundary layer flow [8]. These methods solves the viscous sublayer in the boundary layer flow, as explained in chapter 3.3.3. The viscous sublayer is known to extend up to $y^+ \approx 5$. If this should be resolved, the dimensionless distance from the wall to the first grid–point (y_p^+), should be below this value over the whole surface. The literature normally recommends $y_p^+ \approx 1$ [8].

The grid 'C I' was used to investigate this. Keeping all other parameters equal, the extension normal to the wall of the first cell (y_p) was varied. By using an angle of attack of 7° and a Reynolds number of $1.0 \cdot 10^5$, the lift and drag of the airfoil was calculated, and the maximum value of y_p^+ on the airfoil surface was found. The SST–model and the RNG–model was used with both standard and enhanced wall treatment. The SST–model has an implemented blending function that calculates the value of y^+ and applies the appropriate method. For the RNG–model, this needs to be defined in advance.

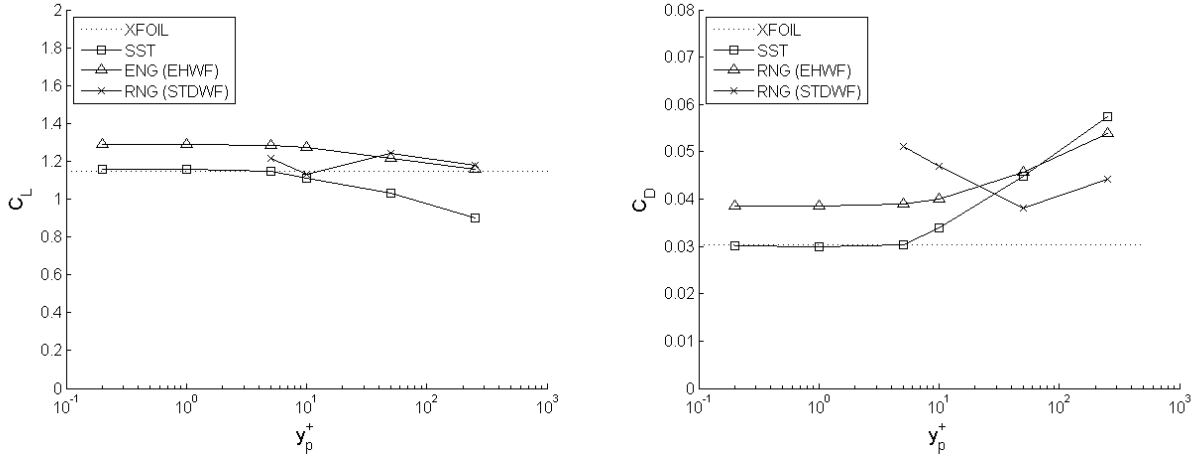

Figure 5.7: Lift and drag calculations with varying values of the maximum y_p^+ on the airfoil, keeping other parameters equal. Both the SST– and RNG–model has been used with two different wall treatments. In each calculation, the value of y_p is kept constant over the airfoil.

It is obvious that the maximum value of y_p^+ on the airfoil should be kept below 5, in order to get a grid independent result. This is consistent with recommendations in the literature. It is also obvious that when keeping y_p^+ below 300, a value recommended when using standard wall functions, the drag is overpredicted compared to the results from XFOIL. There are larger discrepancies in the drag– than in the lift–prediction.

In order to get good estimates for the lift and drag in the 3D case, the maximum value of y_p^+ on the airfoil should be kept below 5, and the mean value should be in the order of 1. For the Reynolds number examined here, this was achieved by keeping y_p less than $5 \cdot 10^{-4}C$, where C is the chord length of the airfoil.

5.3.3 Turbulence model sensitivity

In order to accurately predict the flow pattern around the airfoil, the turbulent nature of the flow needs to be modeled. Several models are available, all with known advantages and shortcomings. This two–dimensional study aims to compare three different turbulence models in order to find one appropriate for the three dimensional simulations. First a comparison of fully turbulent formulations will be made, followed by a small study of two of the models ability to predict laminar turbulent transition.

The Menter k–ω SST model is widely used for CFD wind turbine modeling [12] [21]. It is known to give good results in separated areas, and has proven to predict transition from laminar to turbulent flow and laminar separation bubbles quite accurately, an effect that is expected in this case [17]. The model can be run both as a fully turbulent model, or with a term predicting laminar turbulent transition.ling [12] [21]. It is known to give good results in separated areas, and has proven to predict transition from laminar to turbulent flow and laminar separation bubbles quite accurately, an effect that is expected in this case [17]. The model can be run both as a fully turbulent model, or with a term predicting laminar turbulent transition.

Fluent recommends the use of the k–ϵ–models for moderately swirling flows. Despite the improvements made by the use of RNG and Realizable theory, the problems related to the modeled equation of the dissipation rate ϵ are still known to cause problems in certain cases [8]. The RNG model involves the prediction of laminar turbulent transition by employing a differential formula for the effective viscosity, but as this has proven not to give good results, only the fully turbulent formulation will be used in the further studies.

The Spalart–Allmaras (SA) model was specifically designed for wall bounded flows in aerospace applications. It has proven to predict laminar turbulent transition fairly well, and works well in boundary layers with adverse pressure gradients [3] [8] [17]. It has also been used for turbomachinery applications. But, as a one–equation model it has certain shortcomings regarding accurate prediction of the turbulent length scale in cases of rapid changes (e.g when the flow changes from a wall–bounded to a free shear flow). There might be problems related to the swirling effects as well. The model will only be tested as a transisting model, as the fully turbulent formulation is not incorporated in FLUENT.

Fully turbulent flow

When modelling the flow as fully turbulent, the Boussinesq–approximation is valid in the entire flow–field. As seen from the turbulence model equations, this implies a positive value of μ_t, causing a higher effective viscosity over the airfoil than what is expected in reality. This means that laminar boundary layers will not exist in such a solution, causing higher skin friction and higher resistance to separation.

Only the k–ϵ RNG– and the k–ω SST–model were examined in this study.

The lift and drag calculations in figure 5.8 shows that the SST–model tends to give results that are

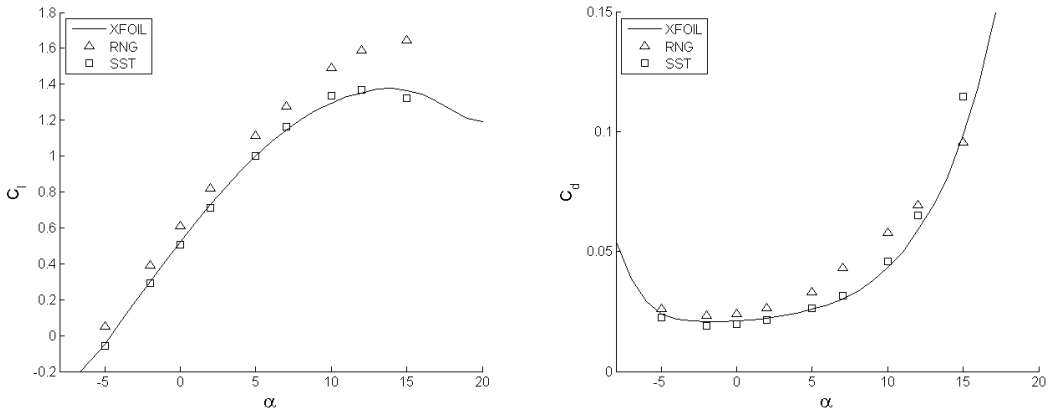

Figure 5.8: Lift and drag calculations with varying angles of attack using the RNG and SST turbulence model. The flow is regarded fully turbulent.

more consistent with the results from XFOIL for all angles of attack. The RNG–model overpredicts both lift and drag compared to the XFOIL results. The overprediction of drag could be related to the well–known deficiency related to overprediction of turbulent stresses in areas of rapid strain. The airfoil curvature is known to be problematic for the k–ϵ formulation.

It is clearly seen from figure 5.9, where the turbulent viscosity is severely overpredicted in front of the airfoil. This overprediction is related to the transport equation for ϵ, as the value of ϵ tends to zero upstream of the airfoil. Thereby the turbulent viscosity is increased. Both models use the same equation for production of mean kinetic energy in the high Reynolds number form, and it is clear that Wilcox claim that the transport equation for ϵ was too much of a drastic surgery on the original equations seems justifiable.

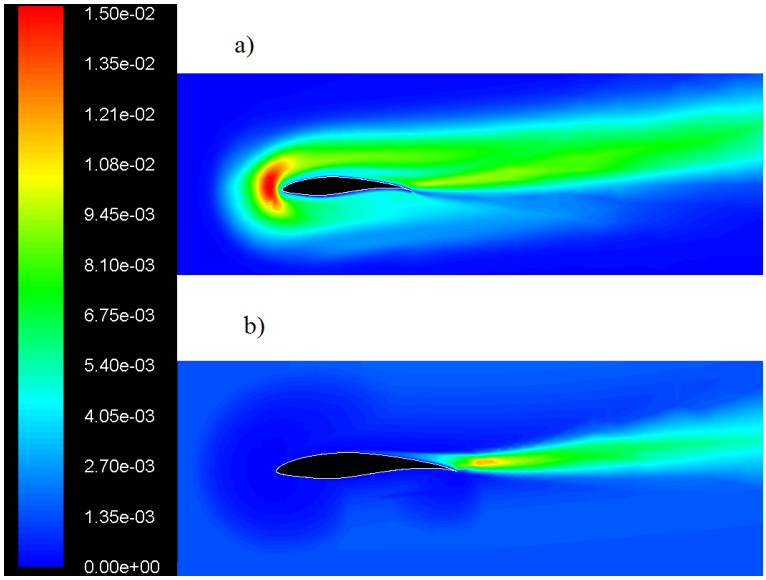

Figure 5.9: Contour plots of the turbulent viscosity calculated at α=10° and Re=$1.0 \cdot 10^5$ with a) the RNG–model and b) the SST–model.

Despite the overprediction of turbulent viscosity, figure 5.10 shows that both turbulence models predict the pressure distribution quite well. The RNG–model still overpredicts C_p over the whole

length of the airfoil, whereas the SST model gives a somewhat more consistent result. The main difference between XFOIL and the SST model is the prediction of the separation on the 'ramp' near the trailing edge where the SST–model predicts a separation.The result from XFOIL shows no sign of separation. This can be confirmed when examining the skin friction coefficient prediction of the different methods.

Because of the RNG–models inability to predict the turbulent quantities, the SST model will be applied in the further studies.

Transient flow

A description of the flow over the wind turbine blade as fully turbulent is not correct. The flow approaching the wind turbine will be close to laminar, making the flow at the leading edge laminar. In order to resolve the flow field, the turbulence model then has to take transition into account. The SST and the SA model do have this option in FLUENT, and a small series of numerical experiments was conducted in order to see if this could be included in the final simulations.

The inclusion of the laminar flow regime will lead to a reduced C_d for moderate angles of attack, as the viscous drag is reduced over certain parts of the airfoil. However, as the flow now is vulnerable to laminar separation, this effect can change the flow field a lot.

The turbulence intensity at the airfoil was kept at 1% in all simulations. For a two–dimensional flow over a smooth airfoil, this turbulence level should correspond to a $Ncrit$ in XFOIL of about 3.0 [6]. The CFD–simulations was then compared to the results from XFOIL.

The simulations revealed that a high number of cells was needed in order to capture the present effects. A structured grid with 100 000 cells was used as a reference. It was shown that there was a high demand for resolution in order to capture the transition with accuracy. In addition, the results revealed to be more unstable than fully turbulent flow. This is most probably because of the inherent instabilities in the laminar separation bubbles present for several flow conditions.

Because of the demand for grid refinement and difficulties regarding convergence, an inclusion of laminar effects in the final three dimensional simulations is regarded beyond the scope of this project.

5.3.4 Reduced grid sizes

The grids used in the initial grid sensitivity studies all had more than 15 000 cells in the numerical domain. It was clear that the resolution had to be drastically reduced in order to keep the number of cells in the three–dimensional grid within an acceptable range. It is also desirable to use an unstructured grid in order to make the griding process simpler. This calls for a thorough investigation of how the number of cells can be reduced with the smallest possible loss of accuracy.

A series of unstructured grids were then tested, in order to find the best way of reducing the number of cells. These grids consisted of between 5 000 and 9 000 cells, a significant reduction compared to the initial grids. The maximum value of y_p^+ on the airfoil surface was kept at 5, and the number of cells on the airfoil surface was set to 210. According to the initial studies, this should be sufficient.

The cell size in the numerical domain was controlled using one single size function, attached to the airfoil surface. The cells were allowed to grow to a maximum size of $2C$, some distance from the airfoil. The pace of this growth was set to be geometric, with a growth rate given in the figures.

Three of the grids from the initial study has been included in the figures. This has been done to quantify the loss of accuracy introduced by reducing the number of cells.

Three different grid parameters were investigated: (1) the effect of reducing the number of cells in the structured boundary layer grid. (2) the effect of reducing the height of the structured boundary layer grid, and (3) the effect of changing the geometric growth rate in the rest of the numerical domain.

The simulations was performed at an angle of attack of 12°, as the errors seem to grow with the angle of attack (see figure 5.8). The SST–model with a fully turbulent formulation was used, with a Reynolds number of $1.0 \cdot 10^5$. In order to isolate the effect of one change in grid parameter, all grid parameters but one was kept constant when a new grid was created. Thereby the effect of the change is always captured in the results. As the investigation resulted in more than 12 different grids, only the grid parameters of some grids are included in this report. They can be found in appendix A.5.

Figure 5.12 shows that the number of cells in the boundary layer grid can be reduced to approximately 15 without substantial loss of data. However, using 20 cells could improve the results somewhat. The height of the structured grid is a more important parameter, as can be seen from the figure. A height of $0.1C$ seems sufficient.

The geometric growth rate of the cells in the structured boundary layer is dictated by the height and the number of cells. The results were investigated in order to see if the solution was sensitive to this growth rate. No significant bias was found, indicating that the solution is not sensitive to the choice of this parameter.

As can be seen from figure 5.13, the choice of the geometric growth rate in the external domain is a crucial parameter. It should be set as low as possible, in order to get a better prediction of the drag acting on the airfoil. The lift is not very sensitive to the resolution, as expected. However, when keeping BLh at $0.1C$, the geometric growth rate can be increased to 1.45 before the results get as inaccurate as the $BLh = 0.05C$ results. This indicates that increasing the boundary layer height is an efficient way of achieving accurate results with few cells.

When constructing the three dimensional grid, an effort should be made in order to get the boundary layer height 0.1 times the longest chord length on the blade, with approximately 20 cells normal to the surface. Then a proper growth rate will be determined, so that the total number of cells are within an acceptable range.

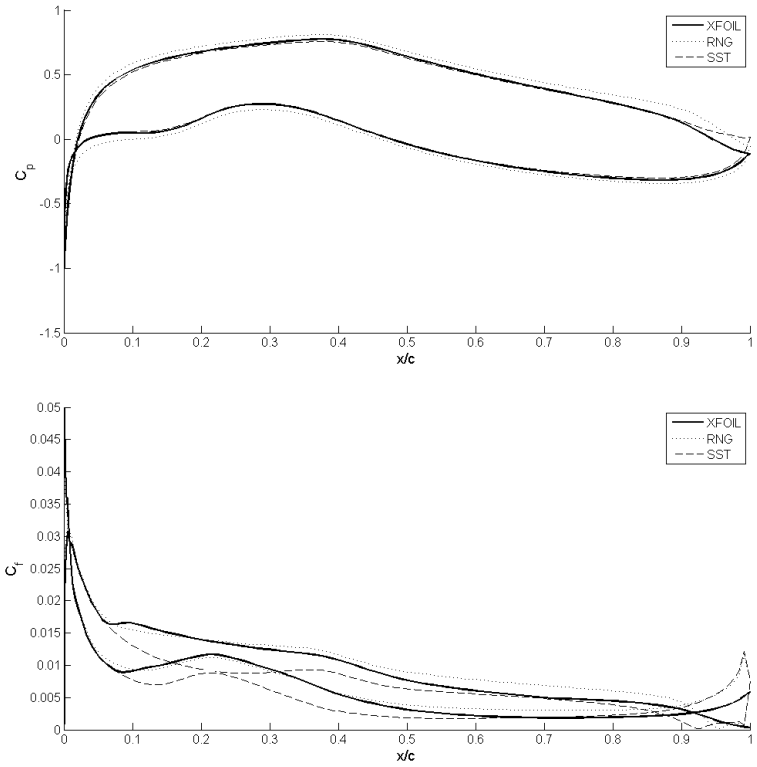

Figure 5.10: Pressure coefficient and skin friction coefficient from XFOIL calculation (Ncrit=0.01) and CFD, using fully turbulent flow and two different turbulence models. Re = $1.0 \cdot 10^5$ and $\alpha = 0°$.

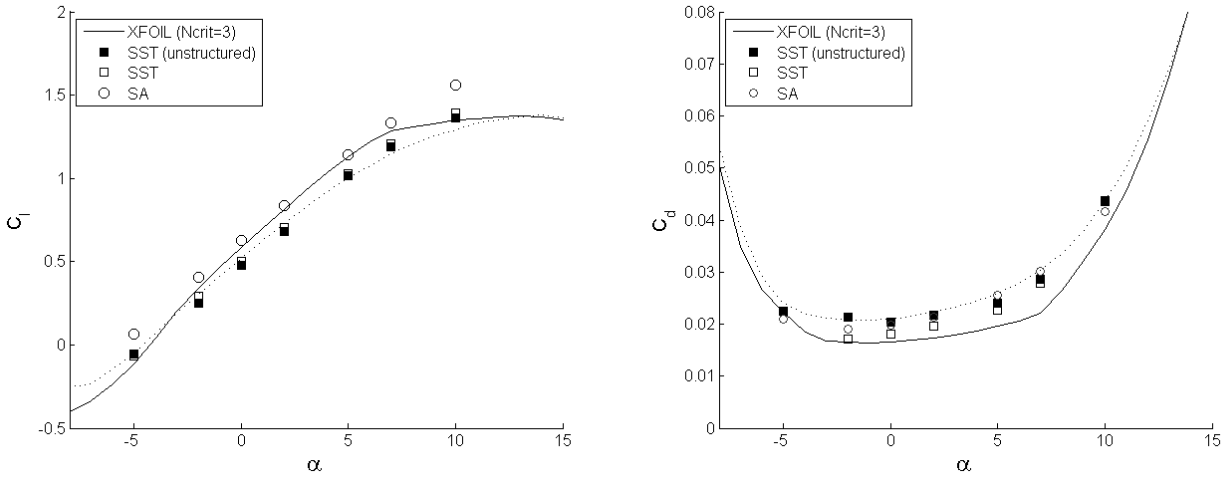

Figure 5.11: Lift and drag calculations with varying angles of attack using the SST and SA turbulence model with transition criteria. The calculations with the SST model has been done with both a structured (C II) and an unstructured grid (O I).

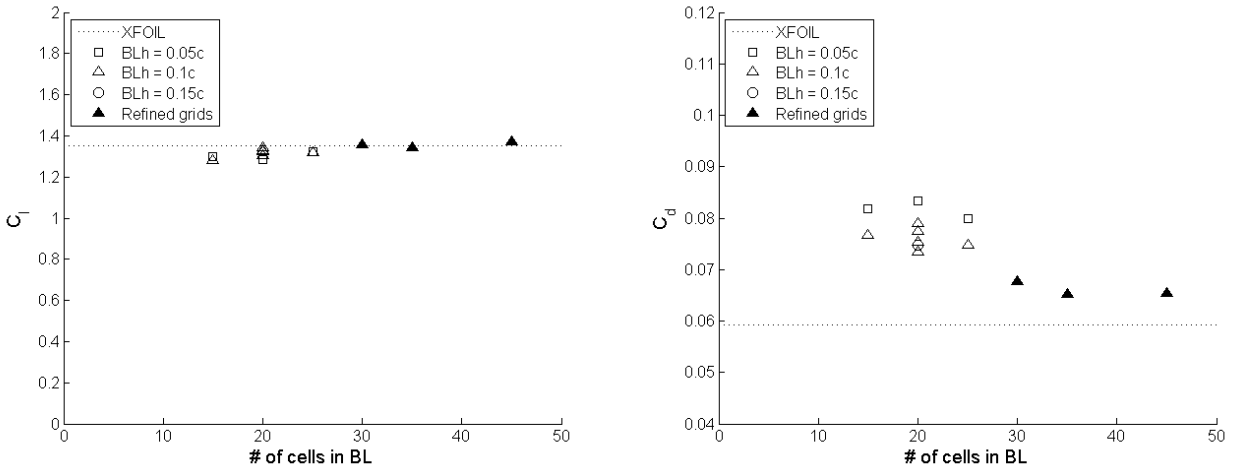

Figure 5.12: Numerical simulation results with varying number of cells in the structured boundary layer (BL) grid. Three results from the initial simulation with a refined grid is also included. The simulations are done with Re = $1.0 \cdot 10^5$, TI = 1.0% and $\alpha = 12°$.

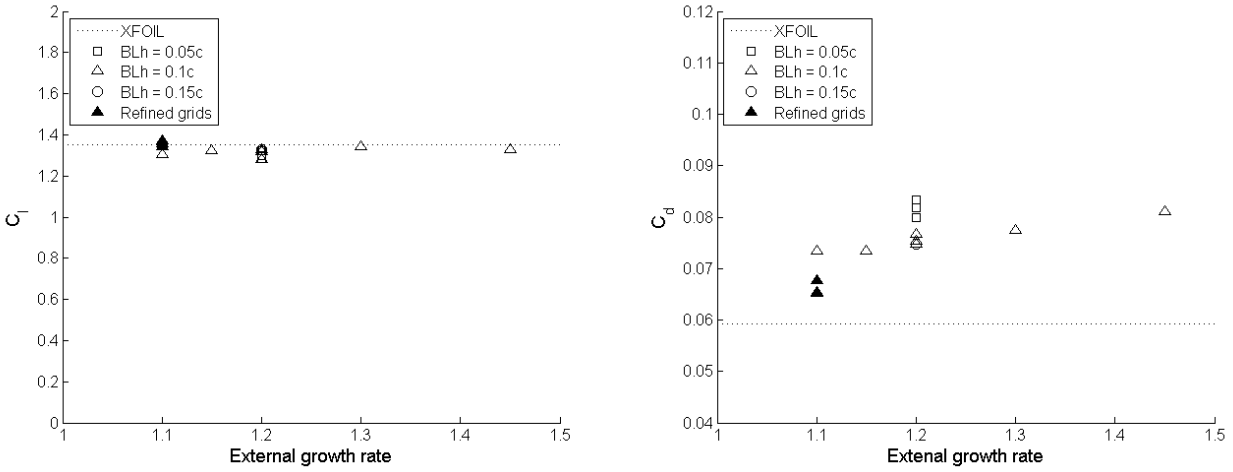

Figure 5.13: Numerical simulation results with varying geometrical growth rates in the external domain. The extended use of size functions makes the 'refined grids' better than the ones tested here. However, the number of cells i one third in the new cases.

5.4 Reynolds number effects

It is seen from figure 5.2, that the airfoil characteristics depend both on the transition criteria as well as the Reynolds number. For a fully turbulent flow around an airfoil at a moderate angle of attack, an increase in Reynolds number dictates an increase in airfoil performance.

The Reynolds number of the wind turbine blade will be determined by the tip speed for high tip speed ratios. With a free stream velocity of 10 m/s, a tip speed ratio of 12 will give a Reynolds number at the tip close to $2.0 \cdot 10^5$. A tip speed ratio of 1 will give a Reynolds number almost 10 times lower. This is bound to give high variations in lift and drag for the same angle of attack.

It is seen from figure 5.14 that there are large differences in airfoil forces depending on the Reynolds number. Because of this, the BEM program should have the ability of using lift and drag data for several Reynolds numbers. As the program code is not taking this into account, it is expected that certain errors will arise.

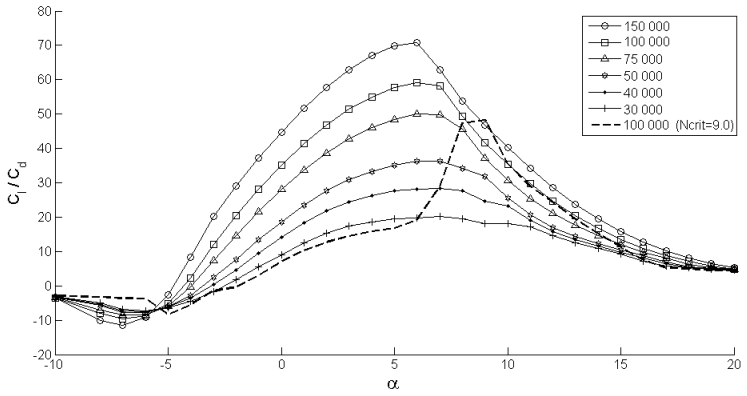

Figure 5.14: An examination of the Reynolds number effect on the lift drag ratio. The results have been computed in XFOIL with $Ncrit = 3.0$. One calculation with $Ncrit = 9.0$ and has been included for comparison.

One sees that the $Ncrit = 9.0$ regime at high Reynolds numbers gives quite similar results than the $Ncrit = 3.0$ regime when the Reynolds number is low. This is because laminar separation bubbles exist in both cases. Because the transition process depends on the Reynolds number, one gets similar results for some cases. This way, the $Ncrit = 9.0$ regime can give some indications on what happens if the Reynolds number is reduced, whiteout actually taking the Reynolds number into account.

An examination of the SST turbulence model ability to predict changes in airfoil forces at different Reynolds numbers was tested. This was done using grid 'O I', keeping the angle of attack at 0° and 7°. The results showed that the SST–model was capable of calculating the lift and drag coefficients in the range of local Reynolds numbers expected over the wind turbine blade.

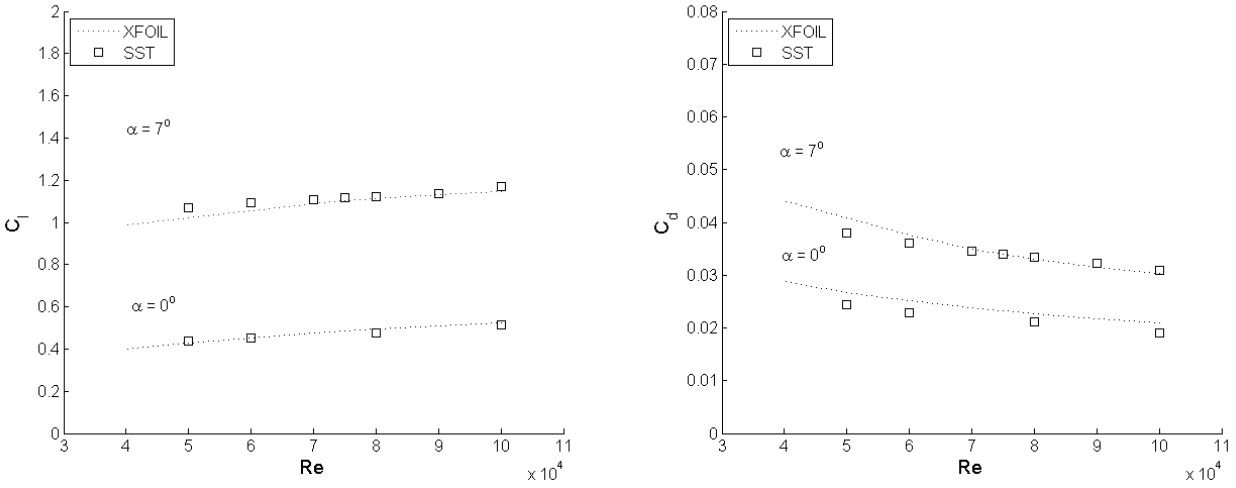

Figure 5.15: Lift and drag sensitivity to varying Reynolds number at two angles of attack.

5.5 Recommendations for 3D simulations

Based on the experience gained from the 2D–simulations, a rough estimate for some of the simulation parameters in the 3D case can be determined.

For the three dimensional grid, the following guidelines should be followed:

- 200 or more grid–points around the airfoil in the chordwise direction
- Increased chordwise refinement close to the leading and trailing edge
- A maximum value of y_p^+ no more than 5, and an average value no more than 1.
- At least 15 cells in the structured boundary layer grid
- A thickness of the structured boundary layer grid no less than $0.1C$
- The geometrical growth rate outside the boundary layer grid should be as low as possible

In addition, the k–ω SST–model should be used in its fully turbulent form.

Chapter 6

Construction of 3D model

6.1 3D model

A 3D model of the wind turbine blades was obtained from the company that machined the blades. This way it was assured that the model used in the numerical simulations was the exact same as the one used for the production of the blades. The uncertainty in the 3D model is then only related to the error in the production process, which can be assumed to be small.

The hub was measured manually and added to the model of the 3D blades. The uncertainties introduced in this process can be expected to be somewhat larger than in the modelling of the blades. However, the hub is not a vital part of the model, and small uncertainties can be accepted here.

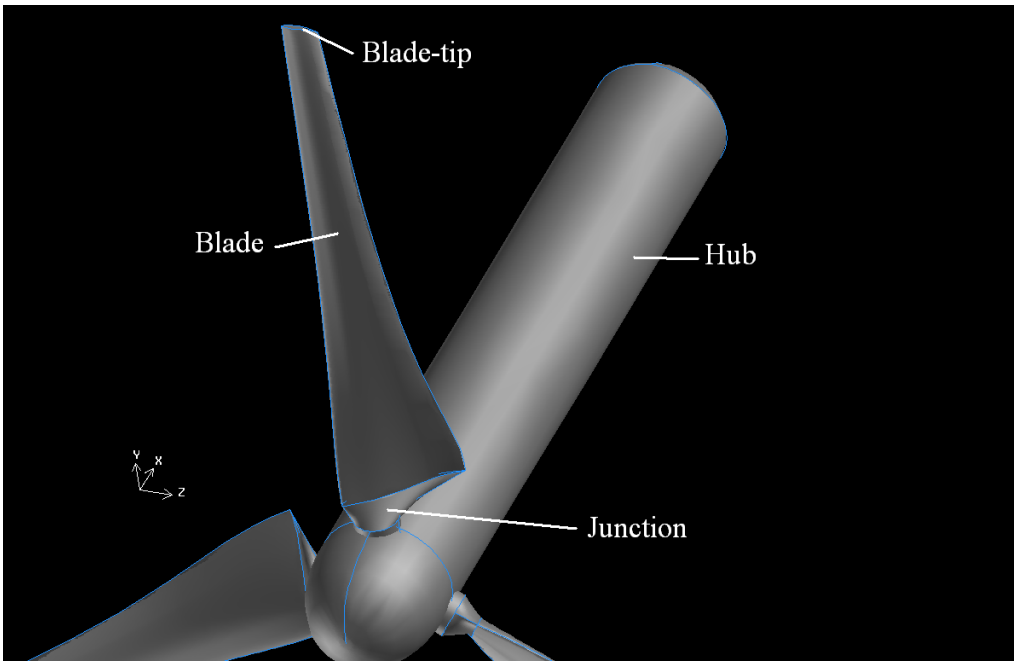

Figure 6.1: A 3D model of the wind turbine blades and hub. The different parts of the model are denoted

As long as the tower influence is excluded from the model, and the wind tunnel modelled as a circular

tube, the flow field around the wind turbine can be assumed to be be rotationally periodic. This makes it possible to model only one third of the complete model, as the flow in the other two thirds will be fully described by the flow in the first. This reduces the needed number of cells to one–third, making it more easy to reduce the number of cells needed.

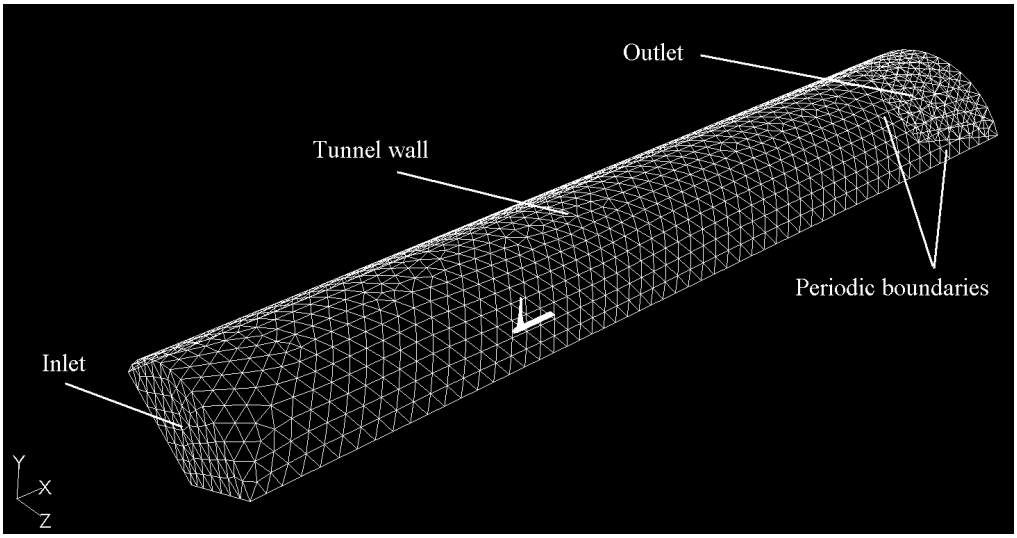

Figure 6.2: The numerical domain. The wind tunnel is modelled as one third of a cylinder. The periodic boundary surface grid has been excluded from the wiev. The wind tunnel blade and hub can be seen in white inside the model.

The wind tunnel was modelled as a cylinder with a cross section equal to that of the real wind tunnel. The cross section of the wind tunnel is 2.7 m $\cdot$ 1.9 m, making the corresponding radius 1.278 m. This approximation is done in order to reduce the need for sliding meshes. The procedure has been used in other studies, and has been reported not to introduce significant errors [21].

No mesh indepency test was made, as this is very expensive in 3D. But based on the two–dimensional studies, good choices of grid parameters is expected to reduce numerical errors to a minimum.

6.2 Surface mesh

6.2.1 Blade

The surface mesh was created using GAMBIT. The blade needs a high degree of refinement. Because of this a structured mesh was chosen in order to reduce the amount of cells needed to get a fine resolution near the leading and trailing edge. A total of 300 nodes was used around the airfoil in the chordwise direction, and 200 nodes in the spanwise direction. Close to the root and the tip, the spanwise extension of the cells was kept at 0.1 mm. Near the leading and trailing edge, the chordwise extension of the cells was kept at 0.03 mm close to the tip, and 0.1 mm close to the root.

In total, 60 000 faces was used to describe the surface of the blade.

6.2.2 Tip

An unstructured mesh was used to represent the tip of the wing. The elements had a size corresponding to the streamwise extension of the cells close to the tip on the blade surface, but was allowed to grow somewhat toward the center of the tip surface.

A total of 3056 faces was used to describe the tip of the blade.

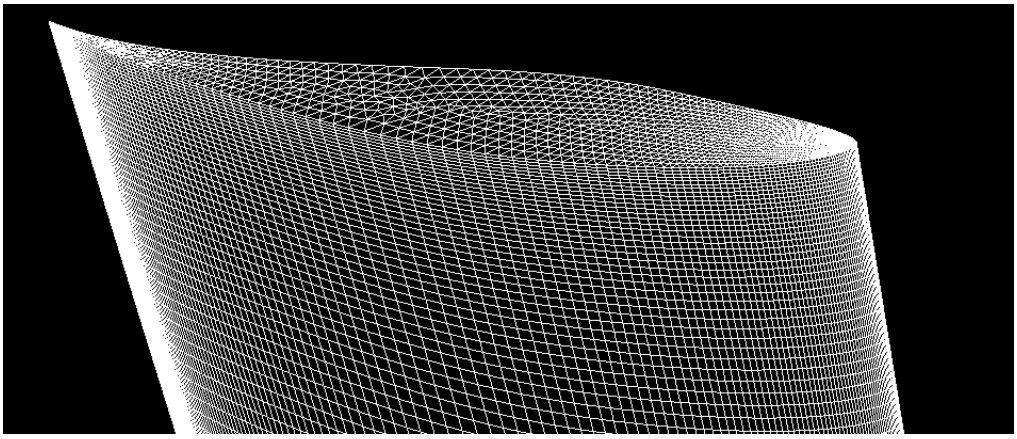

Figure 6.3: Detail of grid at the tip of the turbine blade.

6.2.3 Junction

The junction between the blade and the hub consists of two parts. A cylindrical section close to the hub, and a transition from this cylinder to the blade. Due to the three dimensional curvature of the latter section, an unstructured mesh was chosen. The size of the element edges was kept below 1 mm in the transition part of the blade, and below 0.5 mm on the tubular section.

A total number of 28 500 faces was used to describe this part of the blade.

6.2.4 Hub

The hub is formed as a cylinder with a rounded front and rear. An unstructured grid was used here as well. The size of the face edges was set to a maximum of 7 mm on the hub surface, with a refinement in the front, near the blade junction and close to the rear of the hub.

A total number of 7500 faces was used to describe the hub.

6.2.5 Exterior surfaces

There was five exterior surfaces in the model. Two periodic boundaries, one inlet, one outlet and one surface describing the wind tunnel roof. These surfaces was all meshed using triangular faces. Far from the wind turbine, the cell edges was set to a length of 0.2 m, and size functions was used to enhance refinement close to the wind turbine.

The mesh on the three latter surfaces can be seen in figure 6.2. The periodic boundary mesh was created using a size function with a geometric growth rate of 1.2, that allowed the mesh to grow from

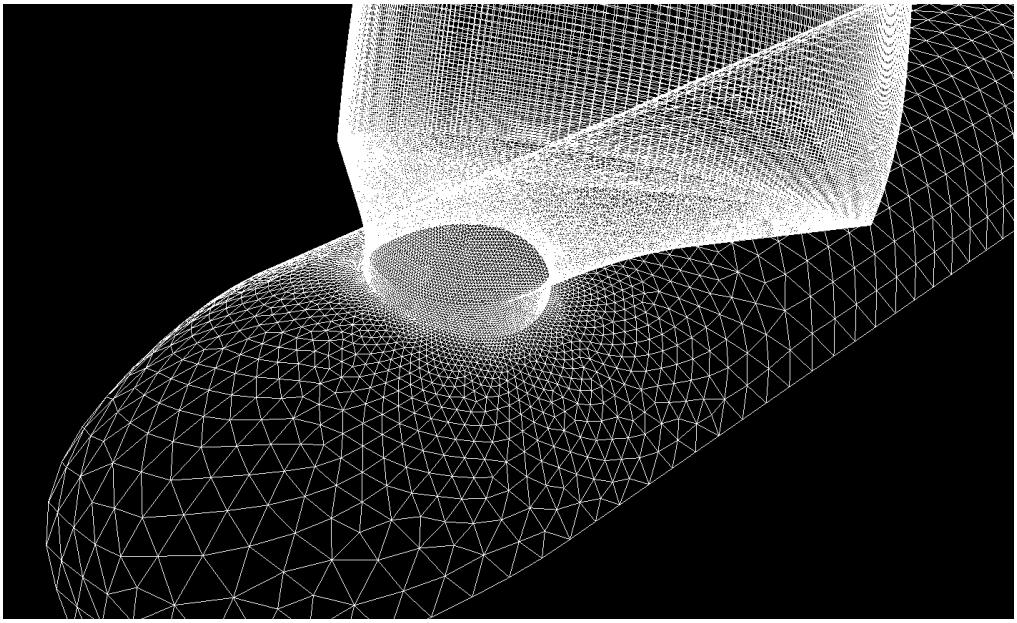

Figure 6.4: Detail of the grid close to the hub. Size functions was used to refine the grid close to the junction and near the front and rear of the hub.

the sizes related to the hub, to the sizes related to the rest of the exterior surface meshes. A figure of the periodic boundary grid can be found in appendix A.6.

6.3 Boundary layer grid

Using the program TGRID, a boundary layer grid was created on all the physical surfaces. Prism layers were grown from all wall surfaces (blade, tip, junction, hub). A layer of pyramid cells was attached to the surface of the structured cell faces on the boundary layer grid. This was done in order to be able to use an unstructured volume grid in the rest of the domain.

The viscous shear on the wind turbine surface is expected to be more or less the same in the 3D case as in the 2D simulations, as long as the local Reynolds number is the same. The shear could be influenced by three–dimensional effects, but these are expected to occur at low tip speed ratios where the blade Reynolds number is allready low. The 2D simulations showed that as long as $y_p < 5 \cdot 10^{-4} C$, the corresponding value of y_p^+ was low enough to resolve the viscous boundary layer in a decent way. Based on the tip chord length of 26 mm, the grid point closest to the blade surface should be approximately 0.01 mm from the wall. Closer to the hub, the local Reynolds number is expected to decrease (as seen in figure 7.1), a fact that indicates that the choice of y_p should be based on the tip conditions.

The boundary layer thickness should be kept higher than $0.1C$. Based on the maximum chord–length, the boundary layer grid thickness should be approximately 9 mm.

23 cells were created in the boundary layer grid, with a geometric growth rate of 1.2, yielding a boundary layer grid height of 3.3 mm. The program was incapable of creating a higher grid, because of the proximity of the faces, and the concave curvature of the blade pressure side. This resulted in a boundary layer height less than one third the recommended value, a possible cause of numerical stability problems in cases where the root of the blade is stalled.

A total number of $1.98 \cdot 10^6$ cells were created in the boundary layer grid.

6.4 Volume grid

In order to get a smooth transition between the quadrilateral faces in the boundary layer grid above the blade, pyramid cells were used to get triangular interfaces. In total 60 000 pyramid cells were added to the boundary layer grid. The pyramid interface is only a moderately good choice in interfaces where the quadrilateral cells have a high aspect ratio. Close to the leading and trailing edge, high aspect ratios occur near the center of the blade. The resulting mesh will therefore have certain spots of low quality in the interface between the structured hexahedral boundary layer cells and the unstructured tetrahedral volume cells.

This is clearly seen from figure 6.5, where the 'spider web' structure indicates cells of high aspect ratio and large size changes. This could increase the truncation error. A further discussion of the errors introduced in the simulations is conducted in chapter 7.2.2.

A geometric growth rate was used to increase the cell size with the distance from the wind turbine blade. A growth rate of 1.45 had to be used in order to get the cell number below 4 millions. The cell sides were set to grow geometrically until the cell edges reached a size of 0.2 m.

This resulted in a total number of $3.54 \cdot 10^6$ cells.

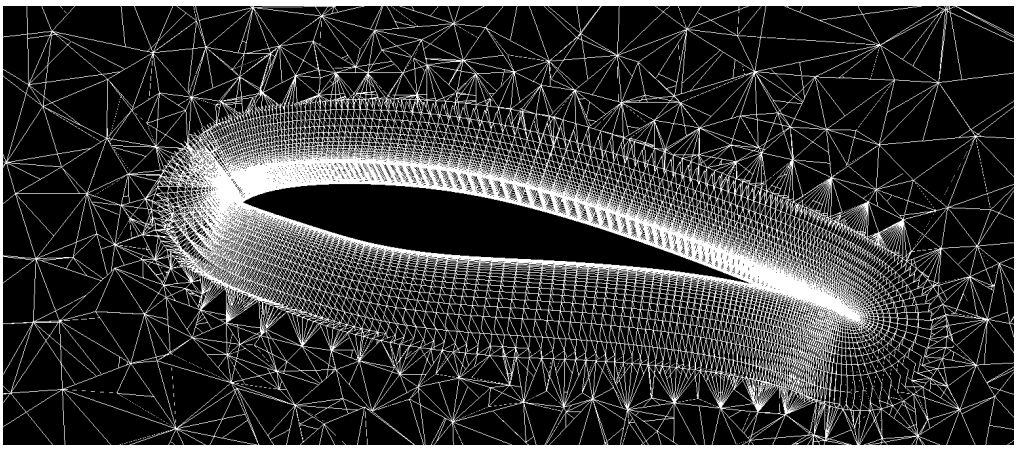

Figure 6.5: A cut at a radial position of $y = 0.4$ m. The interface between the structured boundary layer grid and the unstructured tetrahedral cells is clearly seen.

Griding in three dimensions is a time consuming activity. It is evident that an equal or even better accuracy could be obtained using fewer cells. However, problems with the griding programs and lack of time did put certain restrictions on the grid quality.

Certain errors are expected in the 3D simulations, but the grid is assumbed to be good enough to capture the flow physics.

Chapter 7

Results and discussion

7.1 BEM results

7.1.1 BEM calculation procedure

A Blade Element Momentum computation of the wind turbine performance was made. This was done using the PERFORMANCE code that is described in figure 3.7. The blade geometry was obtained from the 3D CAD model, that was the basis of both the production of the wind turbine blades, and the CFD model. However, in order to make the format acceptable for the BEM code, some minor changes had to be made to the blade junction. The description of the blade geometry can be found in appendix A.3. Lift and drag curves obtained in the two–dimensional study was used in the calculations.

For high tip speed ratios the BEM code had convergence problems for certain blade elements close to the root of the blade. This seems to occur in cases where the wind turbine acts as a propeller, adding energy to the wind. In these cases the axial induction factor and the blade section moment will become negative.

7.1.2 Blade section Reynolds number

The program code can only apply one lift and drag curves at the time. Because of this, a fixed Reynolds number is used in the calculations. This is inaccurate, as the Reynolds number is known to vary with the rotational speed of the wind turbine. An initial study was therefore conducted, in order to calculate blade Reynolds number and angle of attack for different tip speed ratios. The $Ncrit = 3.0$ results with a fixed Reynolds number of $1.0 \cdot 10^5$ was used in the calculations. The axial and angular induction factors were then found, making it possible to determine the local flow angle (φ). This was used to determine the angle of attack, using equation 3.15 and the following relation:

$$\alpha = \varphi - \theta \tag{7.1}$$

The Reynolds number was found using the relative velocity (U_{rel}) and the local chord length (C)[1]. The relative velocity was derived from the induction factors, using equation 3.14. The results are

[1]The local Reynolds number was calculated using a kinematic viscosity of $1.46 \cdot 10^{-}5\ \mathrm{m}^2/\mathrm{s}$

presented in figure 7.1, and form a basis of the following discussion, where local angles of attack and Reynolds numbers are important parameters.

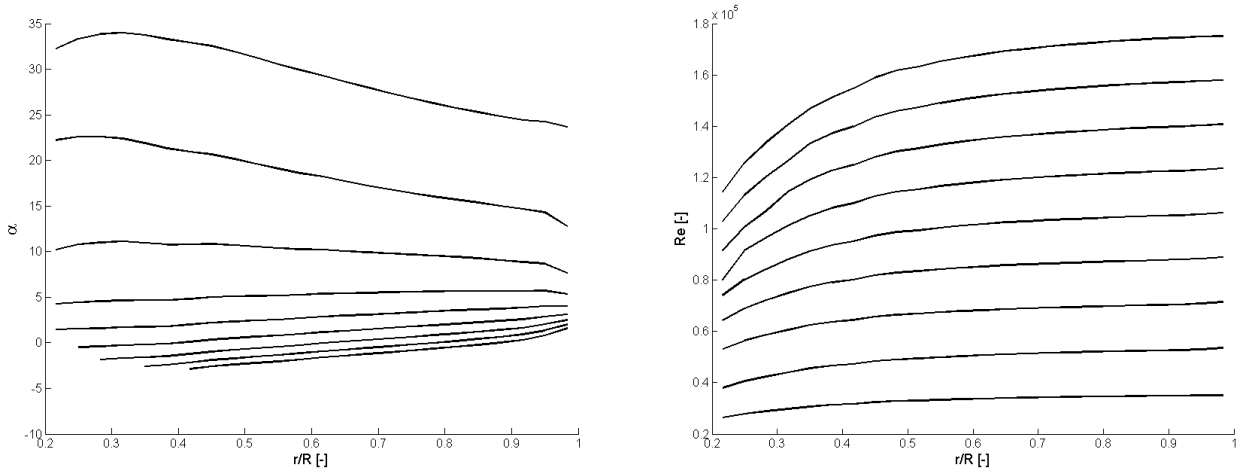

Figure 7.1: Variations of Re and α over the blade, for $\lambda = 2, 3, 4, 5, 6, 7, 8, 9$, and 10. $Ncrit = 3.0$. The angle of attack is gradually reduced, and the Reynolds number increased with increasing tip speed ratios.

The Reynolds number is found to vary from approximately $3.0 \cdot 10^4$ to a maximum value of almost $2.0 \cdot 10^5$. From the findings in chapter 5.4, it is clear that this will affect the lift and drag coefficients of the airfoil. The lift and drag curves used in the further study have been calculated at a Reynolds number of $1.0 \cdot 10^5$. This has been chosen as it is representative for the design conditions of the wind turbine ($5 < \lambda < 7$). In order to get a more accurate result from the BEM calculations, lift and drag curves for different Reynolds number should have been applied. But, as the program is not designed for that, this will not be taken into account.

The Reynolds number study in chapter 5.4 indicated that the angle where stall occurred did not change much with the Reynolds numbers. This means that these results could give good indications of when the wind turbine blade will stall. The results presented in figure 7.1 indicate that the blade will be fully stalled for tip speed ratios below 4, whereas it will be partly stalled at a tip speed ratio of 4. Increasing the tip speed ratio above 5, the the boundary layer on the wind turbine can be expected to remain attached for tip speed ratios up to 10. However, some separation will probably occur on the separation trap near the trailing edge. For high tip speed ratios, the angle of attack is reduced towards $-5°$. However, it is hard to say whether or not the root of the blade is stalled for high tip speed ratios, as the BEM code gave no solutions for these conditions.

7.1.3 C_P and C_T calculations

Power curve predictions

Using the BEM method, C_P and C_T curves was calculated for tip speed ratios ranging from $\lambda = 1$ to $\lambda = 25$. Some convergence problems did occur for blade elements close to the hub for high tip speed ratios, but the effect is small for all tip speed ratios below 9 [2]. The results from the calculations are presented in figure 7.2

[2] A more detailed study of the blade forces is found in chapter 7.3

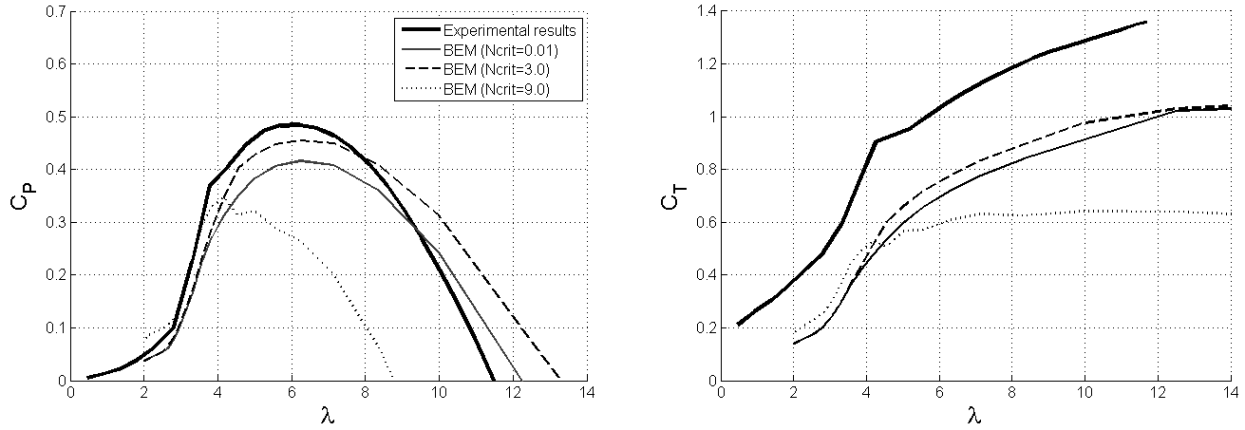

Figure 7.2: C_P and C_T curves from the BEM calculation compared to experimental measurements. The lift and drag curves used in the calculations are obtained in the two dimensional study, and can be found in figure 5.3.

The three different transition criteria examined in chapter 5.2 were used, yielding quite different results. However, no transition criteria seems superior in describing the flow field. The $Ncrit = 9.0$ regime tends to predict the C_P curve very well for low tip speed ratios, where the angle of attack is relatively high. This is expected as the laminar separation was found to improve the airfoil performance for moderately high angles of attack. But when the tip speed ratio is increased to $\lambda = 4$, and the the angle of attack is reduced, the laminar separation bubbles deforms the airfoil, reducing the efficiency. This is visible as a sharp drop in the C_P curve at $\lambda = 4$ for the $Ncrit = 9.0$ case.

For $\lambda > 4$ the $Ncrit = 9.0$ regime fails in predicting the wind turbine production. This indicates that the laminar flow effects that were found in the two dimensional study, are not present in the experiment for the Reynolds number in question. However, for a lower wind tunnel Reynolds numbers laminar effects could occur. These effects will probably be seen as a reduction in wind turbine efficiency for moderate angles of attack, probably occurring for tip speed ratios larger than 4.

The laminar effects can be seen in figure 7.3, where data from a Reynolds number study performed by post doc. Muyiwa Adaramola on the same wind turbine is presented. It is clear that as the Reynolds number is reduced, laminar separation occurs. The blades are not affected by this in the stalled area, but as the boundary layer attaches, the laminar separation influences the airfoil performance, reducing the efficiency of the wind turbine. However, as the tip speed ratio increases, the C_P curve is found to be increasing again. This is because the local blade Reynolds number increases, moving the point of transition closer to the leading edge, surpressing the laminar separation. For high tip speed ratios the flow over the blade seems to be little affected by Reynolds number. This is because the increase of Reynolds number due to faster rotation, is far larger than the reduction due to the reduced free stream velocity in the experiments.

As the blade Reynolds number has been calculated to be close to $1.0 \cdot 10^5$ for $\lambda = 6$, the lift drag curves obtained should be correct at this point. In addition, the BEM method is expected to give good results in this area, as it is close to the design tip speed ratio. Because of this, the results gives a clear indication that the $Ncrit = 9.0$ is too conservative for the conditions in the wind tunnel. As discussed in chapter 5.2, this could be related to rotating effects, free stream turbulence or roughness, causing transition to occur before the boundary layer separates.

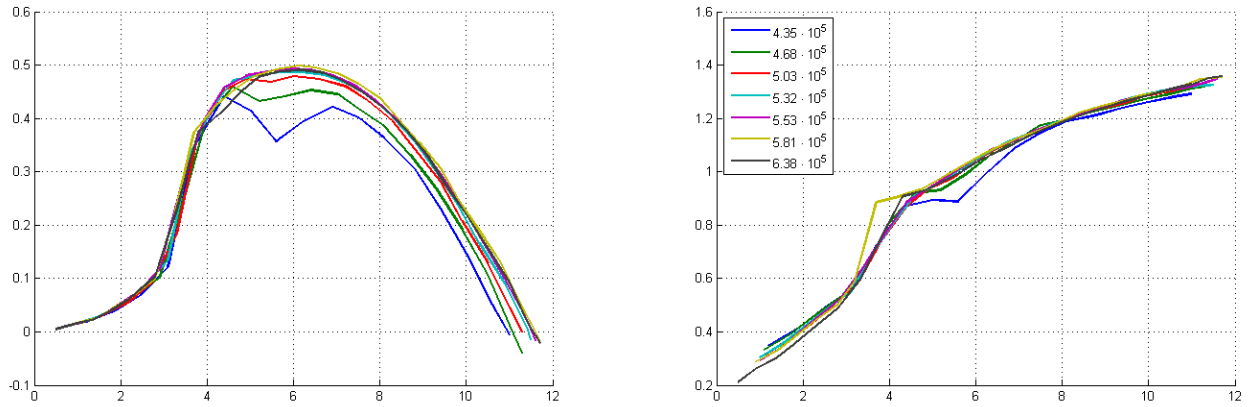

Figure 7.3: Experimental data from a wind turbine Reynolds number study. The Reynolds number is based on the wind tunnel free stream velocity and the wind turbine diameter. The experimental data from this study is included. The rest of the data have been reproduced with courtesy of Muyiwa Adaramola [1].

The BEM method seems to be able to predict the point of stall fairly well. There is a good correlation between the dynamic stall effects observed in the experiment and the prediction of stall in the BEM method.

It is interesting to notice that the $Ncrit = 9.0$ regime predicts laminar stall at the same tip speed ratios as the dynamic stall effects were observed. Laminar stall can occur very abruptly, and this could be one explanation of the dynamic effects observed in the experiment. However, the dynamic stall could also be related to regular turbulent stall. If the dynamic effects are related to laminar stall, the onset of the stall is expected to be very sensitive to the Reynolds number or free stream turbulence level. This could be examined by simple experiments in the wind tunnel.

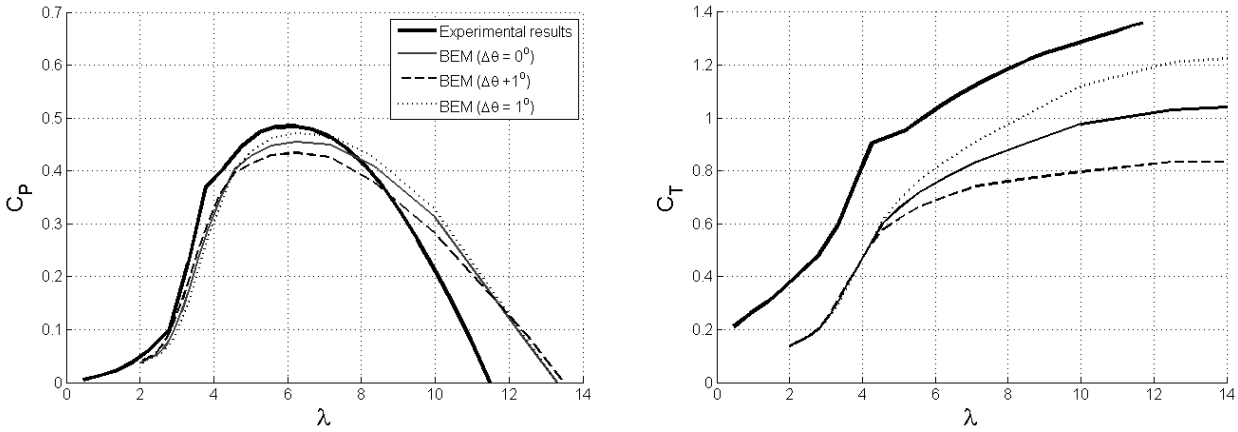

Figure 7.4: BEM calculations with the $Ncrit = 3.0$ transition criteria and an offset angle $\Delta\theta$.

For moderate and low tip speed ratios, the BEM method tends to underpredict the wind turbine efficiency, whereas the efficiency is overpredicted for high tip speed ratios.

As the $Ncrit = 3.0$ regime tends to give the best results for the wind turbine performance, this will be used in the further studies.

Thrust curve calculations

While the predictions of the power coefficient were rather accurate, there are larger deviances in the thrust coefficient predictions. However, the difference seems to be rather constant. It is also clear that Glauerts correction factor succeeds in predicting thrust in the invalid area ($a >> 0.2$).

However, the constant underprediction of the thrust force needs to be commented upon. One possible source of uncertainty is the blade pitch angle. It was possible to pitch the blade in the experimental setup. If the blades were misaligned, they could add bias to the results. This was tested by introducing an offset angle in the BEM calculations. An offset angle of 1° was chosen, as the uncertainties in the experimental pitch alignment are expected to be below this value.

As indicated in figure 7.4, even a small offset angle can cause large changes in the C_T curve for high tip speed ratios. However, for $\lambda = 5$ the differences are small. Because of this the thrust coefficients should be compared at the design tip speed ratio. Here the Reynolds number is correct, two dimensional effects are assumed to be small, and an errenous offset angle in the experiment will have little impact on the results.

The underprediction of the thrust force seems to be in the order of $\Delta C_T \approx 0.3$, where $\Delta C_T = C_{T,exp} - C_{T,bem}$.

The experimental thrust coefficient includes the thrust (drag) caused by the tower, hub and transmission belt behind the wind turbine. It is probable that the tower thrust is dominant compared to the other sources of drag. It is then possible to determine a tower thrust coefficient that contain the additional drag. If this coefficient is in the order of what is expected for a circular cylinder, the rotor thrust coefficient can be assumed to be correct. If the tower thrust coefficient is too large, then the BEM thrust calculations are probably too low. If one assumes that the disk thrust is correctly predicted by the BEM method, the tower thrust will be given by:

$$T_{exp} = T_{bem} + T_{tower}$$

$$C_{T,exp} - C_{T,bem} = \frac{T_{tower}}{\frac{1}{2}\rho U_\infty A_{rotor}}$$

$$\Delta C_T = C_{T,tower}\frac{A_{tower}}{A_{rotor}} \tag{7.2}$$

The total thrust coefficient and the rotor thrust coefficient are both based on the rotor area. We know that the frontal area of the tower is approximately 0.052 m^2. Introducing the known ΔC_T into equation 7.2, we get $C_{Ttower} \approx 3.7$. This is far higher than what can be expected from the cylindrical tower only. A circular cylinder can be expected to have a drag coefficient no higher than 1.2 in the range of Reynolds numbers expected here [27]. The other sources of thrust are not expected to be larger than twice the thrust of the tower. This is an indication that the BEM method underpredicts the thrust force.

7.2 CFD results

7.2.1 CFD solution strategy

The Navier–Stokes solver, FLUENT, was used for the CFD simulations. FLUENT uses a finite volume method, and steady–state calculations of the RANS equations was performed. The flow regime was assumed to be incompressible, as the velocity in the study was below Mach 0.3 for all tip speed ratios except the $\lambda = 11$ case. In this case the tip speed do actually reach 110 m/s, but this is an exception, not representative for the majority of the cases studied. Compressibility effects were therefore excluded from this study.

The SIMPLEC algorithm was used to couple the pressure and velocity fields. The computations were run on a 64–bit computer with four processors, making parallel processing possible. The turbulent eddy viscosity was modeled using the k–ω SST–model. The momentum equations were solved using a quadratic discretisation scheme (QUICK) for the convective terms, while the pressure was discretised using a normal 1. order discretisation scheme. This was done to enhance convergence, as higher order schemes of pressure discretisation showed to be unstable. Under–relaxation factors was tuned during the iteration process, in order to achieve a converged solution.

A total number of 5000 iterations showed to be sufficient for most calculations, taking approximately 24h to complete.

The viscosity was set to $1.7894 \cdot 10^{-5}$ kg/m $\cdot$ s, and the density to 1.225 kg/m^3. The inlet velocity was set to 10 m/s, which gave a Reynolds number based on the wind turbine diameter of $6.16 \cdot 10^5$. This was done before the experiments was performed, resulting in a Reynolds number approximately 3.4% lower than in the experiments. As seen in figure 7.3 this is not expected to have any significant effect on the solution. However, if transition effects were to be modelled, the flow regime would be more sensitive to Reynolds number effects.

At the inlet a turbulence intensity and a turbulent viscosity ratio was determined. The turbulence intensity is described in equation 3.49, and was set to 1.5% at the inlet. A turbulent viscosity ratio of 10 was set at the inlet, in order to keep $\epsilon \approx 2k$. This gave a turbulence intensity of approximately 0.5% at the wind turbine position in an empty wind tunnel.

7.2.2 Error analysis

According to the AIAA guidelines for verification and validation of CFD analysis, error is defined as: *"A recognizable deficiency in any phase or activity of modeling and simulation that is not due to lack of knowledge"*. An uncertainty is defined as: *"A potential deficiency in any phase or activity of the modeling process that is due to the lack of knowledge"* [2]. There are several sources of errors and uncertainties in this analysis. Some of the uncertainties are allready commented upon. In this section the errors in the CFD analysis will be addressed.

Physical approximation errors

There are several physical approximation errors in the model. The most important ones are the assumptions of the flow regime as stationary, turbulent and rotationally periodic. The assumption of rotational periodicity means that the tower had to be excluded from the model, and that the wind tunnel had to be modeled as a circular cylinder.

The assumption of a stationary flow regime excludes all dynamic effects. As severe dynamic effects were observed in the experiments, this omission do affect the results to a large extent. The assumption of a fully turbulent regime do exclude all laminar effects. As indicated in chapter 7.1.3, laminar effects could be important in prediction of the dynamic stall occurring at moderate and low tip speed ratios. However, for other tip speed ratios examined, laminar effects are expected to play a less important role.

The boundary layer close to the wind tunnel wall was removed in order to reduce the demand for cells. Consequently, the wind tunnel walls were modeled using a no–shear condition.

Computer round off errors

In order to reduce the computer round off errors, the 'double precision solver' was used in all simulations. Because of this, computer round off errors can be assumed to be very small compared to other errors in the model.

Iterative convergence error

The iterating process was run until no significant drop in residual was observed. For some tip speed ratios there were still some variations or oscillations in the solution at this point. This is denoted iterative convergence error. In order to reduce this error, the moment and thrust force was observed. For cases where the variations in these forces were less than 1%, a converged solution was assumed. An illustration of iterative convergence errors can be seen as small oscillations in the C_m and C_d curves in appendix A.8.

Discretization error

No grid dependence test was made in the three dimensional case, as this is very time consuming. Based on the two dimensional analyses made in chapter 5.3, the constructed grid was assumed to be good enough for the simulations. However, the discussion in chapter 6.4 revealed that the constructed grid has certain shortcomings. Especially in the interface between the structured hexahedral boundary layer cells and the tetrahedral cells in the rest of the numerical domain. In addition, the height of the structured boundary layer grid close to the root of the blade was much lower than what was recommended in the 2D simulations. The low grid quality in these parts of the domain could lead to rather large truncation errors for certain cases.

The discretization errors are reduced to some extent by introducing the QUICK discretization scheme.

For tip speed ratios 9 and 11, completely converged solutions were hard to achieve. In order to get stable solutions, the discretisation had to be reduced to a 1. order upwind scheme. The instability observed could be caused by inherent instabilities in the flow, e.g vortex shedding from the blade. It is also plausible that the instability of the solution is connected to the reduced grid refinement close to the root of the blade. A better grid might improve the results. The values of y_p^+ was not found to exceed the recomended values, as illustrated by figures in appendix A.7.

It is expected that the physical approximation errors and the discretisation errors will be the dominant sources of errors in the simulations.

7.2.3 C_P and C_T calculations

From figure 7.5 it is evident that the C_P curve is reproduced by the CFD simulations. The differences between measured and simulated power coefficients were lower than 5% for tip speed ratios up to 6. The differences were somewhat larger for higher tip speed ratios. This could be related to truncation errors introduced by reduction of the discretisation scheme.

For low tip speed ratios there is a very good agreement between the experimental results and the simulations. The dynamic stall effects found in the experiment were not observed. Stationary solutions for $\lambda = 4$ and 5 were obtained, and they tended to be quite stable. This is an indication that they are related to laminar effects as the dynamic stall was not captured in these fully turbulent simulations.

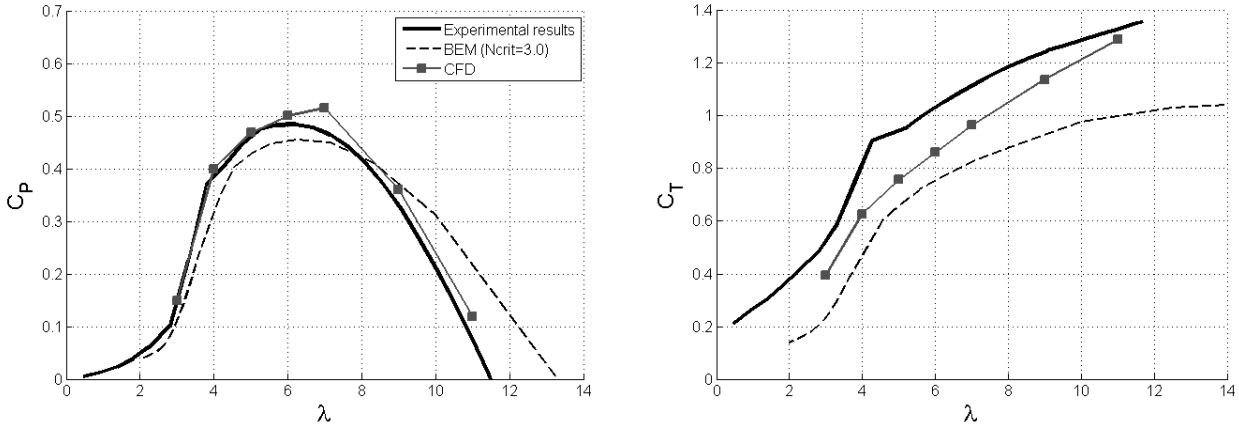

Figure 7.5: C_P and C_T curves from the CFD simulation compared to experimental measurements. The $Ncrit = 3.0$ BEM calculation has been included.

For the CFD simulations, the mean difference between the measured and simulated thrust coefficient is approximately $\Delta C_T \approx 0.13$. Using equation 7.2, this corresponds to a tower thrust coefficient $C_{Ttower} \approx 1.6$. This is somewhat larger than expected for an infinite cylinder immersed in laminar flow [27].

It is hard to say whether the flow around the tower will be laminar or turbulent. The Reynolds number based on the diameter of the tower and a free stream velocity of 10 m/s is varying between $3 \cdot 10^5$ and $7 \cdot 10^5$, depending on the tower diameter. This is in the range of Reynolds numbers where transition is known to occur (see figure A.8 in the appendix [27]). However, as the cylinder has a non–uniform diameter, it will probably have a drag relationship like a cylinder of finite span. Thus the drag coefficient of the tower alone should be lower than 1.2.

The blocking effect caused by the rotor will also influence the tower drag coefficient, as it is scaled by the free stream velocity. This could lead to a reduction in ΔC_T in cases where the blocking effect is more dominant. This is not found in the experiments, as ΔC_T is seen to be high for moderate tip speed ratios. For these conditions the blocking is expected to be quite uniform and high, as much energy is extracted from the free stream. As one sees from figure 7.6, the blocking effect causes a wind speed reduction up to 30% at the tower position when $\lambda = 6$.

It must also be noted that the presence of the tower will induce an upstream blocking effect, reducing the free stream velocity in the rotor plane. This will also affect the measured thrust force.

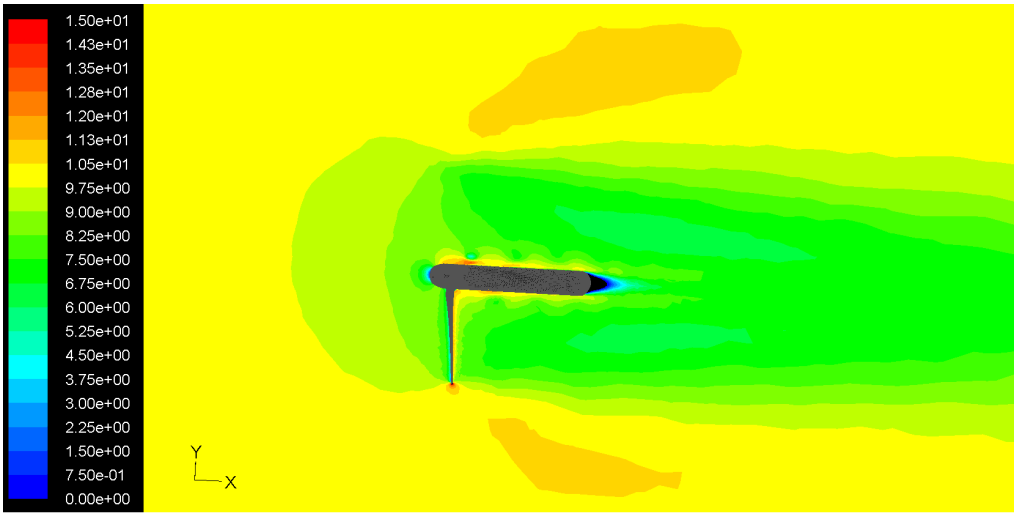

Figure 7.6: Contour plot of the axial speed distribution in a plane z=0 at $\lambda = 6$. One wind turbine blade has been excluded from the view.

In total, the thrust deficit found in the CFD simulations can be said to be within the expected range. The influence of the thrust forces will increase the tower drag coefficient. And as the power curve is well described using the CFD method, it can be expected that the actual thrust forces acting on the rotor and hub are fairly well described as well.

Experimental testing of the tower drag could have been performed by removing the blades from the turbine. This has not been done.

The CFD calculations have given a good estimate of both the thrust and power prediction of the wind turbine. There is a good match between the experimental results and the simulations. The BEM method did give reasonable results for the power curve, but the thrust forces tended to be underpredicted. This underprediction is not caused by the hub drag. This drag is not included in the BEM calculations, but according to CFD results for $\lambda = 4$, less than 2% of the the drag on the modelled geometry is caused by forces acting on the the hub. It is therefore clear that the BEM method underpredicts the thrust forces.

7.3 Blade forces

7.3.1 Methods

When comparing C_P and C_T curves, only the gross forces acting on the blade are examined. A good representation of the power or thrust coefficient is therefore no proof that the spanwise force distribution is well described. Because of this a more detailed study of the forces acting on the different blade sections was conducted. The forces acting on each blade element was extracted by the BEM code. The spanwise force distribution was found using equation 3.22 and 3.23. The computations were made for five different tip speed ratios. In order to reduce the inaccuracies, lift and drag curves for the corresponding Reynolds number were used. For $\lambda = 3$ and 4 a Reynolds number of 40 000 was used. For $\lambda = 6$ a Reynold number of 100 000 was used, while a Reynolds number of 150 000 was used for $\lambda = 9$ and 11.

Data from the CFD simulations was extracted from FLUENT by creating 60 iso–surfaces with different radial distances from the centerline. From all blade cell faces intersected by one of these iso–surfaces, the total pressure and viscous wall shear stress vector at the cell center was extracted. In addition the cell face normal vector and area of each cell was computed. These data was used to extract both axial (thrust) and tangential (moment) forces acting on the different sections of the blade. The forces are denoted dF_x and dF_z and are given in [N/m]. They were determined by adding all viscous and pressure forces acting on the wall cell faces in one radial section of the wind turbine blade:

$$dF_x = \frac{C}{A_{tot}} \sum_{j=0}^{j=N} p_j (A_x)_j + (\tau_{w,x})_j A_j \tag{7.3}$$

$$dF_z = \frac{C}{A_{tot}} \sum_{j=0}^{j=N} p_j (A_z)_j + (\tau_{w,z})_j A_j \tag{7.4}$$

$(A_i)_j$ is the total area of cell face j multiplied by the cell face normal vector component in direction x_i. There are N cells in one radial section. p_j and $(\tau_i)_j$ are the total pressure in cell j and the viscous wall shear acting on the same cell in the x_i direction. All cells in one radial section do have the same height (or spanwise extension). Therefore this simplified method is applicable.

A_{tot} is the sum of the area of all cell faces in one radial section, and C is the local chordlength. By dividing the sum by the 'height' of the radial section (A_{tot}/C), the forces are made independent of the cell faces area.

Integrated along the blade we get the total thrust force in the axial direction, T, and the total moment in the tangential direction, M.

$$T = \int_0^R dF_x dr$$

$$M = \int_0^R dF_z r dr$$

7.3.2 Results

From figure 7.7, one sees how the blade element method manages to predict tangential forces for $\lambda \geq 6$ fairly well. Both the magnitude and spanwise variations are captured. The fact that the spanwise variations near the tip are well–described, indicates that Prandtls tip loss succeeds in quantifying the loss of circulation at the tip of the blade.

For $\lambda = 4$, the tip effect is not properly described. The reductions in blade forces start too early and are decreasing too slow compared to the CFD results.

Looking at the blade thrust forces, the tip effect is well described for $\lambda \leq 6$. However, for $\lambda = 9$ and 11 the rate of which the axial induction factor is increasing toward one, as one approaches the tip of the blade, is too low to capture the tip effect.

It is clear that the thrust force is systematically underpredicted by BEM method. The results was somewhat improved by using the correct Reynolds number in the calculations, but underprediction is still clear. This evident for all tip speed ratios.

There is generally a better accordance when looking at the tangential forces. Especially close to the design point there are only small differences between the two methods. The differences observed are related to tip and root effects. This confirms the assumption that the BEM method works well close to the design point.

When moving away from the design tip speed ratio, the differences increase. This is expected, as three dimensional effects are presumed to be more dominant for high an low tip speed ratios.

The tip loss effects are related to the presence of a tip vortex. However, looking at the spanwise distribution of tangential forces, there are indications of a trailing vortex at the root as well. This is clearly visible when examining the tangential forces for $\lambda = 6$. In figure 7.7 a clear reduction is seen in dF_z as one approaches the root of the blade. This is an indication that there is leakage of circulation here as well. As this effect is not described in the BEM model, this will lead to certain errors for low radii. However, as these forces acts close to the root of the blade, they contribute little to the total moment. As a result, these errors do not influence the C_P predictions much.

It is evident when looking at figure 7.7 that even though BEM method managed to predict the C_P–curve fairly well for low tip speed ratios, the actual flow physics around the blade are not captured. The spanwise variations in dF_x and dF_z seen in the CFD calculations for $\lambda = 3$ are not at all described by the BEM method. These spanwise variations indicate that there are substantial spanwise pressure gradients and velocity components present in the flow field.

It is clear that there are separating effects present at this point. Both the experimental measurements and the CFD simulations confirm that. The BEM method predicted angles of attack larger than 15° for all radii at $\lambda = 3$. This means that according to the BEM method, the blade should be fully stalled from root to tip at this point. However, looking at the high contribution to the moment (dF_z) occurring at $r/R = 0.3$, the blade do not seem to be stalled at this radial position. dF_z is actually higher inn this case than for any of the other examined tip speed ratios. This could be an indication that rotational augmentation and stall delay effects are present.

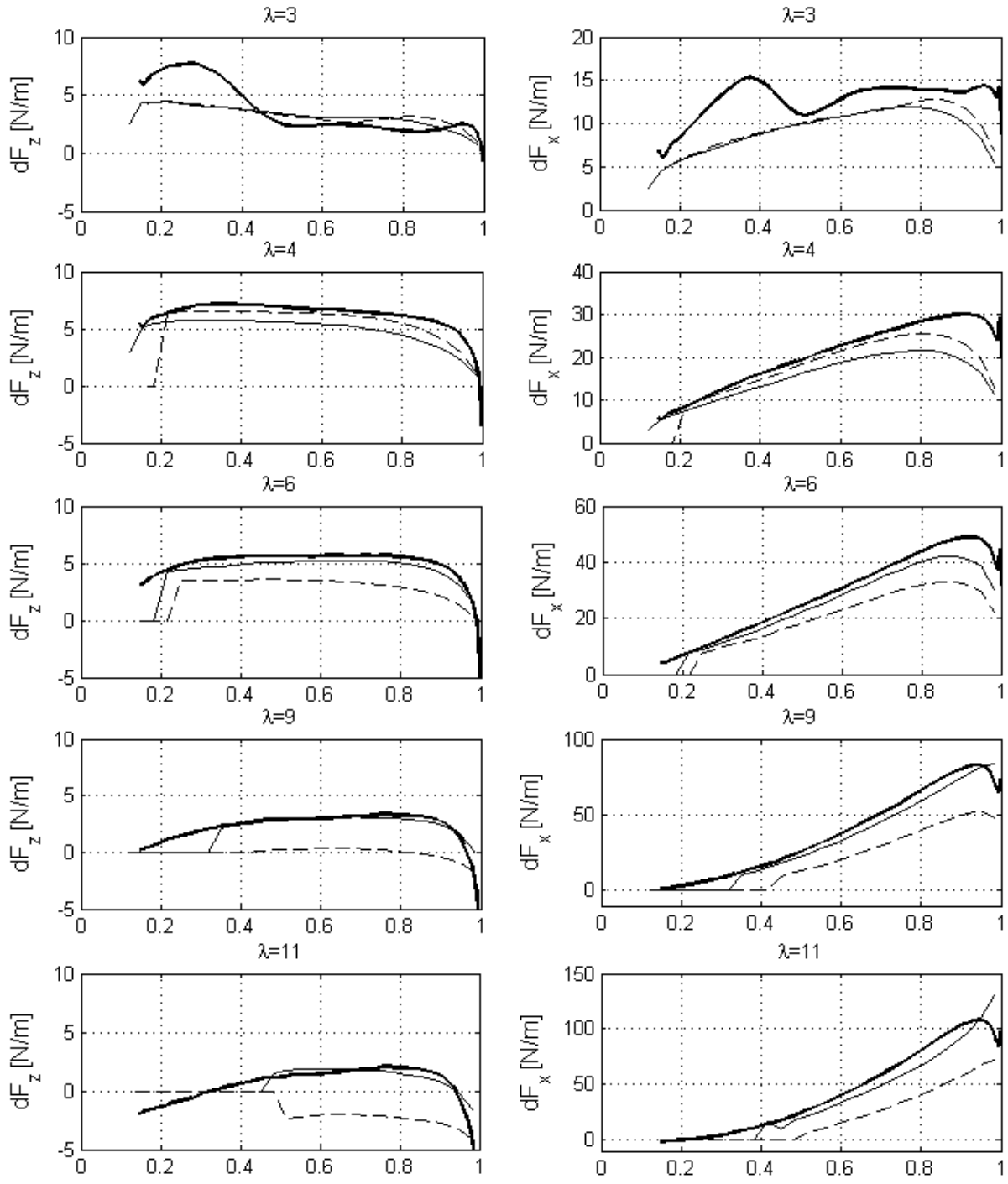

Figure 7.7: Spanwise forces acting on the wind turbine blade for different λ. The forces has been plotted against spanwise (radial) position, r/R. The thick line is the CFD results, while the thinner line is BEM results using $Ncrit = 3.0$ and lift and drag curves for Reynolds numbers corresponding to the operating condition. The dotted line is BEM results using $Ncrit = 9.0$.

7.4 Sectional airfoil characteristics

7.4.1 Methods

A determination of the local angle of attack from the CFD simulations was done using the method proposed and used by Johansen and Sørensen [13]. By determining the mean axial and angular velocity in the rotor plane, the axial and angular induction factors can be determined. Using equation 3.15, the local flow angle (φ) can be determined. Following their method, mean circumferential values of the angular and axial velocities close to the rotor plane value were extracted. This was done using the *'plot circum-avg-radial'* option in FLUENT that should give a representative mean of the specified values. This method gives a mean value of a certain parameter at a given radial distance from the centerline.

In the rotor plane, the values tended to diverge from the trend. This is caused by the discontinuity introduced by the no–slip condition at the blade surface. A value for the rotor plane was found by linear interpolation of the mean flow values 1 cm upstream and downstream of the rotor plane.

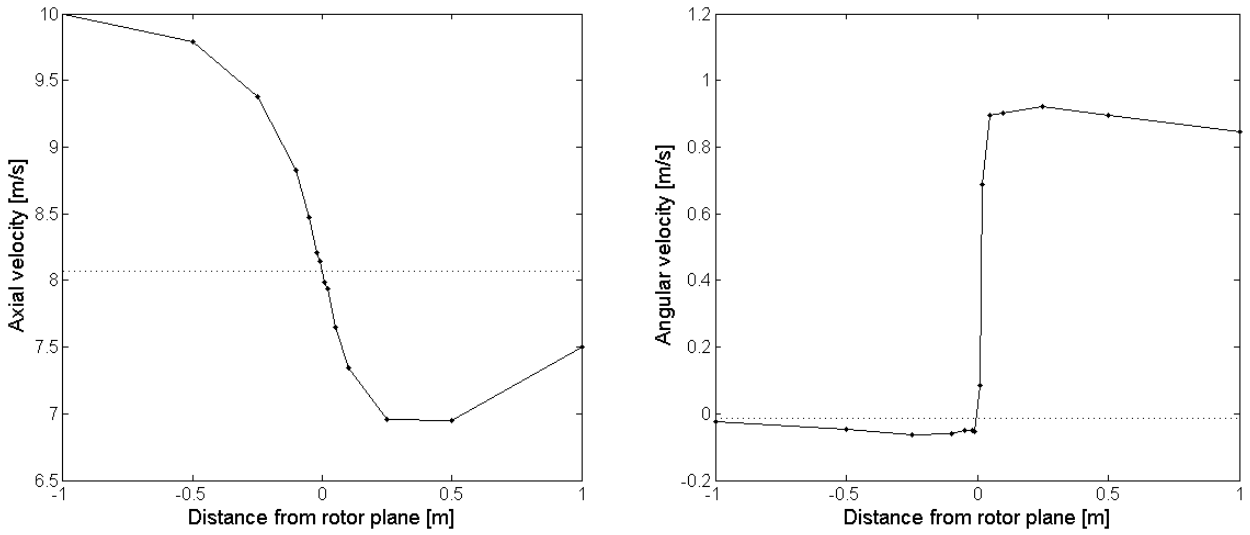

Figure 7.8: The axial and angular velocity close to the rotor plane for $\lambda = 5$, at a radial distance of 70% of the chord.

Because the angular velocities in the rotor plane were generally very low, the angular induction factor was not included in the calculations. Johansen and Sørensen followed the same procedure in their article, and stated that omission of the angular induction factor when estimating the local angle of attack had little influence on the results.

As the local flow angle was found, the local angle of attack for different radii was then determined using the known trigonometrical relation:

$$\alpha = \varphi - \theta$$

The forces acting on the blade are already known. They were non–dimensionalised using a method proposed in the literature [21]:

$$C_n = \frac{dF_x}{\frac{1}{2}\rho C(U_\infty^2 + (\omega r)^2)}$$

$$C_t = \frac{dF_z}{\frac{1}{2}\rho C(U_\infty^2 + (\omega r)^2)}$$

When the axial and tangential force coefficients were transformed into local lift and drag coefficients, using the following equations:

$$C_l = C_n \cos\varphi - C_t \sin\varphi \tag{7.5}$$

$$C_d = C_n \sin\varphi + C_t \cos\varphi \tag{7.6}$$

7.4.2 Sectional lift and drag

Figure 7.9 shows the sectional lift and drag coefficients for the wind turbine, plotted against the angle of attack. The figure also includes a lift and drag curve from XFOIL at a Reynolds number of $1.0 \cdot 10^5$ and a transition criteria of $Ncrit = 3.0$ for comparison. It is clear that there is a good correspondence between the XFOIL results and the CFD results.

The innermost and outermost sections are found to have a smaller lift slope than what is expected in the two dimensional case. This is an indication that both tip and root vortices are present. The induced downwash from the vortex will reduce the effective angle of attack, resulting in a lower slope on the C_l curve [4]. It is also clear that rotational augmentation or stall delay is present. The lift coefficient at $r/R = 0.25$ is increased far beyond what is expected for an airfoil of infinite span, for angles of attack far into the stalled region.

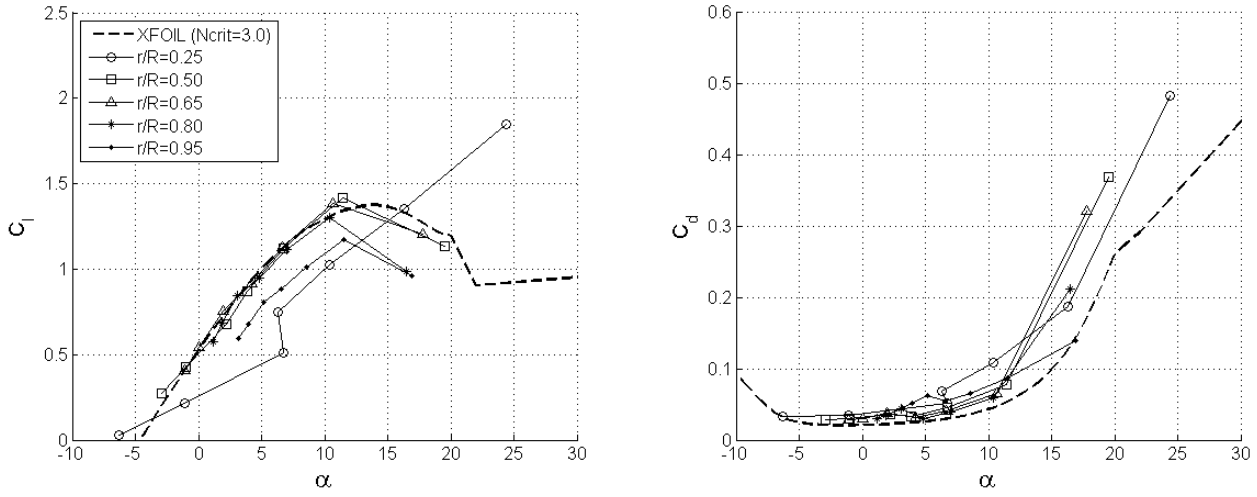

Figure 7.9: Calculation of local lift and drag coefficients for different tip speed ratios.

Moving toward the tip of the blade, it is clear that tip loss effects do affect the performance of the near–tip sections. This is seen as a reduction in maximum lift. The $r/R = 0.80$ section only seems to be influenced by the tip effects at $\lambda = 3$, as it follows the two dimensional results quite well for

all other tip speed ratios. The lift coefficients of the $r/R = 0.5$ and $r/R = 0.65$ sections do follow the two dimensional results remarkably well. This indicates that the reason for failure in the BEM model is related to tip and root effects – effects that the Prandtl tip loss factor seems incapable of describing correctly.

Looking at the drag curve, the correspondence is still good. However, there are indications that stall is precipitated (or hastened) at low tip speed ratios. At high angles of attack, the drag coefficient seems to be increased far beyond what is expected in a two dimensional case. As it is only the innermost section that experiences a stall delay, this might actually be a poor phrase for the observed effect. Rotational augmentation might be a better choice, as the lifting force is augmented, while stall seems to be precipitated for several radii.

7.5 Three dimensional effects

There are several indications that three dimensional effects are present. It is expected that these effects are related to separation on the wind turbine blades. In order to investigate where and when the flow around the wind turbine blades is separating, a study of cross sectional pressure distributions was made. The pressure was obtained using the method described in chapter 7.3.2.

The pressure was non–dimensionalised using the method proposed by Sørensen el. al [21]:

$$-C_p = \frac{p_\infty - p}{\frac{1}{2}\rho C\left(U_\infty^2 + (\omega r)^2\right)} \tag{7.7}$$

The pressure distribution was studied with the boundary layer theory in mind. Generally, a chordwise pressure gradient on an airfoil is an indication that the boundary layer is attached. Alternatively, pressure distribution with no gradient in the chordwise direction indicates boundary layer separation. In this way the separation point can be determined by looking at the C_p–curve. If there is a gradient upstream of the separated area, it is a sign of boundary layer separation. A gradient downstream of the separated area is an indication of boundary layer attachment.

As indicated in the study of spanwise forces, there are indications of massive separation on the blade for the $\lambda = 3$ case. This is evident when looking at figure 7.13, where there are clear indications of separation from the middle of the blade and outwards. At $r/R = 0.50$ the blade seems to be fully stalled, with separation from the leading to the trailing edge of the blade. Closer to the tip, the flow seems to remain attached close to the leading edge.

For $r/R = 0.25$ it is hard to interpret the C_p curve. There are indications of separation on the suction side, close to the leading edge. However, the pressure distribution indicates a shear layer reattachment. A closer look at the velocity field at $r/R = 0.25$ revealed large spanwise velocity components. The flow actually separates at the leading edge, but there is a rapid spanwise flow below the separated flow. Because of the high velocity of this flow, the pressure coefficient remains low over the blade, indicating that separation has not occurred. These radial velocity components remain quite large for all spanwise sections, as seen in figure 7.10.

Looking at figure 7.12, it is seen that the spanwise flow occurring at $\lambda = 3$ starts at the root of the blade and extends all the way towards the tip. These spanwise velocity components are visible for all tip speed ratios. However, they seem to become more dominant as the blade enters the stalled area. When the angle of attack is reduced, suction side pressure is reduced. This can be seen from figure 7.13. This low pressure area seems to draw air from the root of the blade, pulling it in the spanwise direction.

As the angle of attack is increased, the spanwise flow will grow, eventually 'forcing' a separation at the leading edge. But, as the spanwise flow has a rather high velocity, a high lift coefficient can be maintained for low radial sections.

It is important to notice that earlier studies of this rotational augmentation effect have shown that the effect is dependent of rotation. This indicate that centripetal and/or Coriolis forces are important in the description of the physics behind it. However, it seems like it is the pressure potential that gets the spanwise flow started.

As the tip speed ratio is increased to $\lambda = 4$, the massive leading edge separation disappears. Here the pressure distributions seem quite normal for all spanwise sections. This is in accordance with

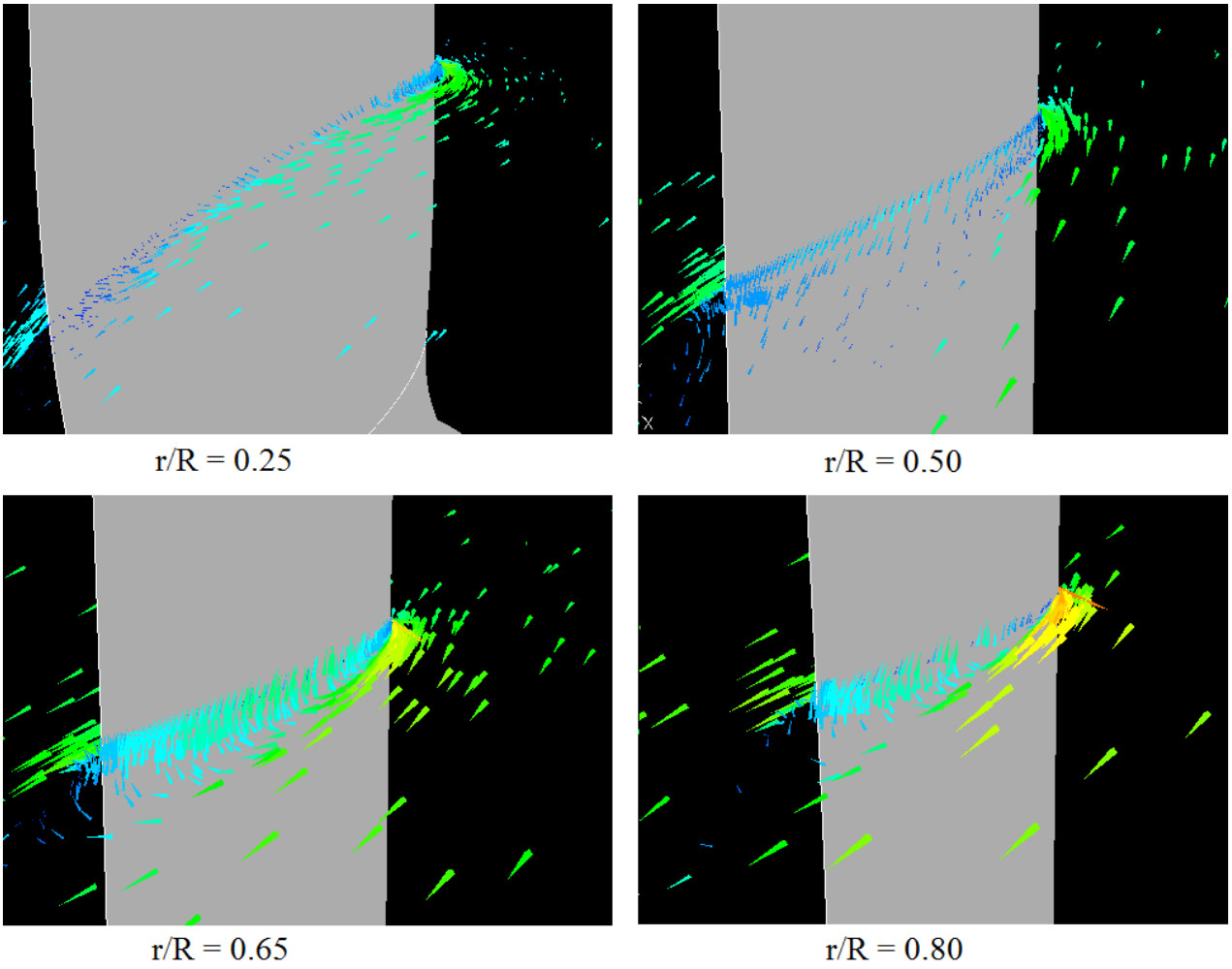

Figure 7.10: Vector plot of the fluid velocity relative to the blade at different spanwise sections for $\lambda = 3$. The separation is found to occur at the leading edge for all spanwise sections, with a spanwise flow below the separated air.

the BEM predictions, that gave angles of attack below 12° for all spanwise sections (see figure 7.1). However, looking at the CFD results, the predicted angle of attack is close to 15° at $r/R = 0.25$, which means that the blade should be stalled at this point.

Looking closer at figure 7.12, it is clear that there are still quite large spanwise velocity components close to the root of the blade. The effect observed for $\lambda = 3$ is observed for $\lambda = 4$ as well. There are signs of leading edge separation close to the root of the blade, but the spanwise velocity components maintains a low pressure on the suction side. Therefore the separation is not visible in the C_p curves.

For $\lambda = 6$ the leading edge separation has disappeared, but the three dimensional effects close to the root are still significant. There are indications of a small recirculation area where the blade meets the junction, seen as an increase in spanwise viscous shear (figure 7.11). However, the local angle of attack near the root of the blade is far below the stall angle for this case.

The fact that separation occurs for low angles of attack indicates that the spanwise components observed for low tip speed ratios do not only depend on the local angle of attack, but also on the blade junction geometry. If the spanwise velocity components depend on the shape of the root of the blade, it would probably be favorable to reduce the size of the gap between the blade and the hub.

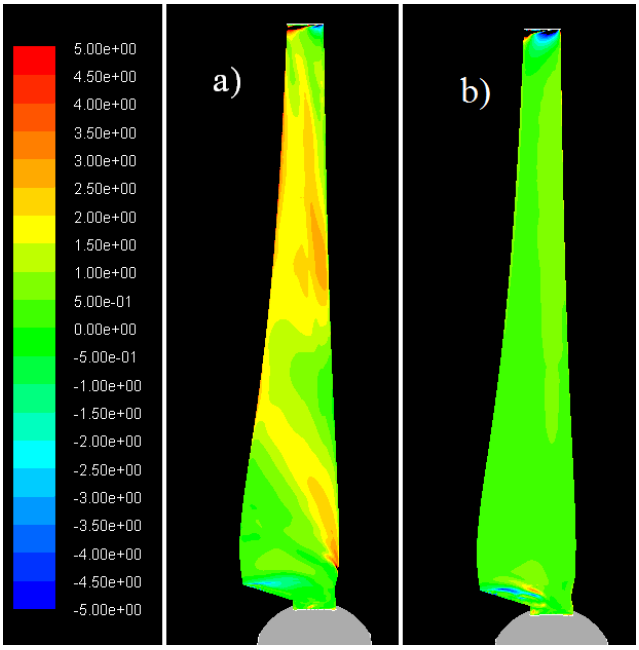

Figure 7.11: Spanwise viscous shear on the suction side of the blade for a) $\lambda = 3$ and b) $\lambda = 6$.

This could reduce both the blade root vortex and the spanwise velocity components. The spanwise velocity components might have a positive effect on the sectional lift coefficients, but they could also lead to strong dynamic effects.

The reduction of the angle of attack is first seen by a reduction of the suction peak near the leading edge. The resulting pressure distributions for moderate tip speed ratios have no signs of deviation from the expected results.

As the tip speed ratio increases towards 9 and 11, the three dimensional effects tend to disappear. The angle of attack is reduced and the pressure difference between the suction and pressure side decreases. When the pressure difference is reduced, the potential causing the spanwise flow disappears. The reduction in pressure difference can be seen from the pressure distributions. For $\lambda = 9$ and 11, the flow close to the root section is almost two–dimensional. Even the root vortex seen for the lower tip speed ratios tend to disappear, as the lift coefficient approaches zero for the root section.

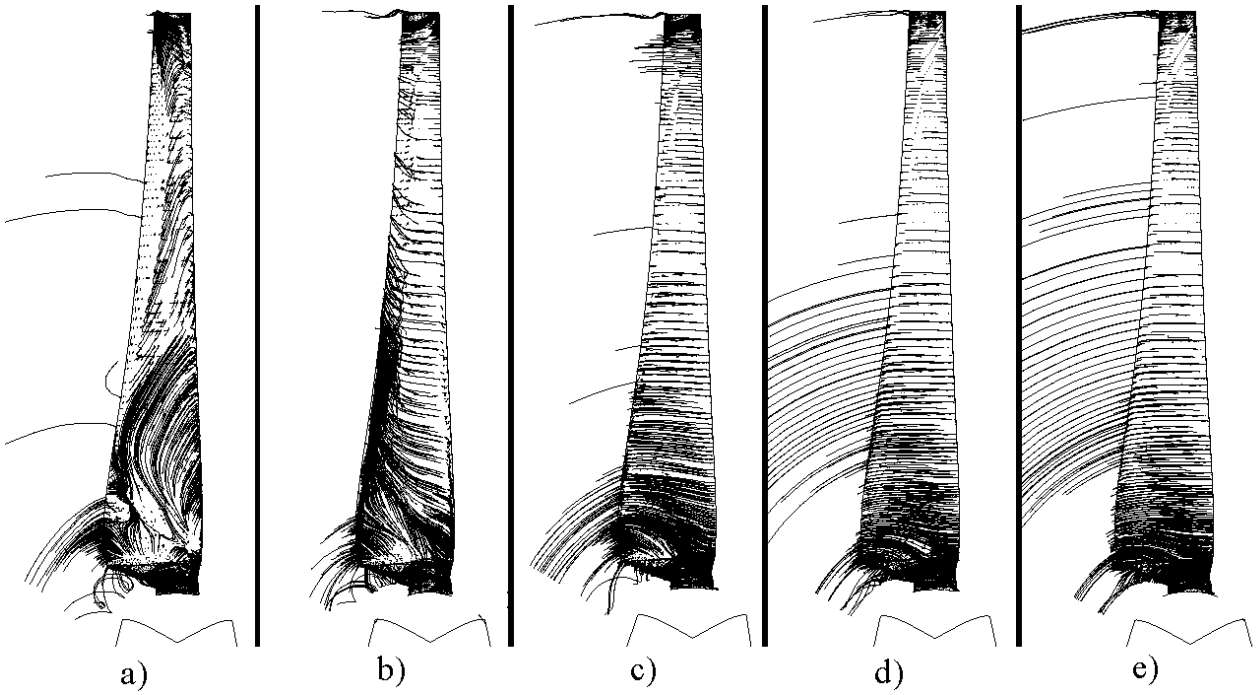

Figure 7.12: Particle tracks and spanwise viscous shear stress on the blade suction side for a) $\lambda = 3$, b) $\lambda = 4$, c) $\lambda = 6$, d) $\lambda = 9$ and e) $\lambda = 11$.

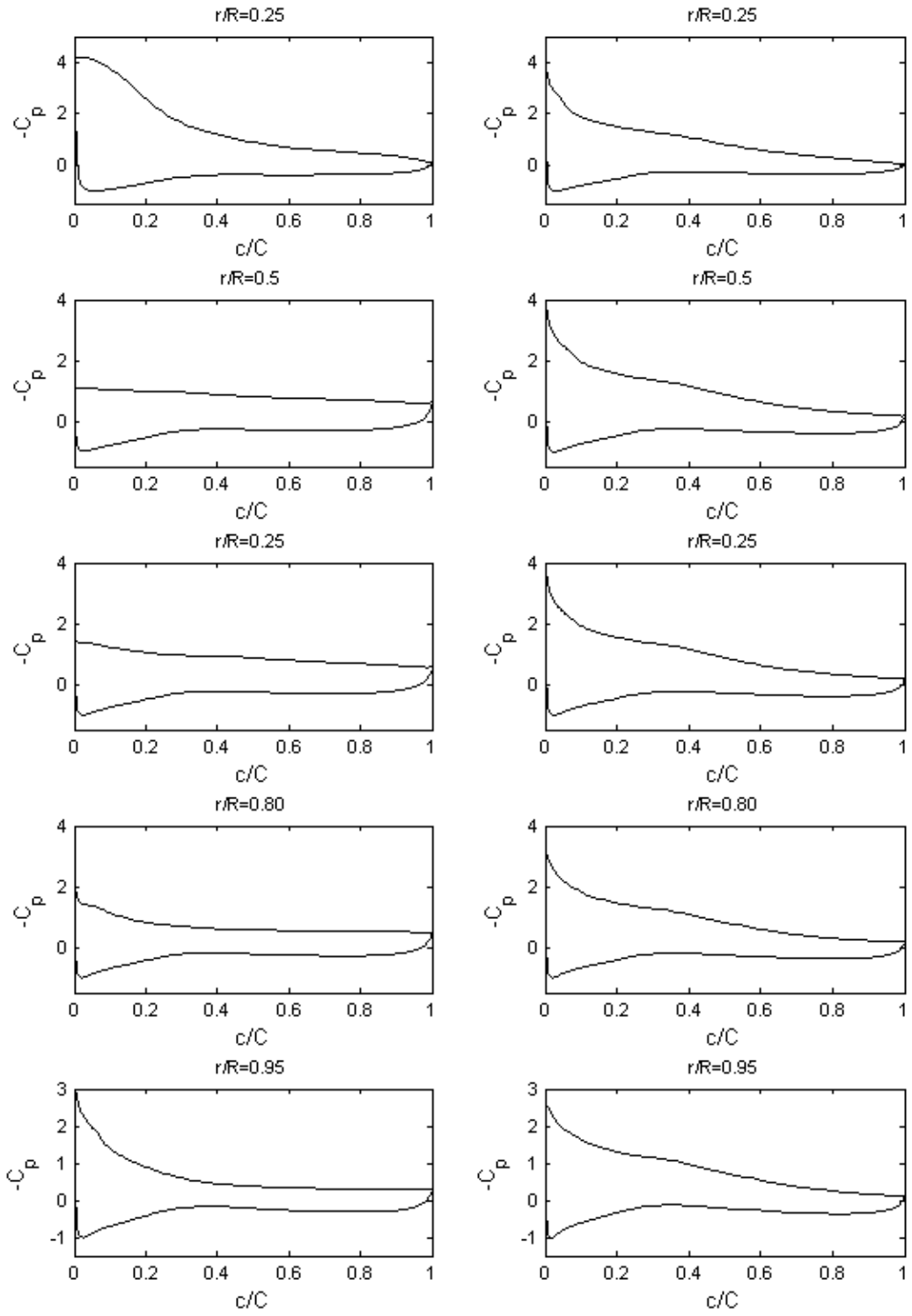

Figure 7.13: Pressure distributions for the $\lambda = 3$ (left) and $\lambda = 4$ (right) case at five spanwise positions.

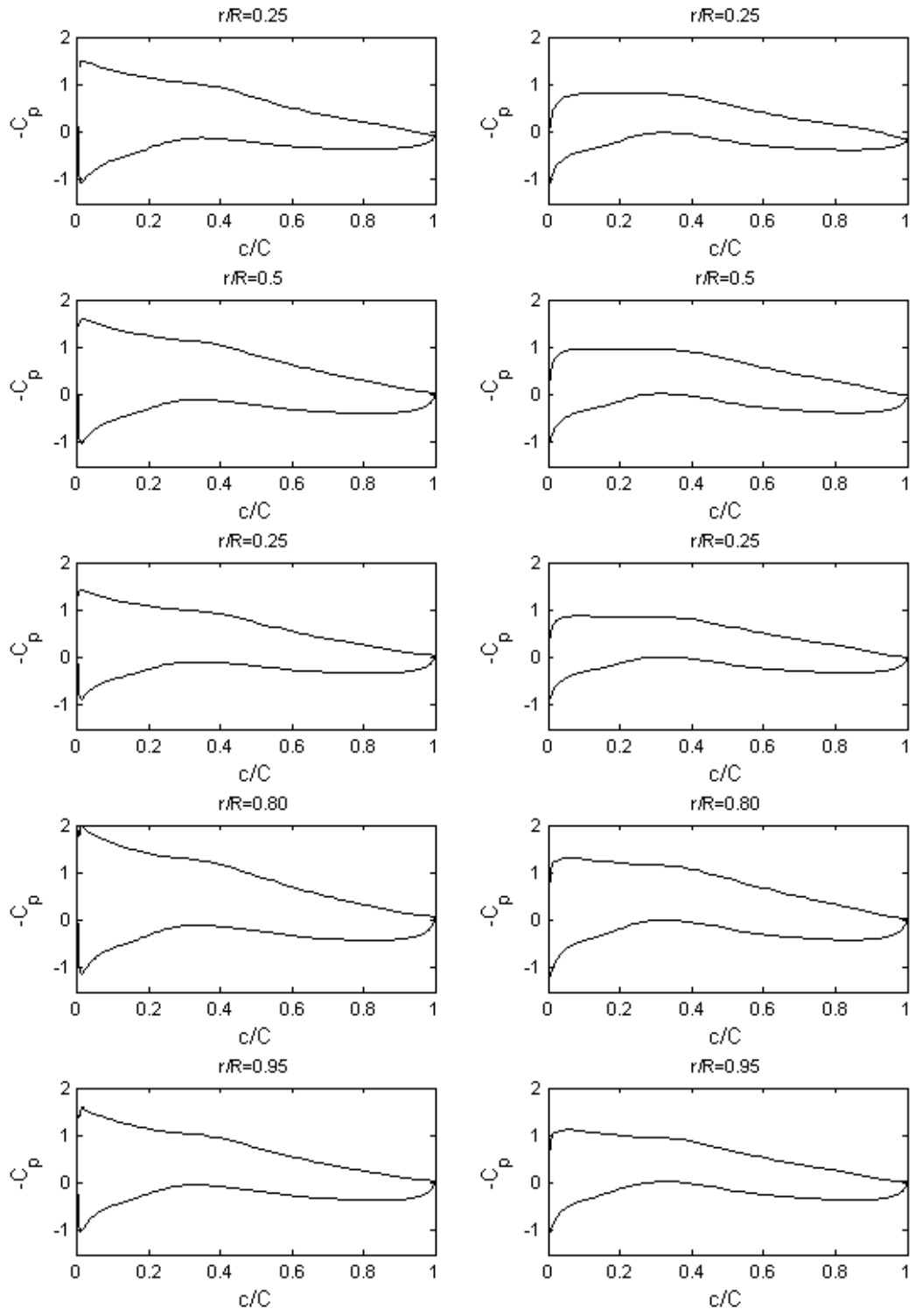

Figure 7.14: Pressure distributions for the $\lambda = 5$ (left) and $\lambda = 6$ (right) case at five spanwise positions.

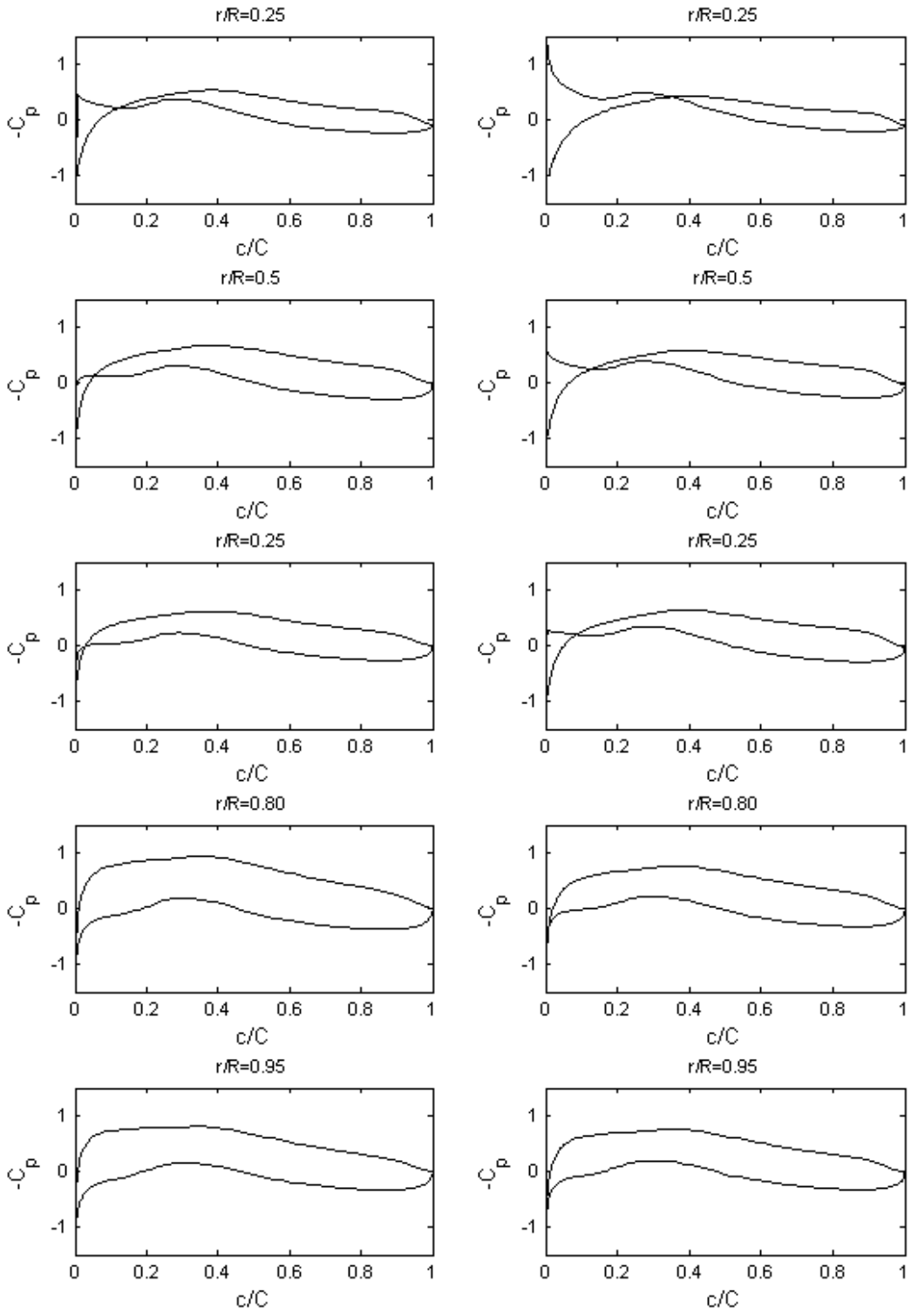

Figure 7.15: Pressure distributions for the $\lambda = 9$ (left) and $\lambda = 11$ (right) case at five spanwise positions.

Chapter 8

Conclusions

8.1 Concluding remarks

An experiment conducted in the wind tunnel at NTNU confirmed that the model wind turbine was working according to estimates made using a BEM method. However, as the profile used throughout the blade has been designed for a Reynolds number twenty times higher than what is expected in the wind tunnel, the airfoil is exposed to laminar separation. This has been observed in laboratory work performed by Muyiwa Adaramola [1].

At tip speed ratios below design conditions, severe dynamic effects were observed, probably related to stalling of the blade. The BEM method was able to predict the onset of stall, but as a one–dimensional method, the dynamics behind it was not captured.

Initial two–dimensional CFD simulations of the flow around the NREL s826 airfoil were performed in order to determine reasonable grid parameters for the three–dimensional grid. It was revealed that a structured boundary layer grid with at least 15 cells, and a height of $0.1C$ was sufficient to capture the boundary layer flow. When using an unstructured grid in the rest of the domain, the external grid growth rate should be kept as low as possible. The use of enhanced wall treatment and the k–ω SST–model gave good predictions of the airfoil forces.

Based on the experience from the initial simulations, a three–dimensional grid was created, and full 3D CFD simulations of the wind turbine were conducted. Rotational periodicity was assumed in order to reduce the size of the grid.

In general, good accordance was observed between the CFD simulations and experimental data. For low tip speed ratios the power curve predictions were well within the measured standard deviations, with errors less than 5%. For higher tip speed ratios the errors were somewhat higher. This is expected to be caused by low grid refinement close to the root of the blade. The thrust was somewhat underpredicted, which was expected due to the exclusion of wind turbine tower and transmission belt in the CFD model.

Prandtls tip loss factor has been included in the BEM calculations. It is clear that the correction factor manages to describe the tip loss effects fairly well for moderate tip speed ratios. Close to the design point, the accordance between the BEM and CFD results for tangential forces on the blade are almost perfectly matched. However, for high tip speed ratios, the BEM method overpredicts the thrust forces near the tip of the blade.

The BEM calculations tended to give lower estimates of the thrust force than the CFD model for all operational conditions. But it is clear that the introduction of Glauerts correction factor for high values of a improves the results. The power curve is fairly well described for all tip speed ratios, but the errors tend to be smaller near the design tip speed ratio. Under these operational conditions three–dimensional effects are small, and the angle of attack is rather constant over the blade.

A further examination of the forces acting on the blade revealed that there were substantial three–dimensional effects present for low tip speed ratios. These effects caused large spanwise variations in the force distribution on the blade, combined with evidence of rotational augmentation. The rotational augmentation was visible as sectional lift coefficients near the root of the blade were increased far beyond what could be expected for two dimensional flow. However, the rotational augmentation was found to occur in cases where there was leading edge separation on the blade. The increased lift was caused by a rapid spanwise flow beneath the separated air. Due to these observations, the term 'stall delay' that is used in the literature is regarded to be a poor phrase, not describing the actual physics behind the effect.

There are indications that the three dimensional effects observed near the root of the blade are dependent on the root geometry. Near the root of the blade separation seems to be precipitated due to a certain leakage of flow around the root edge of the blade. Separation at the root was observed for a tip speed ratio of 6, where the angle of attack is low and three dimensional effects are expected to be small. This indicates that an improvement of the root geometry could reduce the spanwise flow on the blade for low tip speed ratios.

8.2 Further work

The BEM method proved to have certain convergence problems in cases where the axial induction factor became negative. In these cases the turbine works as a propeller, adding energy to the flow. This occurs close to the root of the blade for high tip speed ratios, and the code needs to be improved in order to capture these effects.

The Prandtl tip loss factor proved to be unable to predict the spanwise thrust force distribution for high tip speed ratios. There is a new class of tip loss factor emerging, and several of these are presented in the literature [20]. It is probable that an improvement of the tip (and hub) loss predictions can improve the BEM predictions.

Future testing of the wind turbine should be conducted at a fixed rotational speed, in order to reduce the change of blade Reynolds number between the different operational conditions. It is important to keep this speed so high that laminar effects do not become dominant.

The experimental results revealed strong dynamic effects as the blade entered the stalled area. These effects have been discussed in this report, and there are indications that they could be caused by laminar separation. This could be examined by relatively simple experiments in the wind tunnel. Further studies should be undertaken in order to determine the effects of rotation on transition, and furthermore if the regular $Ncrit$ transition criteria is applicable for a rotating wind turbine.

The actual physics behind the rotational augmentation found in this study is still incompletely understood and characterised. This calls for further studies on the behavior of rotating wind turbine blades in stalled condition.

Bibliography

[1] Muyiwa Adaramola, 2009. Laboratory work in progress.

[2] AIAA. Guide for the verification and validation of computational fluid dynamics simulations, 1998. AIAA G-077-1998.

[3] W A Basha and W S Ghaly. Drag Prediction in Transitional Flow over Airfoils. *Journal of Aircraft*, 44:824 – 832, 2007.

[4] J J Bertin. *Aerodynamics for Engineers, 4th ed.* Prentice Hall, 1994.

[5] P A Davidson. *Turbulence, an introduction for scientists and engineers.* Oxford University Press, 2004.

[6] M Drela and H Youngren. XFOIL 6.9 User Primer, 2001.

[7] C Kjaer et. al. Wind Energy - The Facts, 2009.

[8] Fluent. www.fluent.com, 2008. 03.03.2009.

[9] Per Åge Krogstad, 2009. Private communication.

[10] M O L Hansen. *Aerodynamics of Wind Turbines, 2nd ed.* Earthscan, 2008.

[11] H Hu and Z Yang. An Experimental Study og the Laminar Flow Separation on a Low-Reynolds-Number Airfoil. *Journal of Fluids Engineering*, 130, 2008.

[12] J Johansen, H Aa Madsen, M Gaunaa, C Bak, and N N Sørensen. Design of a Wind Turbine Rotor for Maximm Aerodynamic Efficiency. *Wind Energy*, 2008.

[13] J Johansen and N N Sørensen. Aerofoil Characteristics from 3d CFD Rotor Computations. *Wind Energy*, 7:283 – 294, 2004.

[14] V P Jones and B E Launder. The prediction of Laminarization with a Two-Equation Model of Turbulence. *International Journal of Heat and Mass Transfer*, 15:301 – 314, 1972.

[15] P B S Lissaman. Low Reynolds Number Airfoil. *Ann. Rev. Fluid Mechanics*, 15:223 – 239, 1983.

[16] F R Menter. Two-Equation Eddy-Viscosity Turbulence Models for Engineering Applications. *AIAA*, 32:1598 – 1605, 1994.

[17] C L Rumsey. Apparent Transition Behaviour of widely-used Turbulence Models. *International Journal of Heat and Fluid Flow*, 28:1460 – 1471, 2007.

[18] H Schlichting and K Gersten. *Boundary Layer Teory, 8th ed.* Springer, 1999.

[19] S J Schreck, N N Sørensen, and M C Robinson. Aerodynamic Structures and Processes in Rotationally Augmented Flow Fields. *Wind Energy*, 10:159 – 178, 2007.

[20] W Z Shen, R Mikkelsen, J N Sørensen, and C Bak. Tip Loss Corrections for Wind Turbine Computations. *Wind Energy*, 8:457 – 475, 2005.

[21] N N Sørensen, J A Michelsen, and S Schreck. Navier Stokes predictions of the NREL Phase VI rotor in the NASA Ames 80-by-120 Wind Tunnel. AIAA Paper 2002-0031, 2002.

[22] E Sæta. The Blade Element Momentum Method. Project–thesis, 2008.

[23] Nobou Tanaka. *World Energy Outlook 2008.* IEA, 2008.

[24] H. Tennekes and J. L. Lumley. *A First Course in Turbulence, 3rd ed.* MIT Press, 1972.

[25] L W Traub and E Cooper. Experimental Investigation of Pressure Measurements and Airfoil Characteristics at Low Reynolds Numbers. *Journal of Aircraft*, 45:1322 – 1333, 2008.

[26] H K Versteeg and W Malalasekera. *Computational Fluid Dynamics, The finite volume method.* Pearson, 2007.

[27] Frank M. White. *Viscous Fluid Flow, 3rd ed.* McGraw–Hill, Inc, 1991.

[28] David C. Wilcox. *Turbulence Modeling for CFD.* DCV Industries, Inc, 1994.

[29] J Windte, U Scholz, and R Radespiel. Validierung der RANS-Simulation Laminarer Ablöseblasen auf Profilen. *Aerospace and technology*, 10:484 – 494, 2006.

[30] Victor Yakhot and Steven A Orszag. Renormalization Group Analysis of Turbulence. I. Basic theory. *Journal of Scientific Computing*, 1:3 – 51, 1986.

[31] Victor Yakhot and Leslie M Smith. The Renormalization Group, ε-expansion and the Derivation of Turbulence Models. *Journal of Scientific Computing*, 7:35 – 61, 1992.

Appendix A

Appendix

A.1 Calibration curves

A.1.1 Thrust gauge

The calibration curve for the thrust force given i kg was given by:

$$T = 3.5763 \frac{V_{t,measured} - V_{t,offset}}{V_{t,gain}} - 0.0118 \tag{A.1}$$

The offset voltage was -8.110 V, and the amplifier gain was set to 8. The calibration was done using weights directly attached to the gauge. The weight box had a mass of 449 g, and masses up to 6 kg was attached.

Weight [kg]	**Volts**	$V - V_{t,offset}$
0	-8.110	0
0.449	-7.054	0.132
0.949	-5.984	0.26575
1.449	-4.862	0.406
1.949	-3.732	0.54725
2.449	-2.609	0.687625
2.949	-1.366	0.843
3.449	-0.379	0.966375
3.949	0.740	1.10625
4.449	1.853	1.245375
4.949	2.973	1.385375
5.449	4.089	1.524875
5.949	5.238	1.6685
6.449	6.33	1.805

Table A.1: Calibration data for thrust gauge.

A.1.2 Torque gauge

The calibration curve for the torque given in Nm was given by:

$$M = -0.2042 \frac{V_{m,measured} - V_{m,offset}}{V_{m,gain}} + 0.007 \tag{A.2}$$

The offset voltage was 8.044 V, and the amplifier gain was set to 1. The moments was measured attaching weights at a radial distance of 0.448 m from the hub. The weight box had a mass of 16 g, and masses up to 400 g was used to generate moments.

Weight [kg]	**Force** [N]	**Torque** [Nm]	**Volts**	$V - V_{m,offset}$
0	0	0	8.044	0
0.016	0.156896	0.070289408	7.634	-0.41
0.066	0.647196	0.289943808	6.672	-1.372
0.116	1.137496	0.509598208	5.647	-2.397
0.166	1.627796	0.729252608	4.567	-3.477
0.216	2.118096	0.948907008	3.445	-4.599
0.266	2.608396	1.168561408	2.404	-5.64
0.316	3.098696	1.388215808	1.17	-6.874
0.366	3.588996	1.607870208	0.224	-7.82
0.416	4.079296	1.827524608	-0.878	-8.922

Table A.2: Calibration data for torque gauge. $V_{m,gain} = 1V$

A.1.3 Pressure gauge

The pitot tube was already calibrated, and the calibration curve was given as:

$$p_{dynamic} = -61.89 \frac{V_{p,measured} - V_{p,offset}}{V_{p,gain}} + 0.007 \tag{A.3}$$

The offset voltage was -7.825 V, and the amplifier gain was set to 5.

A.2 Experimental data

The measured data is given below.

ω	T [° C]	**Thrust** [kg]	**Torque** [Nm]	**Dyn. pressure** [Pa]
101	23.0	0.821030863	0.1922094	59.649582
200	23.2	1.004316238	0.2448930	59.377266
299	23.3	1.180001975	0.3008438	59.909520
401	23.4	1.453141888	0.4066194	63.276336
500	23.4	1.733434400	0.5191336	65.417730
599	23.5	1.847428963	0.6198042	58.585074
701	23.5	2.235457513	1.1445982	58.238490
800	23.6	2.818841450	1.6352908	57.953796
899	23.7	3.397307975	1.5848534	57.817638
1001	23.7	3.477327688	1.5603494	57.607212
1100	23.7	3.572993713	1.5035818	57.508188
1199	23.9	3.753149825	1.4129170	57.644346
1301	23.9	3.904695538	1.2967272	57.273006
1400	24.0	4.054900138	1.1954440	57.396786
1499	24.1	4.191246575	1.0859928	57.409164
1601	24.1	4.305688175	0.9581636	57.099714
1700	24.1	4.438905350	0.8485082	57.396786
1799	24.1	4.536806563	0.7233336	57.248250
1901	24.1	4.627555175	0.5965254	57.211116
2000	24.2	4.707127850	0.4772726	57.297762
2099	24.2	4.771054213	0.3572030	57.136848
2201	24.3	4.848838738	0.2426468	57.112092
2300	24.4	4.931093638	0.1368712	57.248250
2399	24.4	5.010666313	0.0276242	57.223494
2450	24.4	5.036594488	-0.028735	57.149226

Table A.3: Measured data

A.3 Blade design

The blade design used in the BEM–calculations was similar to the original design proposed by Sata [22], however, some changes was made close to the root of the blade. This was done to represent the shape of the actual blade better. The junction part of the blade is represented by keeping the twist angle more or less constant, while reducing the chord length.

r	c/R	θ
7.5000000e-003	3.0000000e-002	1.2000000e+002
2.2500000e-002	3.0000000e-002	1.2000000e+002
4.9000000e-002	3.0000000e-002	1.2000000e+002
5.5000000e-002	1.1000000e-001	3.8000000e+001
6.7500000e-002	1.8096180e-001	3.7054990e+001
8.2500000e-002	1.7802475e-001	3.2544100e+001
9.7500000e-002	1.7113681e-001	2.8676740e+001
1.1250000e-001	1.6250122e-001	2.5261900e+001
1.2750000e-001	1.5335073e-001	2.2430330e+001
1.4250000e-001	1.4433777e-001	1.9987820e+001
1.5750000e-001	1.3578290e-001	1.8034450e+001
1.7250000e-001	1.2782281e-001	1.6348850e+001
1.8750000e-001	1.2049533e-001	1.4663250e+001
2.0250000e-001	1.1378725e-001	1.3067150e+001
2.1750000e-001	1.0766085e-001	1.1829070e+001
2.3250000e-001	1.0206832e-001	1.0752650e+001
2.4750000e-001	9.6959534e-002	8.8827240e+000
2.7750000e-001	8.8002408e-002	7.9877430e+000
2.9250000e-001	8.4068035e-002	7.2526930e+000
3.0750000e-001	8.0446168e-002	6.5649770e+000
3.2250000e-001	7.7104257e-002	5.9186800e+000
3.3750000e-001	7.1148557e-002	4.7185370e+000
3.6750000e-001	6.8486964e-002	4.1316170e+000
3.8250000e-001	6.6008976e-002	3.5438940e+000
3.9750000e-001	6.3697134e-002	2.9433360e+000
4.1250000e-001	6.1535992e-002	2.2185090e+000
4.2750000e-001	5.9511861e-002	1.0970280e-001
4.4250000e-001	5.7612581e-002	-7.167448e-001

Table A.4: Blade design input to BEM–calculations.

A.4 Examination of laminar separation bubbles

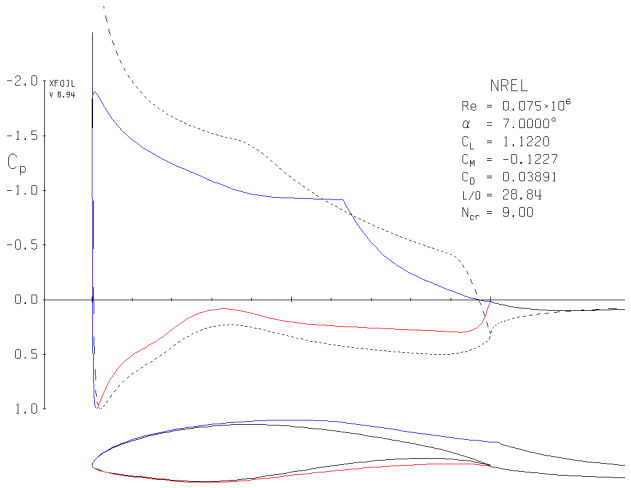

Figure A.1: XFOIL calculation at $\alpha = 7°$ and Re $= 7.5 \cdot 10^4$ with $Ncrit = 9.0$. The laminar separation bubble on the suction side is clearly seen from the C_p curve, reattaching at $c/C \approx 0.65$.

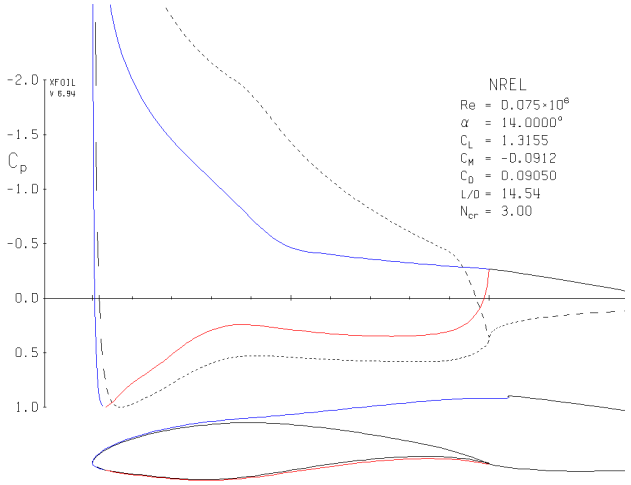

Figure A.2: XFOIL calculation at $\alpha = 14°$ and Re $= 7.5 \cdot 10^4$ with $Ncrit = 3.0$. The transition occur near the suction peak at the leading edge and no laminar separation is visible. The boundary layer separates at $c/C \approx 0.45$

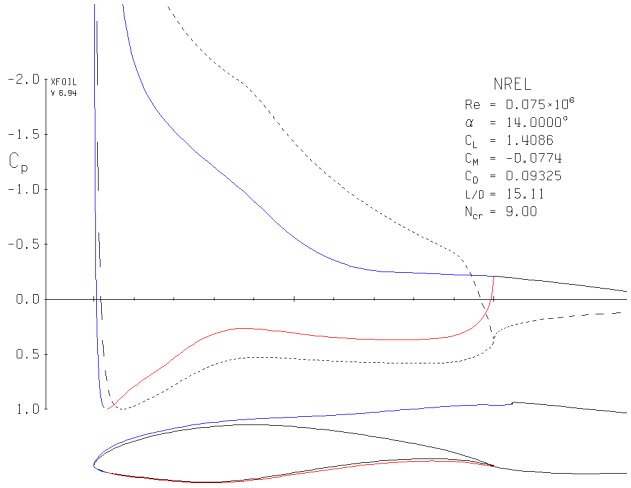

Figure A.3: XFOIL calculation at $\alpha = 14°$ and Re $= 7.5 \cdot 10^4$ with $Ncrit = 9.0$. The laminar separation bubble can be seen near the leading edge, as a small bulge in the displacement thickness line. Compared to figure A.2, the separation is found to be delayed, resulting in less drag and more lift.

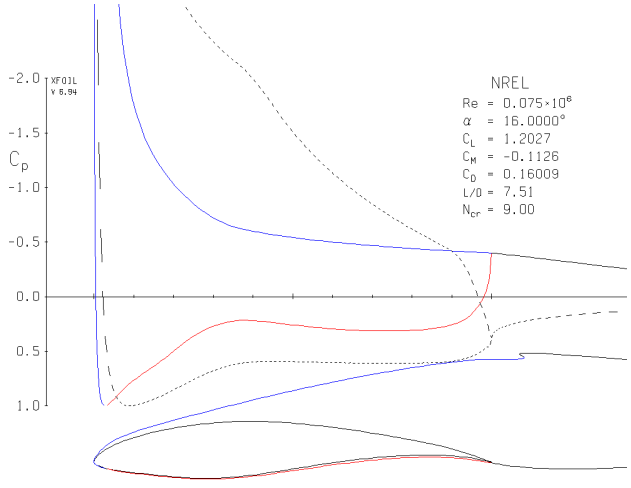

Figure A.4: XFOIL calculation at $\alpha = 16°$ and Re $= 7.5 \cdot 10^4$ with $Ncrit = 9.0$. The laminar separation bubble has bursted, causing full stall from the leading edge. Compared to figure A.3, the drag has been increased dramatically.

A.5 Grid parameters (reduced size)

Grid	**O X**	**O XI**	**O XIV**	**O XIVa**	**O XIVb**	**O XX**
# cells	6557	7764	7436	6342	5760	8725
External growth rate	1.2	1.2	1.2	1.3	1.45	1.2
Nodes in BL	15	20	20	20	20	20
BL growth rate	1.24	1.15	1.21	1.21	1.21	1.24
BL height	0.05c	0.05c	0.1c	0.1c	0.1c	0.15c

Table A.5: Grid parameters for some of the grids used in the second part of the grid sensitivity study.

A.6 Periodic boundary grid

A figure of the periodic boundary grid is attached.

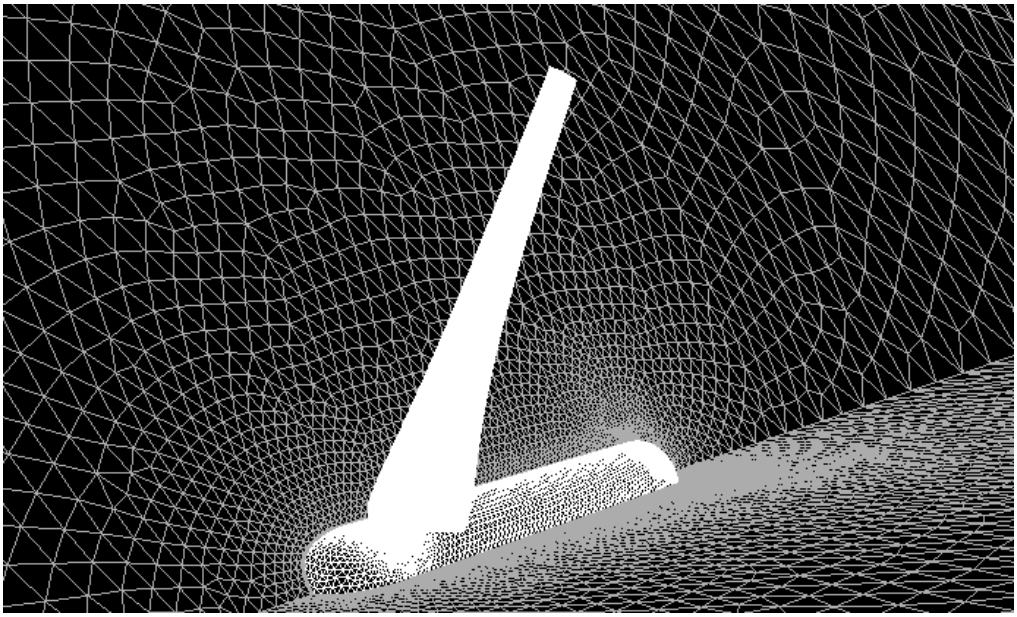

Figure A.5: Periodic boundary surface grid

A.7 Blade y_p^+ values

The y_p^+ values for three different cases have been plotted. It is seen that the grid refinement is sufficient for all cases.

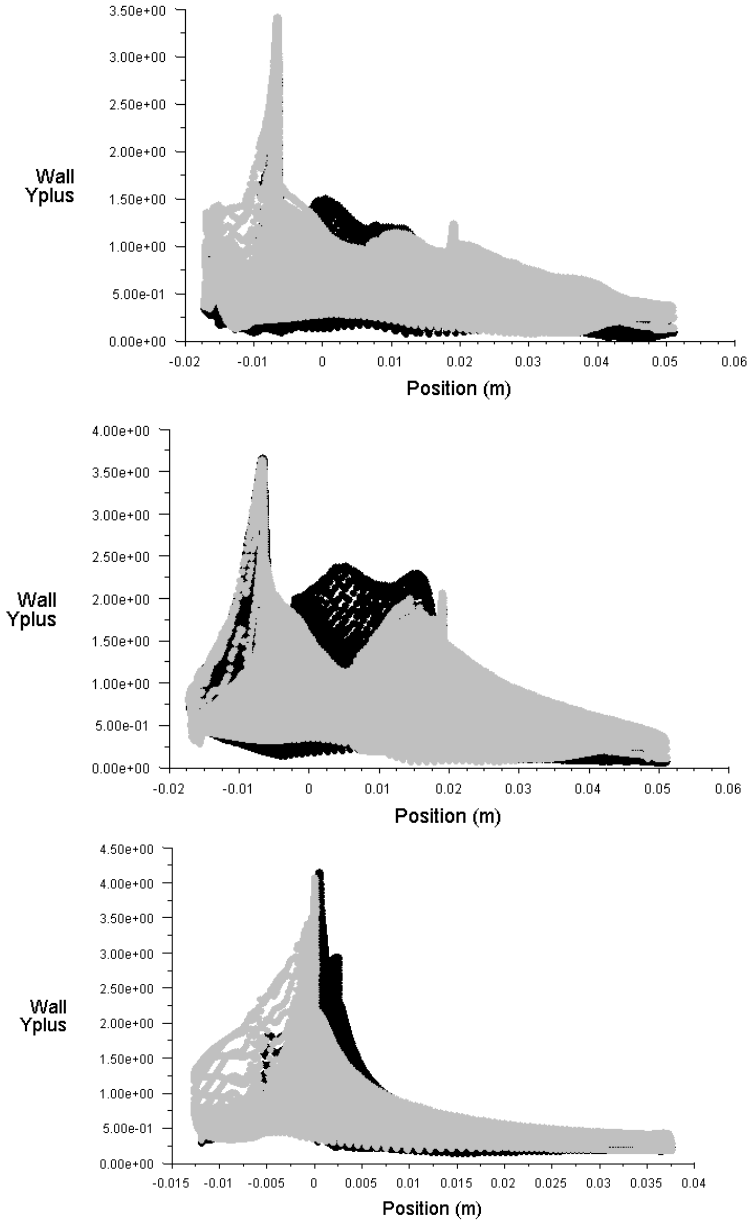

Figure A.6: y_p^+ values on the blade surface for the $\lambda = 3$ above, $\lambda = 6$ in the middle and $\lambda 11$ at the bottom.

A.8 Convergence monitoring

A typical convergence history. The solution was started at 4000 iterations, from the $\lambda = 4$ case. A non–oscillating solution was found after 1000 iterations, using 1. order discretisation. Then the QUICK scheme was applied, reaching maximum convergence after 1000 iterations more. An additional 500 iterations was taken in order to reduce residuals more, and minimize iterative convergence error. Additional iterations was made to reduce the residuals for k, without altering the C_m and C_d results.

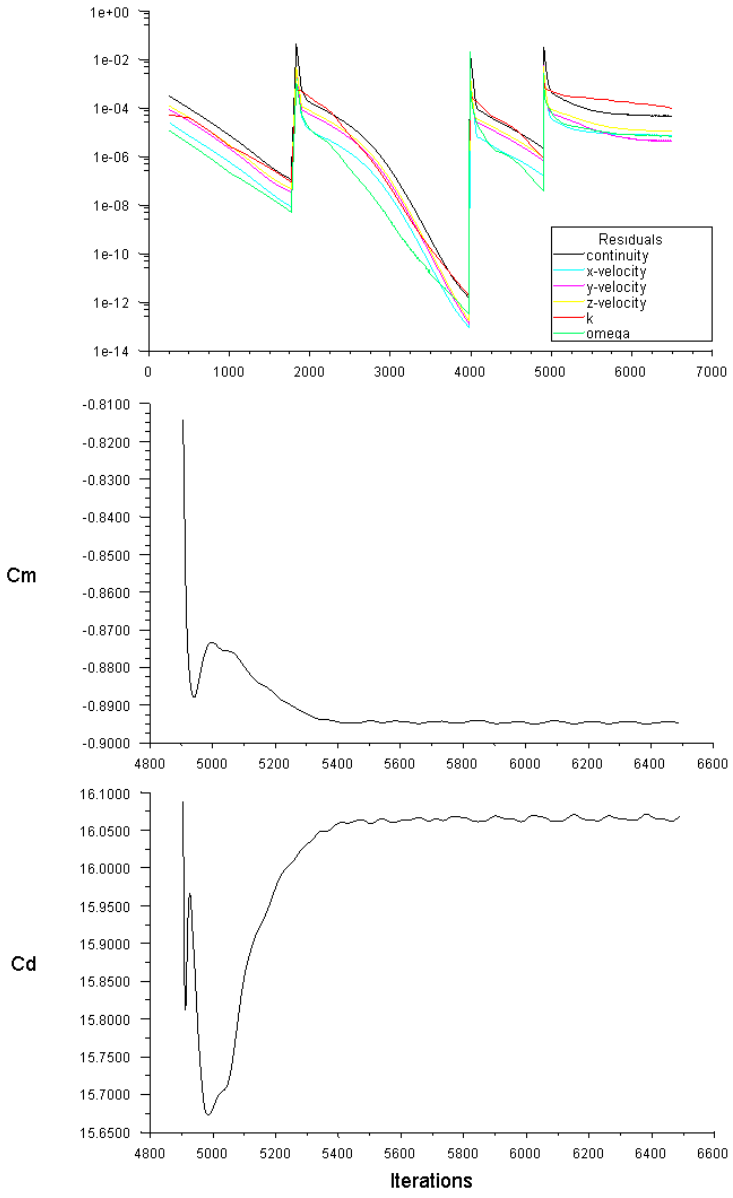

Figure A.7: Convergence history for the $\lambda = 5$ case.

A.9 Critical Reynolds number for a cylinder

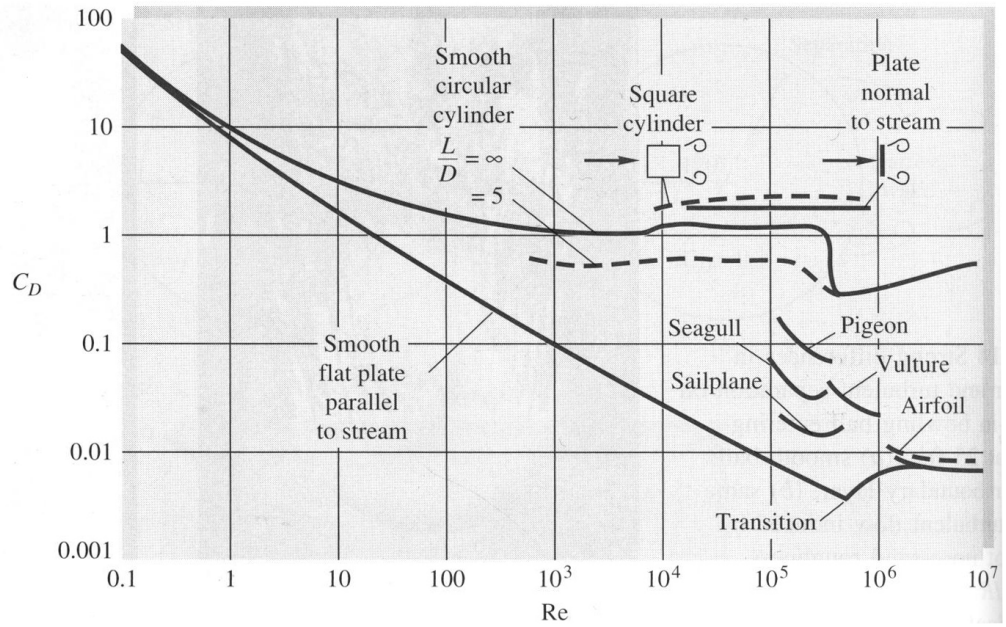

Figure A.8: C_d as a function of Reynolds number for different bodies. From White [27].